

Techniques for phase noise mitigation in photonic THz wireless systems

Luis Gonzalez Guerrero

A dissertation submitted in partial fulfillment
of the requirements for the degree of
Doctor of Philosophy
of
University College London.

Electronic & Electrical Engineering
University College London

August 4, 2019

I, Luis Gonzalez Guerrero, confirm that the work presented in this thesis is my own. Where information has been derived from other sources, I confirm that this has been indicated in the work.

Abstract

Wireless communications at THz frequencies are considered a solution to overcome the spectrum congestion at lower radio frequencies. Photomixing two free-running lasers in an ultra-fast photodiode is an attractive technique for THz generation for its seamless integration with optical networks. However, the THz signal generated with this method can suffer from high phase noise.

In the first part of the thesis, the envelope detection of THz single sideband (SSB)-with carrier signals is proposed as the mean to combat such phase noise. Using an ideal envelope detector (ED) at the THz receiver, no significant phase noise penalty is observed in a system operating at 250 GHz and for combined linewidths of up to 1 MHz. The use of interference cancellation algorithms is then proposed as a mean to increase the bandwidth efficiency of the proposed system. Using the Kramers-Kronig algorithm, an efficiency improvement of 38% is achieved with respect to the the case without this algorithm. Next, the performance of three different techniques for generating THz SSB signals is analyzed through numerical simulations and end-to-end implementation of each of them is experimentally demonstrated. According to the simulation, the technique giving better performance is also the one requiring lower analog bandwidth on the transmitter arbitrary waveform generator. This, however, comes at the expense of an increased analog complexity.

The second part of this thesis focuses on wireless bridges. To mitigate the phase noise associated with the high number of free-running lasers that form this type of link, the pilot tone-assisted technique is proposed. The wireless bridge is demonstrated in several scenarios: single channel transmission, wavelength division multiplexing network and multiple user support. The last part of this chapter

discusses the configuration and DSP to achieve a 40 Gbit/s wireless bridge

Impact statement

THz communications (100 GHz - 10 THz) have emerged as a solution to the scarce spectrum available at low radio frequencies - insufficient to cope with the rapid growth of wireless internet traffic - and a lack of technology to match wireless data rates to those provided by optical fiber communications. In this context, this thesis explores several transmission configurations for photonic THz systems, which generate the THz signal via optical technologies. A strong focus is placed on phase noise mitigation, which can prevent the system to use higher order modulation formats. This however, is key to achieving the high data rates that are envisaged for wireless communications.

In the first part of this thesis we propose the reception of higher-order single-sideband THz signals with an envelope detector. Experimental investigations of the phase noise sensitivity of this scheme are carried out in a system operating at 250 GHz, transmitting 5 GBd 16-QAM signals through 10 km of optical fiber, and for combined optical linewidths of up to 1 MHz. No penalty associated with increasing linewidth is measured, indicating that cost-efficient free-running foundry-fabricated lasers (linewidths of few MHz) are compatible with this technique. This, besides the obvious advantage of cost and footprint reduction, significantly lowers the complexity of the transmitter as no complex locking techniques are required. This is the first investigation to experimentally verify the phase robustness of this technique. To increase the bandwidth efficiency of this scheme we propose the use of digital signal processing for signal-signal beat interference mitigation. An efficiency gain of 38% with respect to the case without interference cancellation algorithms is obtained with the Kramers-Kronig receiver. This efficiency increase can be critical as

optical networks evolve to ultra-dense wavelength multiplexing formats, where the use of guard bands may not be acceptable.

In the second part of this thesis we focus on the development of THz wireless bridges, which have attracted the interest of the research community because of the many scenarios where they could find application, from data centres to backhaul distribution in mobile and optical networks. To tackle the phase noise associated with the high number of free-running lasers associated with this type of links, we propose the use of the tone-assisted phase compensation technique. With this technique we demonstrate a wireless bridge operating at 250 GHz and transmitting 16-quadrature amplitude modulation (QAM) 40 Gbit/s signals. To the best of the authors knowledge this is the only demonstration of a wireless bridge operating above 100 GHz and using such spectrally efficient modulation format.

Acknowledgements

First and foremost I would like to thank my supervisor, Professor Cyril Renaud, for giving me the opportunity to pursue a Ph.D. in THz communications at University College London (UCL). His guidance and supervision as well as his faith in my ability to carry out research have made this work possible. I would also like to thank my secondary supervisor, Dr. Martyn J. Fice. His insightful suggestions and expertise in communications have been essential for the completion of this thesis. Apart from my supervisors, I wish to express my gratitude to Professor Alwyn J. Seeds, head of the ultra-fast photonics group and Dr. Chin-Pang Liu for their useful discussions.

My sincere thanks to Dr. Haymen Shams for his patience in teaching me all I needed to know about communications. I am also grateful to other current (Dr. Katarzyna Balakier, Dr. Lalitha Ponnampalam, Dr. Chris Graham, Dr. Valeria Vercesi, James Seddon, Ahmad Mohammad) and previous (Dr. Michele Natrella, Dr. Will Yang, Marc Sans) ultra-fast photonics group members for their support and their kindness and friendship, which have made the last few years so splendid.

I would also like to thank Dr. Mira Naftaly and Dr. Irshaad Fatadin for their feedback on all the research outputs of this thesis and making my time at the National Physical Laboratory (NPL) a very enjoyable one.

I could not finish without thanking my girlfriend Ana and my parents Jose Luis and Inmaculada and my sister Julia for having to put up with me all these years (as hard a task as going through the PhD itself). For my amazing time here in London I also thank my friends Miguel, Sergio, Cristina, Eugenia and Jorge.

Contents

1	Introduction	16
1.1	THz communications	16
1.1.1	Why THz?	16
1.2	System considerations	17
1.2.1	FSPL	18
1.2.2	Frequency allocation in the sub-THz band and atmospheric attenuation	19
1.2.3	Applications	21
1.3	THz technology	21
1.3.1	Photonics & electronics	21
1.3.2	Converged optical-wireless access networks	25
1.4	Outline of the thesis	27
1.5	Publications associated with this thesis	28
1.5.1	Main publications of this thesis	28
1.5.2	Other journal publications	28
1.5.3	Other conference proceedings publications	29
2	Literature review	33
2.1	THz applications	33
2.1.1	Fixed links	33
2.1.2	Links requiring automatic beam steering capabilities	37
2.1.3	Distance and data rate requirements	38
2.2	Technology required	40

2.2.1	THz transmitter	40
2.2.2	THz receiver	40
2.3	Phase noise reduction techniques	45
2.3.1	DSP	45
2.3.2	Optical frequency comb filtering	50
2.3.3	Envelope detector-based systems	54
3	Envelope detector-based THz systems	63
3.1	Tx and Rx DSP and experimental arrangement	64
3.1.1	DSP for SSB generation and reception	64
3.1.2	Complete experimental arrangement	68
3.2	Phase robustness and spectral efficiency of SSB signals	71
3.3	Techniques for SSB signal generation	81
3.3.1	Digital virtual SSB (DVSSB) implementation	82
3.3.2	Analog virtual SSB (AVSSB) implementation	83
3.3.3	Simulation results	84
3.3.4	System demonstrations	86
3.4	Summary and conclusions	89
4	THz wireless bridges	94
4.1	Tone-assisted THz wireless bridge	94
4.2	Wireless bridge on a WDM network	101
4.3	Dual wireless channel transmission	103
4.4	40 Gbit/s wireless bridge	106
4.5	Conclusions	110
5	Conclusions and further work	114
5.1	Summary of research	114
5.2	Further work	117
	Acronyms	120

List of Figures

1.1	Atmospheric attenuation at frequencies from 100 GHz to 1 THz. Values calculated for an atmospheric pressure of 101.300 kPa, temperature of 15°C, and a water vapor density of 7.5 g/m ³	20
1.2	Possible applications of THz links in future wireless networks: connecting several access points, access points and end customers and different end customers	22
1.3	Beating of two optical signals in a photomixing device (in this case a PD). The output of two lasers is optically coupled and injected into a PD, that generates a signal at a frequency equal to the frequency difference between the two lasers. For data generation one of the laser outputs is modulated before combining the two lasers outputs. This process is also referred to as heterodyne THz generation. . . .	22
1.4	(a) An optical wireless integrated network,(b) BBoF BS (typical configuration of electronic THz generation), and (c) RoF BS (typical configuration of photonic THz generation)	26
2.1	(a) Current network model where the BS has baseband processing capabilities and serves a large area, and (b) C-RAN concept where the antenna unit is separated from the baseband unit (the CO) and the density of wireless cells is increased	34
2.2	(left) single-hop C-RAN network with THz and fibered links and (right) C-RAN multi-hop network	35
2.3	Wireless bridge	36

2.4	(a) Time-to-space beam steering concept (adapted from [7]) and (b) Time-to-space beam steering concept (adapted from [8]). TDD: true time delay	43
2.5	Sensitivity penalty of the QAM-adapted VV at a BER of 10^{-3} and an optimum block filter length N . The lower x axis shows the linewidth \times symbol product (figure of merit of PE algorithms [24]), while the upper x axis shows the required linewidth per laser (assuming two identical lasers) at a symbol rate of 10 GBd.	47
2.6	Differential decoding process	49
2.7	Photonic THz system with comb generation	51
2.8	Dual-arm OPLL	52
2.9	Stabilization of two OFCG's filter modes with PSs. Adapted from [35].	53
2.10	SSB signal generation using Hilbert transform	55
2.11	Photonic generation and envelope detection of THz SSB signals	57
3.1	Transmitter DSP for the generation of SSB signals.	67
3.2	Receiver DSP for the demodulation of envelope-detected SSB signals.	67
3.3	Typical constellation diagram after (A) normalization, (B) RDE, (C) VV and (D) DD equalizer.	68
3.4	Block diagram of the experimental arrangement for the transmission of SSB THz signals (including the digital ED and the CSPR measurement point). The inset shows the optical spectrum of the generated SSB signal at point A (i.e., after EDFA1).	69
3.5	The spectrum of envelope-detected signals when (a) the guard band between carrier and signal (GB) is equal to the signal passband bandwidth (BW) and (b) when the GB is lower than the BW. In the first case the direct detection terms do not overlap with the down-converted signal after envelope detection and there is no SSBI. On the latter case there is some overlap and hence there is SSBI.	72

- 3.6 BER versus received electrical power for SSB signals with different GBs. The inset shows the optimum CSPR versus the GB. 73
- 3.7 BER versus received electrical power for SSB signals with f_{SC} of 6.25 GHz and different combined optical linewidths. Insets A, B, C, and D: constellation diagrams at the lowest BER value for the 22 kHz, 229 kHz, 493 kHz and 905 kHz linewidths respectively. 75
- 3.8 BER versus received electrical power for SSB signals using the KK receiver. The inset shows the optimum CSPR versus the GB for the two curves taken with the KK receiver. 77
- 3.9 BER at a received electrical power of -4 dBm versus the net ISD of the transmitted SSB signal. 78
- 3.10 BER versus received electrical power for baseband signals and different combined optical linewidths. Insets A, B, C, and D: constellation diagrams at the lowest BER values for 22 kHz, 229 kHz, 493 kHz, and 905 kHz linewidths, respectively. The linear fit for the BER curve obtained for a SSB signal when no emulation was performed is also shown for comparison. N denotes the size of the averaging filter in the VV algorithm. 79
- 3.11 Penalty at the HD-FEC limit due to combined linewidth. In the case of the SSB signals w/ KK receiver, the penalty is assumed to remain constant with linewidth (this is experimentally verified for SSB signals w/o the KK receiver). 80
- 3.12 Optical DVSSB transmitter design. Inset (A) complex spectrum of the off-line digital signal for $f_{SC-DVSSB} = 2.75$ GHz and $f_{T-DVSSB} = -5.5$ GHz and (B) spectrum of the resultant optical signal (resolution bandwidth of 10 MHz). $|f_{T-DVSSB}| = 1/2[GB + S_R(1 + \alpha)]$ and $|f_{SC-DVSSB}| = GB/2$, where GB is the guard band, S_R is the symbol rate and α is the roll-off factor of the RRC filter. 82

3.13	Optical AVSSB transmitter design. Inset (A) complex spectrum of the off-line digital signal, and (B) spectrum of the resultant optical signal for $ f_{T-DVSSB} = 8.25$ GHz (resolution bandwidth of 10 MHz). $ f_{T-DVSSB} = GB + S_R(1 + \alpha)/2$ where GB is the guard band, S_R is the symbol rate and α is the roll-off factor of the RRC filter.	83
3.14	Optical sideband SNR versus CSPR for each technique.	85
3.15	BER versus CSPR for the (A) 5.5 GHz, (B) 4.75 GHz, and (C) 3.5 GHz GBs and at an input optical power to the PD of 12.9 dBm. The normalized GB (GB/BW) is also indicated inside the brackets.	87
3.16	Optimum CSPR versus normalized GB.	88
3.17	BER versus received electrical power for the (A) 5.5 GHz, (B) 4.75 GHz, and (C) 3.5 GHz GBs. The normalized GB is also indicated inside the brackets.	89
3.18	Penalty (taking the lowest received electrical power yielding a BER below the FEC limit on Figure 3.17 as reference) versus normalized GB.	90
4.1	Schematic representation of a wireless bridge based on photonic THz generation.	96
4.2	Receiver DSP including the tone-assisted technique.	97
4.3	Experimental arrangement for single optical/single wireless channel THz bridge.	99
4.4	(a) BER versus PSPR for ECL#1 and DFB#1, and (b) BER curves for the various transmission configurations.	100
4.5	(a) Schematic representation of a wireless bridge embedded on a WDM network and (b) experimental arrangement for multiple optical-/single wireless-channel THz bridge. The inset shows the spectra of the 4 modulated optical channels before fiber transmission.	102
4.6	BER curves for the 4 optical channels.	103

4.7 (a) Schematic representation of a wireless bridge supporting several users and (b) experimental arrangement for multiple optical-/multiple wireless-channels THz bridge. The inset shows the electrical spectra of the received signal at the ONU. 104

4.8 IF response of the Rx RAU (including SHM amplifiers and optical modulator) (blue curve) and combined THz response of UTC and SHM (red curve). 105

4.9 (a) BER curves of the 2 transmitted channels at 4 GBd and 5 GBd (the THz frequency of each channel is shown in the legend); (b) electrical spectrum of the signals received at the ONU for each modulation speed; (c) electrical noise in the Rx RAU. 106

4.10 Digital transmitter and receiver for twin-SSB transmission. 107

4.11 Electrical channel and pre-equalization filter responses 107

4.12 Optical spectra of (a) baseband signal and (b) twin-SSB signal. . . . 108

4.13 BER as a function of the squared photocurrent for twin-SSB (both for conventional approach and split carrier scheme) and baseband signals. The inset shows the BER produced by each of the sidebands in the twin-SSB signal. 110

List of Tables

1.1	Link budget calculation at 300 GHz	19
2.1	Summary of THz applications	44
2.2	Notable THz transmissions with OFCGs	54
3.1	Parameters of components used in the transmission experiments . . .	71
3.2	Summary of SSB techniques	91
4.1	Summary of relevant wireless bridge transmission experiments sup- porting higher order modulation	98

Chapter 1

Introduction

1.1 THz communications

1.1.1 Why THz?

According to Cisco's Visual Networking Index report [1], internet traffic will reach 278 Exabyte per month by 2021 (in 2016, the monthly run rate was 96 Exabyte). The fastest-growing part of this increase is happening on wireless traffic, which is expected to account for 63% of the total traffic by 2019 (it accounted for less than half in 2014). Such an increase in the wireless network capacity will require much higher wireless transmission rates both in the backhaul and access links of the network. In this scenario, 100 Gb/s or even few Tb/s wireless links are expected to become a reality within the next few years [2].

Recently, several spectral windows at mm-wave frequencies¹ (one at the 60 GHz band and four in the 70 GHz - 90 GHz band) have been allocated for wireless communications. The individual bandwidth assigned to these bands, however, is not higher than 9 GHz. To achieve transmission speeds higher than 100 Gb/s with such a constrained bandwidth, very spectrally-efficient modulation formats (modulation order higher than 2048) would be required. The large signal-to-noise ratio (SNR) that these formats need, would set a very stringent requirement on the transmitter power (and also on the system dynamic range). To achieve the envisaged data rates in a power-efficient way, it is, therefore, necessary to go to carrier frequencies where

¹Although not an official designation, the term 'mm-wave' is normally used to refer to frequencies spanning from 30 GHz to 300 GHz.

regulations allow the use of bands with bandwidths of several tens of GHz.

In this context, communications in the sub-THz² band (100 GHz - 1 THz) are envisioned as a key technology since this region of the electromagnetic spectrum is not allocated and can be used entirely for wireless communications. As will be seen in section 1.2.2, there are six atmospheric windows in this region that have bandwidths higher than 40 GHz.

Optical wireless communication (OWC) in the near-infrared (NIR) region is the other competitive wireless solution to achieve high-speed data transmissions. However, OWC links are much more susceptible to: (a) certain environment conditions like fog, (b) airborne particles (like those found in dust and smoke), and (c) refractive index changes caused by local temperature, pressure, or humidity gradients (scintillation) [3]. For example, the attenuation due to fog at NIR frequencies can be more than two orders of magnitude higher than that at sub-THz frequencies [4]. On the other hand, airborne particles and scintillation have minor effects on THz waves due to the large size of THz wavelengths compared to that of smoke particles and NIR wavelengths. Another disadvantage of OWC, is the higher impact of misalignment between transmitter and receiver [5].

Summarizing, sub-THz communication links potentially offer several advantages over competing technologies including higher bandwidth compared to mm-wave links and less attenuation under foggy weather or smoke conditions compared to NIR links. However, there still exist several technology research challenges that need to be overcome to reach a competitive solution. Some of these hurdles arise from the propagation characteristics of THz waves, which will be reviewed in the next section.

1.2 System considerations

When propagating, electromagnetic waves suffer from attenuation due to free-space path loss (FSPL) and molecular absorption. In this section we review the main implications of these effects on sub-THz communication links.

²In this thesis, the terms "THz" and "sub-THz" are used interchangeably.

1.2.1 FSPL

The FSPL is quantitatively described by the Friis transmission formula:

$$\text{FSPL} = \left(\frac{4\pi df}{c} \right)^2, \quad (1.1)$$

where d is the distance between antennas, and f is the radiation frequency. As can be seen from equation 1.1, the FSPL is quadratically proportional to the carrier frequency. The high FSPL at sub-THz frequencies (higher than 100 dB at 300 GHz and a distance of 10 m) together with both the large noise bandwidth associated with high-symbol-rate transmissions and the low power from THz compact sources leads to the need of high-gain antennas.

To illustrate this, in table 1.1, a representative link budget calculation for a carrier frequency of 300 GHz and link distance of 10 m is provided. A transmitter output power of 10 mW is assumed, based on the reported output power of state-of-the-art InP high-electron-mobility transistor (HEMT) monolithic microwave integrated circuit (MMIC) electronic amplifiers at around this frequency [6]. The down-conversion loss is assumed to be 10 dB, which is similar to that of commercially available sub-harmonic mixers (SHMs) based on Schottky barrier diodes (SBDs) [7]. The intermediate frequency (IF) noise figure (NF) is 7 dB—corresponding to a noise power density of -167 dBm/Hz—to account for the amplifier(s) used after down-conversion. Using these values and assuming binary or quadrature phase shift keying (BPSK and QPSK) modulation (both require a SNR per bit— SNR_b —of 6.8 dB to produce a bit error rate—BER—of 10^{-3}), at least an antenna gain of 25 dBi is needed in both transmitter and receiver antennas to allow for 5 dB of implementation penalty. Since high antenna gain implies high directivity, THz systems will be highly directional. This is a major difference from current wireless systems, which rely on quasi-omni-directional antennas and non-directed transmissions and has several implications. The first one is that THz communication will take place predominantly over line-of-sight (LOS) links and, thus, some THz applications will require steerable antennas and active tracking. The second one is that it makes THz

Table 1.1: Link budget calculation at 300 GHz

Parameter	Value	Unit	Comments
Bit rate	20	Gbit/s	
Source power	10	dBm	
Tx antenna gain	25	dBi	
Transmission loss	102	dB	at 300 GHz; link length = 10 m; absorption negligible
Rx antenna gain	25	dBi	
Received power	-42	dBm	
IF power	-52	dBm	10 dB down-conversion loss
N_0	-167	dBm/Hz	IF NF = 7 dB (IF amplifier chain)
SNR_b	12	dB	
Margin	~ 5	dB	c.f. BPSK or QPSK at a BER of 10^{-3} ($SNR_b = 6.8$ dB)

beams very narrow. This can be exploited for different applications like secure communications, as it limits the possibility of eavesdropping ³, or ultra-dense cellular networks, as it enables high spatial reuse.

1.2.2 Frequency allocation in the sub-THz band and atmospheric attenuation

In section 1.1.1, it was said that the electromagnetic spectrum from 100 GHz to 1 THz is not allocated for specific uses yet, however this is not completely true. Current regulation covers frequencies up to 275 GHz. From 100 GHz up to this frequency there are 10 windows allocated for fixed and mobile communications, but none of them with a bandwidth higher than 17 GHz (see Figure 1.1). From 275 GHz onwards no specific regulation exists. However, two passive applications, radio astronomy and satellite-based earth exploration, use a large number of bands in this region. Until specific bands in this range are assigned to wireless communications (this is likely to happen in the 2019 World Radiocommunication Conference), there are two options: constrain THz communication to remaining bands only or share the spectrum with these applications.

³In a recent work by Mittleman and colleagues [8], it was shown that even THz wireless links are susceptible to eavesdropping if a scattering object, which would serve to redirect part of the beam to the attacker's receiver, is placed in the link path. Although the degree of complexity of such attack is still higher than those for lower RF frequencies, this suggests that appropriate counter-measures will be required if a secure THz channel is needed.

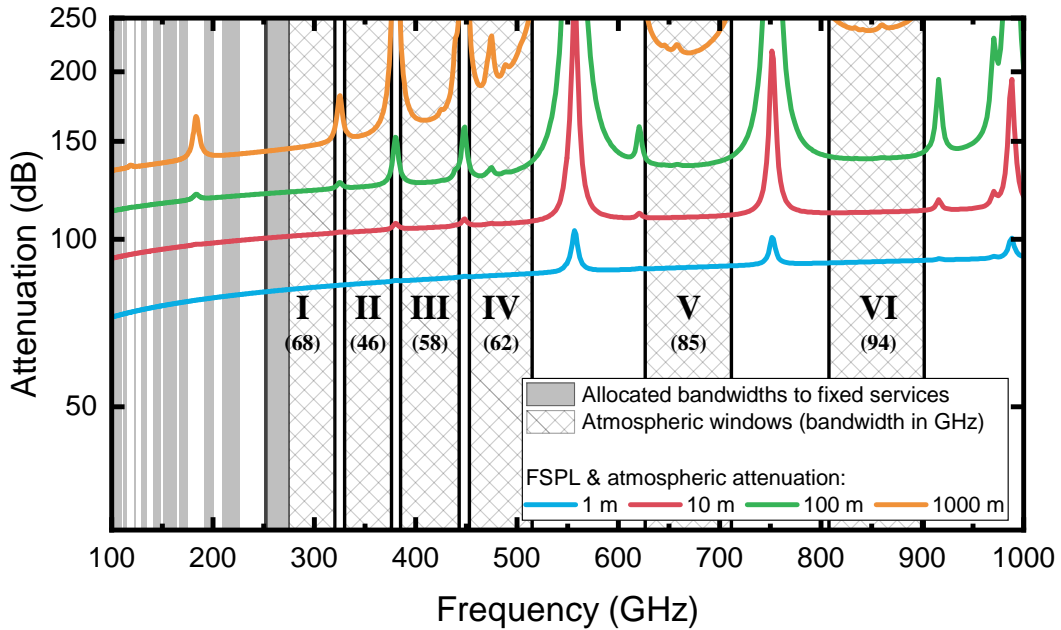


Figure 1.1: Atmospheric attenuation at frequencies from 100 GHz to 1 THz. Values calculated for an atmospheric pressure of 101.300 kPa, temperature of 15°C, and a water vapor density of 7.5 g/m³

First option would make the task of achieving ultra-high data rates a very difficult one due to the small bandwidth, less than 10 GHz [9], of the remaining bands. Therefore, the only way to reach ultrafast wireless communications is to share the spectrum. Although this practice is permitted by the current regulation, "all necessary steps to avoid interference must be taken". As noted in [10], this requirement should not be a problem in the case of radio astronomy since radio telescopes are normally located at isolated places. On the other hand, to avoid interference with earth exploration satellites, the power of THz telecommunication sources should be kept below a threshold that depends on the specific transmission scenario [11]. In chapter 2 we briefly discuss whether this limitation can prevent THz links from achieving the distances required by targeted applications.

If the spectrum is shared, all the spectrum up to 1 THz could be used for communications. In practice, however, atmospheric attenuation of THz waves will ultimately determine the useful transmission windows for THz communications. Atmospheric attenuation of THz waves is mainly caused by water vapor and oxygen absorption. As can be seen from Figure 1.1, there are several windows in the

frequency range from 100 GHz to 1 THz where the atmospheric attenuation is relatively low. The appropriate frequency band for each application will depend on the required transmission distance. Bands I and II may be used for long (1 km - 10 km) and medium (100 m - 1 km) range applications, respectively. Bands III and IV may only be suitable for indoor applications with transmission distances lower than 100 m due to increased atmospheric absorption and the fact that rain attenuation can reach values of up to 100 dB/km at these frequencies [12]. Windows V and VI may be suitable for near field communications (transmission distance lower than 10 cm) [13]. Above 1 THz, because of the many absorption lines of water vapor and other atmospheric gases, seems to be unsuitable for wireless communications.

1.2.3 Applications

THz-communication applications can be divided into two categories: (a) backhaul links⁴ of mobile and optical networks and (b) access links for the distribution of high-definition multimedia services from base stations to end customers (in mobile networks and wireless local access networks, WLANs) and between end customers (in wireless personal access networks, WPANs). In Figure 1.2, a diagram illustrating some examples of these applications is shown. In chapter 2, these applications will be reviewed in more detail together with their main requirements in terms of link distance and data rates as well as the most cost-efficient transceiver technology for each of them.

1.3 THz technology

1.3.1 Photonics & electronics

Since the THz band is an area of convergence between electronics and photonics, there are approaches from both sides of the spectrum with potential to become a commercial solution for THz wireless communications. In this section we review the most important ones for wireless transmitters and receivers.

⁴A backhaul link is any of the links connecting the core network with the access points that provide Internet services to end customers.

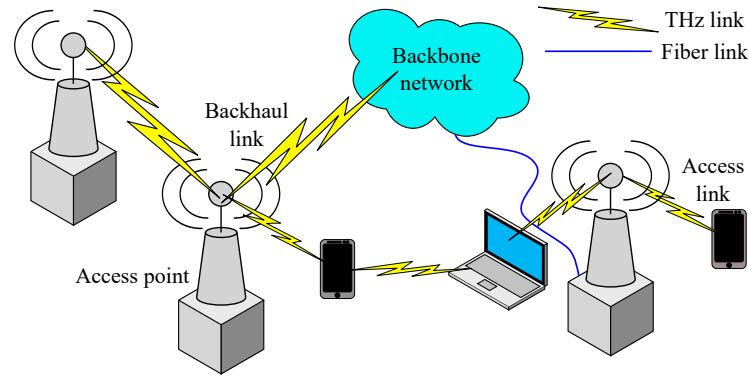


Figure 1.2: Possible applications of THz links in future wireless networks: connecting several access points, access points and end customers and different end customers

1.3.1.1 Transmitter technology

One of the greatest challenges in THz technology is the development of a high-power source. Photonic THz transmitters are based on the beating of two optical modes in a photomixing device (see Figure 1.3 for a more detailed explanation). On the other hand, several electronic technologies for either direct generation or frequency multiplication are being investigated. From these technologies, the most relevant ones for communications are: SBDs, resonant tunneling diodes (RTDs), and transistor-based circuits.

Based on desirable features for wireless transmitters such as portability, low-power consumption, high spectral purity, room temperature operation, low cost and tuneability, one of the most promising techniques for THz generation is photonic

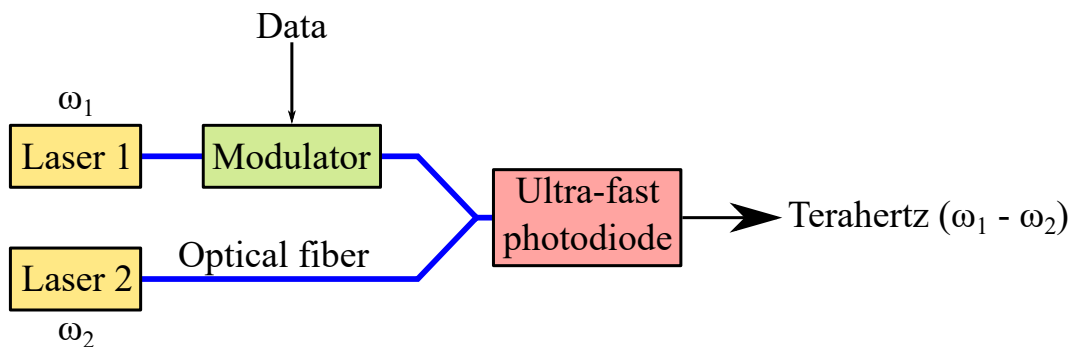


Figure 1.3: Beating of two optical signals in a photomixing device (in this case a PD). The output of two lasers is optically coupled and injected into a PD, that generates a signal at a frequency equal to the frequency difference between the two lasers. For data generation one of the laser outputs is modulated before combining the two lasers outputs. This process is also referred to as heterodyne THz generation.

down-conversion in ultrafast photodetectors (PDs). Using this approach record output powers for frequencies up to 1 THz have been demonstrated [4]. Although it is expected that the power from these devices will not exceed few mW at frequencies around 300 GHz [14], the combination of PDs in arrays is a promising approach to increase the link budget of photonic THz wireless systems [13].

Furthermore, the photomixing approach allows the use of modulators and multiplexing techniques from optical networks to modulate the THz signal. This enables advanced modulation schemes (like vectorial and multi-carrier modulation) to be readily applied to THz signals at very high speeds. In the case of electronic sources, however, the modulation scheme is one of the major drawbacks. On the one hand, the non-linear behavior of multiplication chains limits the amplitude coding at source input. On the other hand, modulating the THz signal at source output, either by using THz SHMs or in-phase/quadrature (IQ) THz modulators will be associated with quite high conversion losses and low modulation indexes [15].

1.3.1.2 Receiver technology

Most of the approaches that are useful as THz emitters for wireless communications can also work as receivers. Currently, from all previously mentioned techniques, SBD-based SHMs remain more efficient than competing technologies [16]. However, transistor-based receivers have also been used in various THz transmission experiments showing very good performance (64 Gb/s at a distance of 850 m and a carrier frequency of 240 GHz [17]) and on-going research is being carried out in ultrafast PDs for optical down-conversion of THz waves [18]. RTDs have been also demonstrated as receivers [19].

1.3.1.3 Future prospects and challenges

There is a need for amplification both at the transmitter and receiver side to combat the high FSPL that exists at THz frequencies. The development of THz amplifiers is therefore a top priority in THz technology and one of the most active areas of THz research [5]. From the technologies considered in this work (i.e., relevant to communications), the highest output power reported at THz frequencies has been achieved with InP transistor-based amplifiers (both HEMTs and heterojunc-

tion bipolar transistor, HBT, InP amplifier circuits have achieved output powers of about 10 dBm at frequencies around 300 GHz [20]).

Apart from amplification, there are other areas of active research which aim either to increase the link budget or reduce production costs. Below are a few of them regarding photonic technologies:

- *Photonic integration.* The main elements to be integrated from Figure 1.3 are the two lasers and the modulator, as depending on the application (see section 1.3.2) the ultra-fast PD can be a standalone component. Photonic integrated systems, compared to those based on discrete components, have lower coupling losses, and, thus, higher power efficiency. Monolithic integration of these components on a III-V material such as InP is normally the solution of choice. Photonic integration can also lead to lower THz signal phase noise as the two lasers encounter the same environmental fluctuations [21]. Although photonic integration is more and more accessible due to the proliferation of multi-wafer foundry platforms, the development of a fully-integrated dual laser source with RF synthesizer-like performance is still a challenge. The integration of the ultra-fast PD with the rest of the photonic components is also a challenge, as it typically uses a significantly different set of epilayers. However, recent progress on integration techniques has enabled the first development of a fully-photonic transmitter chip for operation at mm-wave frequencies (from 3 GHz to 120 GHz) [22].
- *Development of Si photonics integrated technology.* Here we distinguish between two trends: first the development of active Si integrated components and second the development of techniques for integrating passive Si elements with III-V active components. The main drivers for this are associated with the large production capabilities of Si and its low optical propagation losses. This last feature will be essential for the development of electronically steerable antenna-integrated PDs arrays [23]. Si photonics would also enable the easy and cheap integration with Si electronic components.

- *Increasing PD power.* Either by improving single PD performance characteristics, in terms of saturation current and thermal management, or by developing antenna-integrated PDs arrays.

On the electronic side, areas of interest include:

- *Pushing Si integrated technology oscillation frequencies.* While reported InP HEMT oscillation frequencies have exceeded 1 THz [20], the maximum frequency of SiGe and Si complementary metal-oxide-semiconductor (CMOS) integrated circuits is around 700 GHz resulting in powers 10 dB lower than those reported for InP chips at the 300 GHz band for example [24]. Considering the mass production capabilities of this technology, pushing this frequency will be key for realizing practical electronic sources.
- *Integration of InP with Si.* This would allow to combine the high power capabilities of InP technology with the large fabrication capacity of the Si industry.

1.3.2 Converged optical-wireless access networks

Trends indicate that optical and wireless networks will converge to a highly integrated network with a common optical feeder backbone [25] as depicted in Figure 1.4(a). A promising candidate for the optical feeder part of this converged network is the passive optical network (PON). In a PON, a single feeder fibre of up to 90 km is used to connect a central office (CO) to multiple drop fibres that terminate in optical network units (ONUs) without the use of any active devices such as routers. In the ONUs, which are placed at the customer premises, the optical signal is converted to an electrical one for use in phones, computers, TVs... In a converged wireless-optical network, the PON would also feed a number of base stations (BSs) that would provide wireless connectivity to both mobile and nomadic users in WLANs and WPANs respectively. In traditional networks, links at the low microwave region have remained as the popular choice over optical fibre backhaul options due to their associated advantages of faster deployment and cost-effectiveness. However, such advantages are becoming weaker due to the increasingly easier access to existing or planned fibre routes and, most importantly,

the scarcity of bandwidth at low microwave bands [26]. In this context, an advantage of photonic-based THz sources over electronic-based ones, is their seamless integration with optical fibre, which would enable direct installation of photonic-based BSs in such a hybrid network. This can be understood by looking at Figures 1.4(b) and (c). Radio-over-fibre (RoF), in comparison to the alternative technique of baseband-over-fibre (BBoF), reduces BS functionality to photo-detection and amplification. This offers the benefits of centralised control and also minimises the power consumption and the cost of the BSs. In mobile networks literature, these reduced-functionality BSs are referred to as remote antenna units (RAUs).

These advantages will be key in future cellular networks because of the large number of BSs that will be required in the next generation of mobile telecommunications. Moreover, due to the high data rates that are envisaged for THz communications, it is very likely that in the BBoF scheme, some digital signal processing (DSP) will be required in the BS after recovering the baseband data and before up-converting to THz in order to compensate for transmission impairments [27]. This will add some latency to the link that may be critical for achieving fast handover procedures. In RoF, on the other hand, this latency is minimized since digital signal processors are only placed at the edges of the link (i.e. at the CO and the THz receiver).

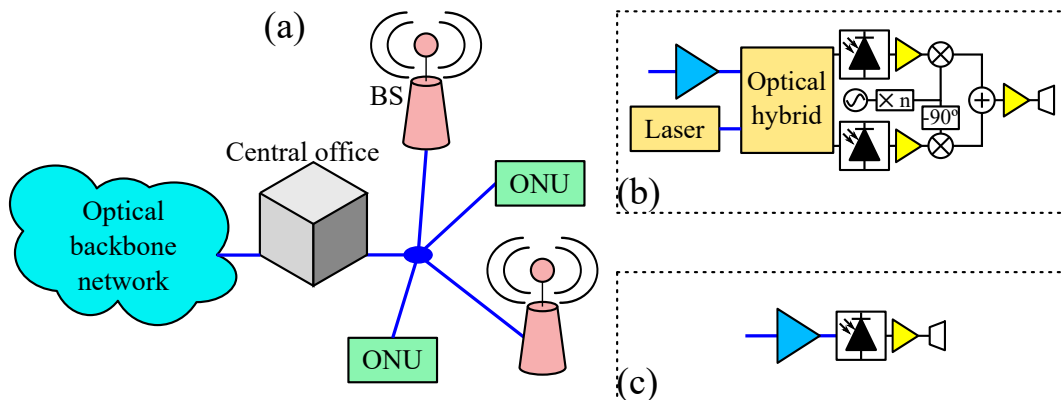


Figure 1.4: (a) An optical wireless integrated network, (b) BBoF BS (typical configuration of electronic THz generation), and (c) RoF BS (typical configuration of photonic THz generation)

1.4 Outline of the thesis

In sections 1.3.1 and 1.3.2, a comparison between electronics and photonics approaches for THz generation has been carried out, paying special attention to their prospects in future converged networks. In spite of how technology progresses in each field, it is clear that the concept of photomixing offers several advantages when a seamless integration with fibre optics is required. Based on this premise, the use cases that are more likely to benefit from an optical interface are identified in the first part of chapter 2 after a detail review of the envisaged applications of THz communications. Based on the distance and data rate requirements of these applications, chapter 2 goes on to discuss the most suitable receiver technology in each of them. In the second part of chapter 2, techniques for phase noise mitigation in coherent THz systems are discussed.

In chapter 3, a system based on an envelope detector (ED) and supporting higher order modulation is proposed. Fundamental aspects of such system, such as the carrier-to-sideband power ratio (CSPR), signal-signal beat interference (SSBI), and phase noise sensitivity are discussed and analyzed. After this, the use of SSBI cancellation algorithms at the digital receiver is proposed as a mean to increase the spectral efficiency of ED systems. A THz system using the Kramers-Kronig (KK) algorithm is then experimentally demonstrated. Finally, the phase robustness of such system is compared with that of a heterodyne system using carrier recovery in the receiver. In the second part of chapter 3, several single sideband (SSB) optical techniques that relax the analog bandwidth requirement of the Tx digital-to-analog converter (DAC) are introduced to the field of photonic THz communications. The performance of such techniques is analyzed by means of numerical simulations and their end-to-end implementation in a THz system is experimentally demonstrated.

Chapter 4 focuses on the realization of high capacity THz wireless bridges. In this case, the analog tone-assisted technique is used to combat the phase noise of the various free-running lasers used throughout the link. The wireless bridge is demonstrated in several scenarios ((a) single channel transmission, (b) wavelength division multiplexing (WDM) network, and (c) multiple-user support capability) for

each of which the link configuration is slightly modified according to the specific requirements. The last part of this chapter discusses the configuration and DSP required to achieve a 40 Gbit/s wireless bridge.

In chapter 5 the thesis is summarized and potential lines for future research are identified

1.5 Publications associated with this thesis

1.5.1 Main publications of this thesis

1. L. Gonzalez-Guerrero, H. Shams, I. Fatadin, M. J. Fice, M. Naftaly, A. J. Seeds, and C. C. Renaud, 35 Gbit/s wireless bridge operating at 250 GHz and supporting multiple users, in preparation for *J. Light. Technol.*
2. L. Gonzalez-Guerrero, H. Shams, I. Fatadin, M. J. Fice, M. Naftaly, A. J. Seeds, and C. C. Renaud, Comparison of Optical Single Sideband Techniques for THz-over-fiber Systems, accepted for *IEEE Trans. Terahertz Sci. Technol.* DOI: 10.1109/TTHZ.2018.2884736. Available from: <http://ieeexplore.ieee.org/stamp/stamp.jsp?tp=&arnumber=8570768&isnumber=5741778>.
3. L. Gonzalez-Guerrero, H. Shams, I. Fatadin, M. J. Fice, M. Naftaly, A. J. Seeds, and C. C. Renaud, Single sideband signals for phase noise mitigation in wireless THz-over-fibre systems, *J. Light. Technol.*, vol. 36, no. 19, pp. 45274534, 2018.

1.5.2 Other journal publications

1. H. Shams, K. Balakier, L. Gonzalez-Guerrero, M. J. Fice, L. Ponnampalam, C. Graham, C. C. Renaud, and A. J. Seeds, Optical Frequency Tuning for Coherent THz Wireless Signals, *J. Light. Technol.*, vol. 36, no. 19, pp. 46644670, 2018.
2. H. N. Parajuli, H. Shams, L. G. Gonzalez, E. Udvary, C. Renaud, and J. Mitchell, Experimental demonstration of multi-Gbps multi sub-bands FBMC transmission in mm-wave radio over a fiber system, *Opt. Express*, vol. 26, no. 6, pp. 73067312, 2018.
3. H. Shams, M. J. Fice, L. Gonzalez-Guerrero, C. C. Renaud, F. Van Dijk, and A. J. Seeds, Sub-THz wireless over fiber for frequency band 220-280 GHz, *J. Light. Technol.*, vol. 34, no. 20, pp. 47864793, 2016.
4. L. Gonzalez-guerrero, H. Shams, J. Martyn, A. J. Seeds, and C. C. Renaud, Linewidth Tolerance for THz Communication Systems Using Phase Estimation Algorithm, in *IEEE Topical Meeting on Microwave Photonics (MWP)*, 2016.

1.5.3 Other conference proceedings publications

1. L. Gonzalez-Guerrero, K. Balakier, M. Thakur, H. Shams, M. J. Fice, A. J. Seeds and C. C. Renaud, Photonic systems for tunable mm-wave and THz wireless communications, accepted for Proceeding of SPIE, 2019.
2. L. G. Guerrero, H. Shams, I. Fatadin, M. J. Fice, M. Naftaly, J. Alwyn, and C. C. Renaud, Spectrally Efficient SSB signals for W-band Links Enabled by Kramers-Kronig Receiver, in Optical Fiber Communcation, 2018, pp. 13.
3. L. Gonzalez Guerrero, H. Shams, J. Martyn, A. J. Seeds, C. C. Renaud, I. Fatadin, and M. Naftaly, Experimental Investigation of Phase Noise Tolerance of SSB THz Signals, in IEEE Topical Meeting on Microwave Photonics (MWP), 2017.
4. M. Fice, H. Shams, Z. Yang, L. Gonzalez-Guerrero, M. Natrella, C. Renaud, and A. Seeds, Photonic generation and distribution of coherent multiband THz wireless signals, 2017 11th Eur. Conf.
5. H. Shams, L. Gonzalez-Guerrero, M. Fice, Z. Yang, C. Renaud, and A. Seeds, Distribution of multiband THz wireless signals over fiber, in Proceeding of SPIE, 2017, no. January 2017.

Bibliography

- [1] Cisco and/or its affiliates. The Zettabyte Era: Trends and Analysis. Technical Report June 2017, 2017.
- [2] Ian F. Akyildiz, Josep Miquel Jornet, and Chong Han. Terahertz band: Next frontier for wireless communications. *Physical Communication*, 12:16–32, 2014. ISSN 18744907. doi: 10.1016/j.phycom.2014.01.006. URL <http://dx.doi.org/10.1016/j.phycom.2014.01.006>.
- [3] John Federici and Lothar Moeller. Review of terahertz and subterahertz wireless communications. *Journal of Applied Physics*, 107(11), 2010. ISSN 00218979. doi: 10.1063/1.3386413.
- [4] Alwyn J. Seeds, Haymen Shams, Martyn J. Fice, and Cyril C. Renaud. TeraHertz photonics for wireless communications. *Journal of Lightwave Technology*, 33(3):579–587, 2015. ISSN 07338724. doi: 10.1109/JLT.2014.2355137.
- [5] Tadao Nagatsuma, Kazuki Oogimoto, Yuki Inubushi, and Jiro Hirokawa. Practical considerations of terahertz communications for short distance applications. *Nano Communication Networks*, 10:1–12, 2016. ISSN 18787789. doi: 10.1016/j.nancom.2016.07.005. URL <http://dx.doi.org/10.1016/j.nancom.2016.07.005>.
- [6] Vesna Radisic, William R. Deal, Kevin M.K.H. Leong, X. B. Mei, Wayne Yoshida, Po Hsin Liu, Jansen Uyeda, Andy Fung, Lorene Samoska, Todd Gaier, and Richard Lai. A 10-mW submillimeter-wave solid-state power-amplifier module. *IEEE Transactions on Microwave Theory and Techniques*, 58(7 PART 2):1903–1909, 2010. ISSN 00189480. doi: 10.1109/TMTT.2010.2050105.
- [7] Virginia Diodes. Mixers - VDI Model: WR3.4SHM. URL <https://www.vadiodes.com/en/products/mixers?id=128>.
- [8] Jianjun Ma, Rabi Shrestha, Jacob Adelberg, Chia Yi Yeh, Zahed Hossain, Edward Knightly, Josep Miquel Jornet, and Daniel M. Mittleman. Security and eavesdropping in terahertz wireless links. *Nature*, 563(7729):89–93, 2018. ISSN 14764687. doi: 10.1038/s41586-018-0609-x. URL <http://dx.doi.org/10.1038/s41586-018-0609-x>.
- [9] Thomas Kürner and Sebastian Priebe. Towards THz communications - Status in research, standardization and regulation. *Journal of Infrared, Millimeter, and Terahertz Waves*, 35(1):53–62, 2014. ISSN 18666906. doi: 10.1007/s10762-013-0014-3.
- [10] Ho Jin Song and Tadao Nagatsuma. Present and future of terahertz communications. *IEEE Transactions on Terahertz Science and Technology*, 1(1):256–263, 2011. ISSN 2156342X. doi: 10.1109/TTHZ.2011.2159552.
- [11] Sebastian Priebe, David M. Britz, Martin Jacob, Stephen Sarkozy, Kevin M.K.H. Leong, Jennifer E. Logan, Ben S. Gorospe, and Thomas Kürner. Interference investigations of active communications and passive earth exploration services in the

- THz frequency range. *IEEE Transactions on Terahertz Science and Technology*, 2(5): 525–537, 2012. ISSN 2156342X. doi: 10.1109/TTHZ.2012.2208191.
- [12] Radoslaw Piesiewicz, Thomas Kleine-Ostmann, Norman Krumbholz, Daniel Mittleman, Martin Koch, Joerg Schoebei, and Thomas Kürner. Short-range ultra-broadband terahertz communications: Concepts and perspectives. *IEEE Antennas and Propagation Magazine*, 49(6):24–39, 2007. ISSN 10459243. doi: 10.1109/MAP.2007.4455844.
- [13] Tadao Nagatsuma. Photonics-enabled terahertz communications towards terabit/s. In *2015 International Topical Meeting on Microwave Photonics, MWP 2015 - Conference Proceedings*, pages 10–13, 2015. ISBN 9781467393683. doi: 10.1109/MWP.2015.7356684.
- [14] Alwyn Seeds, Haymen Shams, Martyn Fice, Katarzyna Balakier, Lalitha Ponnampalam, and Cyril Renaud. Prospects for millimetre-wave-over-fibre and THz-over-fibre systems. In *Proceedings of SPIE*, volume 9387, page 938702, 2015. ISBN 9781628414776. doi: 10.1117/12.2077150. URL <http://proceedings.spiedigitallibrary.org/proceeding.aspx?doi=10.1117/12.2077150>.
- [15] Guillaume Ducournau, Pascal Szriftgiser, Fabio Pavanello, Emilien Peytavit, Mohammed Zaknoue, Denis Bacquet, Alexandre Beck, Tahsin Akalin, Jean Francois Lampin, and Jean Francois Lampin. THz Communications using Photonics and Electronic Devices: the Race to Data-Rate. *Journal of Infrared, Millimeter, and Terahertz Waves*, 36(2):198–220, 2015. ISSN 18666906. doi: 10.1007/s10762-014-0112-x.
- [16] Tadao Nagatsuma, Guillaume Ducournau, and Cyril C. Renaud. Advances in terahertz communications accelerated by photonics. *Nature Photonics*, 10(6):371–379, 2016. ISSN 17494893. doi: 10.1038/nphoton.2016.65. URL <http://dx.doi.org/10.1038/nphoton.2016.65>.
- [17] Ingmar Kallfass, Florian Boes, Tobias Messinger, Jochen Antes, Anns Inam, Ulrich Lewark, Axel Tessmann, and Ralf Henneberger. 64 Gbit/s Transmission over 850 m Fixed Wireless Link at 240 GHz Carrier Frequency. *Journal of Infrared, Millimeter, and Terahertz Waves*, 36(2):221–233, 2015. ISSN 18666906. doi: 10.1007/s10762-014-0140-6.
- [18] Cyril C. Renaud, Martyn J. Fice, Lalitha Ponnampalam, Michele Natrella, Chris Graham, and Alwyn J. Seeds. Uni-travelling carrier photodetectors as THz detectors and emitters. *SPIE Proceedings*, 9370:93700B, 2015. ISSN 1996756X. doi: 10.1117/12.2080195. URL <http://proceedings.spiedigitallibrary.org/proceeding.aspx?doi=10.1117/12.2080195>.
- [19] Tadao Nagatsuma. Terahertz communications technologies based on photonic and electronic approaches. *European Wireless, 2012. EW. 18th European ...*, pages 18–21, 2012. URL http://ieeexplore.ieee.org/xpls/abs_all.jsp?arnumber=6216864.
- [20] Miguel Urteaga, Zach Griffith, Munkyo Seo, Jonathan Hacker, and Mark J.W. Rodwell. InP HBT Technologies for THz Integrated Circuits. *Proceedings of the IEEE*, 105(6):1051–1067, 2017. ISSN 00189219. doi: 10.1109/JPROC.2017.2692178.
- [21] Guillermo Carpintero, Efthymios Rouvalis, Katarzyna Ławniczuk, Martyn Fice, Cyril C. Renaud, Xaveer J. M. Leijtsens, Erwin A. J. M. Bente, Mourad Chitoui, Frederic Van Dijk, and Alwyn J. Seeds. 95GHz millimeter wave signal generation using an arrayed waveguide grating dual wavelength semiconductor laser. *Optics Letters*, 37(17):3657, 2012. ISSN 0146-9592. doi: 10.1364/OL.37.003657. URL <https://doi.org/10.1364/OL.37.003657>.

- [//www.osapublishing.org/abstract.cfm?URI=ol-37-17-3657](http://www.osapublishing.org/abstract.cfm?URI=ol-37-17-3657).
- [22] Frederic Van Dijk, Gael Kervella, Marco Lamponi, Mourad Chtioui, Francois Lelarge, Eric Vinet, Yannick Robert, Martyn J. Fice, Cyril C. Renaud, Alvaro Jimenez, and Guillermo Carpintero. Integrated InP heterodyne millimeter wave transmitter. *IEEE Photonics Technology Letters*, 26(10):965–968, 2014. ISSN 10411135. doi: 10.1109/LPT.2014.2309353.
- [23] S. S. Dhillon, M. S. Vitiello, E. H. Linfield, A. G. Davies, Matthias C. Hoffmann, John Booske, Claudio Paoloni, M. Gensch, P. Weightman, G. P. Williams, E. Castro-Camus, D. R.S. Cumming, F. Simoens, I. Escorcia-Carranza, J. Grant, Stepan Lucyszyn, Makoto Kuwata-Gonokami, Kuniaki Konishi, Martin Koch, Charles A. Schmuttenmaer, Tyler L. Cocker, Rupert Huber, A. G. Markelz, Z. D. Taylor, Vincent P. Wallace, J. Axel Zeitler, Juraj Sibik, Timothy M. Korter, B. Ellison, S. Rea, P. Goldsmith, Ken B. Cooper, Roger Appleby, D. Pardo, P. G. Huggard, V. Krozer, Haymen Shams, Martyn Fice, Cyril Renaud, Alwyn Seeds, Andreas Stühr, Mira Naftaly, Nick Ridler, Roland Clarke, John E. Cunningham, and Michael B. Johnston. The 2017 terahertz science and technology roadmap. *Journal of Physics D: Applied Physics*, 50(4), 2017. ISSN 13616463. doi: 10.1088/1361-6463/50/4/043001.
- [24] Ullrich R Pfeiffer, Ritesh Jain, Janusz Grzyb, Stefan Malz, Phillip Hillger, and Pedro Rodr. Current Status of Terahertz Integrated Circuits from Components to Systems. *IEEE BiCMOS and Compound Semiconductor Integrated Circuits and Technology Symposium (BCICTS)*, pages 1–7, 2018.
- [25] A. Gamage; Christina Lim; Dalma Novak; Rodney Waterhouse Ampalavanapillai, Nirmalathas; Prasanna. Digitized Radio Over Fiber Technologies for Converged Optical Wireless Access Network. *Journal of Lightwave Technology*, 28(16):2366 – 2375, 2010. ISSN 0733-8724. doi: 10.1109/JLT.2010.2051017. URL <http://bit.ly/I8XPG3>.
- [26] Christina Lim, Ampalavanapillai Nirmalathas, Masuduzzaman Bakaul, Prasanna Gamage, Ka Lun Lee, Yizhuo Yang, Dalma Novak, and Rod Waterhouse. Fiber-wireless networks and subsystem technologies. *Journal of Lightwave Technology*, 28(4):390–405, 2010. ISSN 07338724. doi: 10.1109/JLT.2009.2031423.
- [27] Kawanishi. Transparent Waveform Transfer for Resilient and Low-latency Links. Technical Report August, 2014.

Chapter 2

Literature review

In this chapter, we isolate the expected applications for a THz link and describe in detail the key technological choices to be implemented for the system to be operational.

2.1 THz applications

In this section, the main applications of THz communications are reviewed. A brief description of each application is provided first and then the distance and data rate requirements are discussed. The information on this section is based mainly on the documents published by the standardization community (especially by the THz Interest Group launched by the Institute of Electrical and Electronics Engineers [1]) such as [2, 3, 4, 5, 6]. Where information has been derived from other sources, this is properly indicated throughout the text. THz links can be divided in two main groups: fixed links and links requiring active tracking.

2.1.1 Fixed links

In these links the position of the receiver is known and, thus, active tracking is not required. The alignment is performed during the installation process by radio engineers. Note that, depending on the application, some of these links may require to communicate with several receivers located in different (fixed) positions. This can be achieved through either time-to-space [7] or frequency-to-space [8] beam steering.

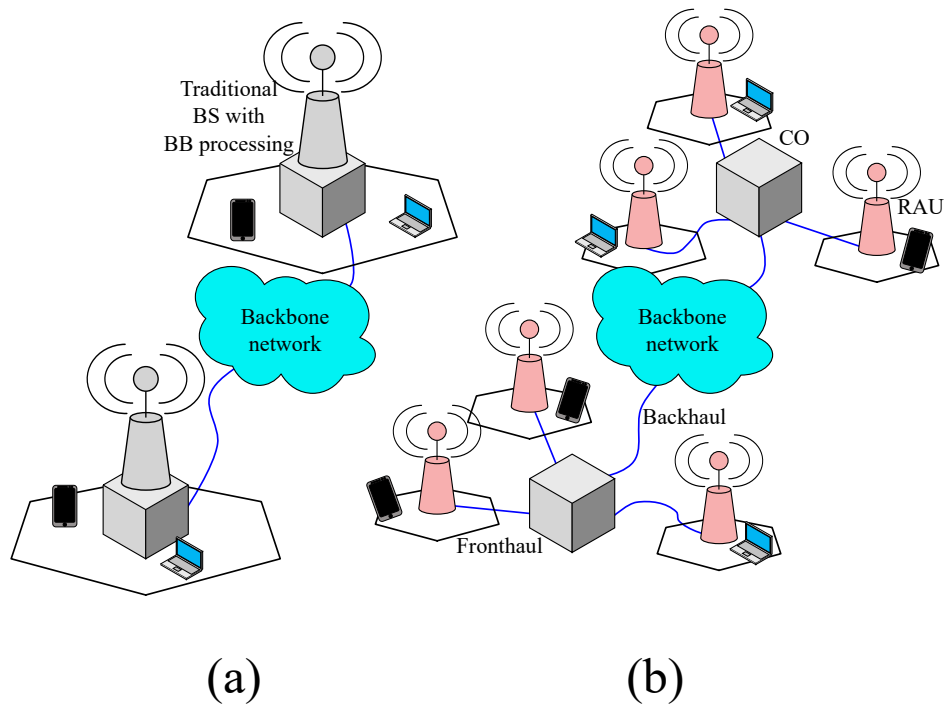


Figure 2.1: (a) Current network model where the BS has baseband processing capabilities and serves a large area, and (b) C-RAN concept where the antenna unit is separated from the baseband unit (the CO) and the density of wireless cells is increased

2.1.1.1 Mobile fronthauling and backhauling

To review the applications that are envisaged for THz wireless links it is necessary to recall the concept of converged optical wireless network that was presented in section 1.3.2. This model of network, which is referred to as cloud-radio access network (C-RAN), has two fundamental aspects: on the one hand, the use of a common optical feeder part and, on the other hand, the centralization of computational resources in the CO. Compared to the current network model (see Figure 2.1), these two properties enable the management of a higher number of antennas from a unique centralized unit (i.e. the C-RAN can be seen as the physical separation of the antenna element and the baseband processing unit). This is a key advantage as the density of wireless cells per unit area continues increasing to support the data rates (see slide 38 of [9]).

As shown in Figure 2.1(b), the link connecting the CO with the RAU is called fronthaul link whereas the link connecting the CO with the network backbone is referred to as backhaul link. As said in section 1.3.2, optical fibre is becoming the

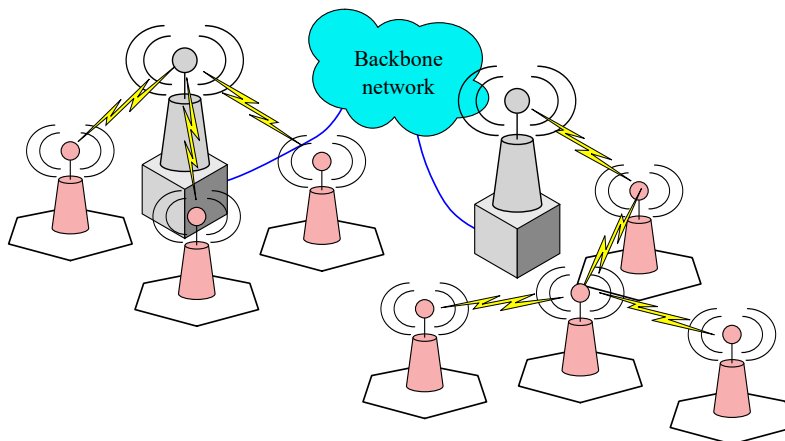


Figure 2.2: (left) single-hop C-RAN network with THz and fibered links and (right) C-RAN multi-hop network

most popular solution for this type of links. However, there are certain situations where its deployment may not be economical as for example in crowded urban areas or old historical areas. In this cases, large bandwidth wireless links might offer better prospects than optical fibre.

In the typical C-RAN arrangement the CO is connected directly to all RAUs (Figure 2.2 (left)). This fronthaul configuration is referred to as single-hop scheme. In the cases where connecting all the RAUs to the CO is not possible (this may be the case in dense urban areas), the implementation of a multi-hop network may be the best solution. In this concept, only few RAUs will be connected directly to the CO. These units will then forward the data packets to neighboring RAUs through wireless links as in Figure 2.2 (right).

2.1.1.2 Wireless bridges

Wireless bridges refer to wireless links connecting two portions of a fiber link. Unlike in mobile fronthaul or backhaul links, the signal is not demodulated in the Rx RAU but rather up-converted to the optical domain and then transmitted to a ONU through an extra portion of fiber as illustrated in Figure 2.3. In [10], three case scenarios where a high-speed wireless bridge could be useful are identified: (a) protection links in case of disasters and subsequent recovery, (b) entrance links in rural areas where optical fiber cannot be deployed and (c) temporal link to provide network connections to small areas that are densely populated in case of large

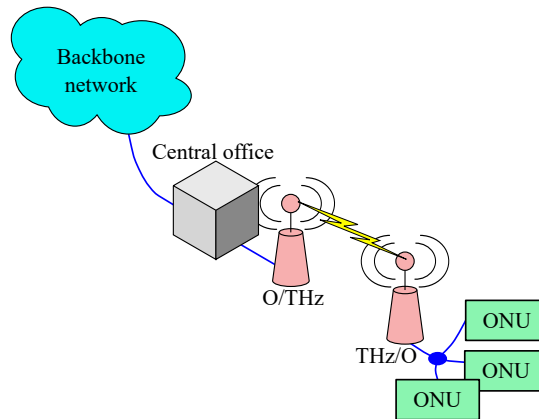


Figure 2.3: Wireless bridge

events, evacuation sites for disaster recovery, etc. Furthermore, these links could be useful in university campuses, technology parks, etc. to interconnect the multiple LANs forming the campus network.

2.1.1.3 Data centres

This is an application that has received significant attention by the THz community [11]. Data centers contain racks equipped with various servers including storage and multiple switches. Today fiber optics is still the preferred option to connect the racks and the servers within a rack. However, pure wired data centers are static and cannot be easily reconfigured following the requirements from dynamic traffic conditions. In addition to this, the large amounts of cables complicate the processes of maintaining and cooling the data center. For these reasons, the introduction of ultra-high data rate wireless is considered as an attractive alternative currently explored at 60 GHz [9]. THz communication, on the other hand, could enable far higher data rates with comparable prerequisites and under the same conditions. Unlike previous fixed links, the deployment of data center links will be indoors.

2.1.1.4 Chip-to-chip communications

This application refers to wireless links inside computers or any other electronic devices. It is of high relevance because wired connectors and microstrip lines on printed circuit boards are likely to become a bottleneck of upcoming bus systems and inter-chip connections.

2.1.2 Links requiring automatic beam steering capabilities

In this group of applications, the receiver will be in a portable device and, hence, active tracking capabilities will be required at the transmitter to follow the receiver and find alternative routes when shadowing of the LOS path occurs due to moving people or objects.

2.1.2.1 THz access points

Cell networks based on THz technology, although one of the most desirable THz applications, is also the most challenging one. This is due to the highly dynamic environment associated with mobile access [12]. According to [13], due to the limited coverage expected from THz stations in this kind of environment (unlikely to exceed few meters), regular cell design will be very difficult to achieve with THz technology, at least in the classic sense of a cell. Hence, it is more likely to have indoor and outdoor THz hotspots providing super-fast access only within a very limited range (nomadic access) rather than continuous access (mobile access). In this scenario it is likely that future mobile cells will emit at different frequencies, providing THz connectivity only when the user is in very close proximity (see slide 43 of [9] for a visual depiction of this concept).

2.1.2.2 Kiosk downloading

This is another application that has attracted the attention of the THz community as it is expected to create an early marketplace [14]. It consists of content synchronization and file exchange with the cloud through terminals called data kiosks. Compared to conventional hotspots that are supposed to offload the traffic while the mobile terminal is in the hotspot range, kiosk downloading is primarily for applications supporting data prefetching (i.e. pre-downloading data in readiness for later use). Two possible case scenarios are envisaged for this application: in the first one, the user stops in front of the terminal placing the mobile phone close to the kiosk; in the second one, the user touches the specified spot but does not fully stop (like for instance when walking through gates in train stations). In any case the link duration in both cases is very short. Apart from train stations the kiosk terminals would be

typically located in public areas such as airports, malls, convenience stores, rental video shops, libraries, and public telephone boxes.

2.1.3 Distance and data rate requirements

Cell distances of current mobile networks, range from 250 m in urban micro cells to 500 m in urban macro cells [15]. It is likely, hence, that the size of future cells will range from tens of meters up to 100 m. In such case, THz fronthaul links in the multi-hop configuration will need to reach, at least, that distance. For fronthaul links in the single-hop configuration and backhaul links, distances as long as 1 km and few km will be required, respectively. In the case of wireless bridges, link distances will range from few hundred of m (technology parks and campus network links) up to few km (rural area-entrance, recovery, and event-coverage links). As for data centers, required distances will vary, depending on the switch configuration, between 10 m and 100 m for inter-rack links and between few cm and hundreds of cm for intra-rack links. On the other hand, for intra-chip communications, links are not likely to exceed few cm. In the case of THz hotspots and data kiosks, targeted distances can be expected to be in the range of few m and few cm, respectively (in the case of data kiosks, such a limited distance will be preferred to avoid interference between neighboring stations).

Taking into account the speed targets that have been set for 5G and extrapolating into the future, one can get an idea of the capacity that will be required from future wireless systems. Since 5G aims to deliver data rates between 1 Gbit/s and 5 Gbit/s for WLANs users and 100 Mbit/s for mobile users [16], it is probable that for the next generation data rates of around few tens of Gbit/s and 1 Gbit/s will be required for WLAN and mobile users respectively.

With these figures in mind one can expect, then, several tens of Gbit/s from fronthaul links. It should be noted that, although the current standard for fronthaul links defines a maximum data rate of 10 Gbit/s, a revision of this standard is in the agenda of the World Radiocommunication Conference of 2019 where it will probably be modified to support higher data rates. As for backhaul links, similarly as for wireless bridges, data rates ranging from several tens of Gbit/s up to 100 Gbit/s

are to be expected. On the other hand, aggregation of 10 Gbit/s links is currently being used in data centers, so data rates of at least several tens of Gbit/s will be required for inter-rack connections. Regarding chip-to-chip communications, data rates up to Tbit/s are specified in a current standard, so, although it will not always be necessary to support Tbit/s speeds, ultra-fast transmissions with data rates in the order of 100 Gbit/s will be required.

If a data rate of a few tens of Gbit/s per user is required in future WLANs, then, an indoor THz hotspot should be able to provide this speed. For outdoor THz hotspots, a data rate of around 10 Gbit/s might be enough to accommodate several users. As for data kiosks, the THz Interest Group suggests data rates in the range of several Gbit/s to allow for a quick download of the contents. For instance, to download a 114 minutes high-definition video in 3 seconds, which is the response time that 83% people can wait without stress, a data rate of 28 Gbit/s is necessary. Even higher data rates will be required for the use case where the user does not fully stop in front of the kiosk.

Before moving on to the next section, it is necessary to discuss the potential limitations imposed by the frequency conflict with earth exploration (see section 1.2.2). In [17], calculations of achievable distances and data rates for safe levels of transmitter power were performed. In the case of fixed links, distances of 867 m and 710 m were found for data rates of 40 Gbit/s (carrier frequency of 310 GHz) and 80 Gbit/s (carrier frequency of 350 GHz) respectively. Regarding THz hotspots, a distance of 33 m was obtained assuming a data rate of 40 Gbit/s and a carrier frequency of 310 GHz. Considering the required distance and data rate values highlighted previously for each application, these figures are likely to be acceptable in all the cases, where link limitations are more likely to come from technological considerations. It is important to note, however, that the calculations above are based on a pure SNR analysis. Generally, a better system performance and, hence, higher transmission distances or data rates can be achieved with DSP techniques such as pulse-shaping filters or forward error correction (FEC), which relate to an enhanced system sensitivity.

2.2 Technology required

In this section we review the different technology options that are available for THz systems and attempt to determine which one suits best the distance and data rate requirements of each application.

2.2.1 THz transmitter

For the transmitter, there are two main options: emitters based on photonic technologies and electronic sources. As said in chapter 1, photonic THz emitters offer an advantage over electronics where a seamless connection with fiber optics is required. Most of the applications discussed previously are expected to be part of the converged optical wireless network concept introduced in section 1.3.2 and, thus, a seamless integration with the optical network will be required. The only applications which may not require an optical-THz interface are intra-chip communications and data centers. Also, in multi-hop networks, RAUs will not need to perform a conversion from the optical to the THz domain either. In these specific cases, the choice between electronics and photonics technologies will depend on how both technologies evolve in the coming years.

Nonetheless, the advantage of optical modulation enabled by photonics (see section 1.3.1.1) may tip the balance in favor of photonic sources even when an optical-THz interface is not required. This might be the case when, in order to maximize the data rate, simultaneous transmission at different THz windows would be advantageous. As noted in [18] this is more easily accomplished with photonics, where the channel multiplexing can be done in the optical domain (rather than in the THz domain).

2.2.2 THz receiver

On the (electronic) receiver, there are also two main options: coherent receivers based on mixers and non-coherent receivers based on envelope detectors (EDs). Among all the devices that can be used as EDs at THz frequencies, those that are interesting for high-speed wireless communications (i.e., those that have a short integration time) operate by generating a current or voltage that is proportional to

the incoming THz power. To do so, such devices must have a nonlinear current-voltage relationship. All the electronic devices mentioned in section 1.3.1.2 (i.e., SBDs, RTDs, and transistors) have such nonlinear characteristic and, hence, can be used as EDs. The same nonlinear characteristic is required for coherent receivers. In this case, however, the received signal is coupled with the output of a THz local oscillator (LO) that serves as the reference tone for the mixing process. The output of a coherent receiver is a voltage or current that is proportional to the incoming THz electric field.

While non-coherent receivers only accept intensity-modulated data and do not support phase or carrier multiplexing (unlike coherent receivers), they significantly simplify the system architecture since EDs do not require a THz LO. Hence, one may always opt for non-coherent receivers as long as the supported data rate is enough for the targeted application. In the following, we will try to determine, based on the data rates given in section 2.1.3, for which applications this might be the case. To simplify the discussion, we focus on the downlink only as its data rate requirements are normally higher than those of the uplink.

Since non-coherent receivers do not support frequency multiplexing¹, all the data would need to be transmitted on a single carrier. On applications with link distances higher than 10 m, where absorption peaks become non-negligible, this limits the total available bandwidth to that of a single transmission window. As shown in Figure 1.1, the wider transmission window, excluding windows V and VI (only suitable for near field transmissions), is the first one, with a total bandwidth of 68 GHz. Assuming double sideband (DSB) on-off keying (OOK) modulation, this bandwidth translates into a total data rate of 34 Gbit/s. This value is clearly not enough for any of the reviewed applications. Note that more complex non-coherent systems based on multiple-antenna receivers (see for instance [19]), can be used to extend the data rate. However, the complexity of such systems can be equal to or

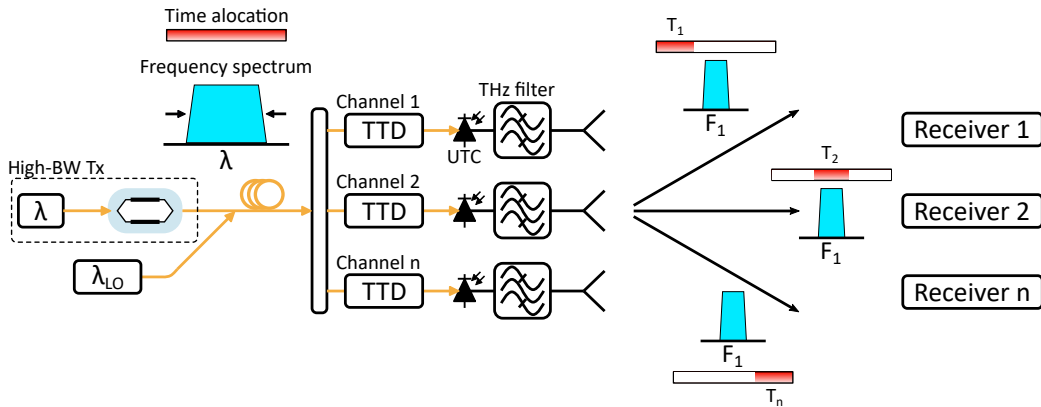
¹Frequency multiplexing can be used in non-coherent networks in order to address several receivers as long as these receivers have filters to select a determined frequency band. In this discussion, however, is assumed that the transmitter communicates only with a single receiver (this would be the case of backhaul links and wireless bridges for instance). In such a case the use of frequency multiplexing is not supported.

even higher than that of coherent systems supporting higher-order modulation, in which case no reason for their implementation may be found.

On the above discussion is assumed that all the data is to be transmitted to a single receiver. However in certain applications like fronthaul links or data centers the transmitter will need to communicate with several receivers located at different positions. To evaluate the feasibility of the non-coherent approach in these applications, one has to scale the capacity of a single link by the total number of links supported by the beam steering technique. As mentioned in section 2.1.1, there are two possible ways to distribute the data between several receivers: time-to-space beam steering (Fig. 2.4 (a)) and frequency-to-space beam steering (Fig. 2.4 (b)). With the latter approach, different frequency components of the THz beam are sent to different locations [8], where a non-coherent receiver may be used to down-convert the THz signal. In this case, hence, frequency multiplexing is permitted and the total available bandwidth would be the total bandwidth of all the atmospheric bands used by the application. Following what was discussed in section 1.2.2, fronthaul links may use windows I and II and data centers all the bands up to band IV, which gives aggregated bandwidths of 114 GHz and 234 GHz and data rates of 57 Gbit/s and 117 Gbit/s respectively. This is enough for data centers but still falls short in the case of fronthaul links. On the other hand, if a time multiplexing technique such as that of [7] is used to steer the THz beam, transmission will be performed at a single carrier frequency but the available bandwidth can be reused between the multiple receivers (the number of times being limited by several parameters such as number of antenna elements in the array, for example). In this case, sufficiently high data rates may be achieved with non-coherent receivers in fronthaul links as well.

Thus, according to an analysis based purely on system capacity, the use of non-coherent receivers and these techniques may be enough to meet the data rate requirements of single-transmitter-to-multiple-receiver applications. However, under practical considerations, the modulation bandwidth required at the transmitter, which will scale with the number of supported receivers, can severely limit the feasibility of the non-coherent approach. This is specially critical if time multi-

(a) Time multiplexing



(b) Frequency multiplexing

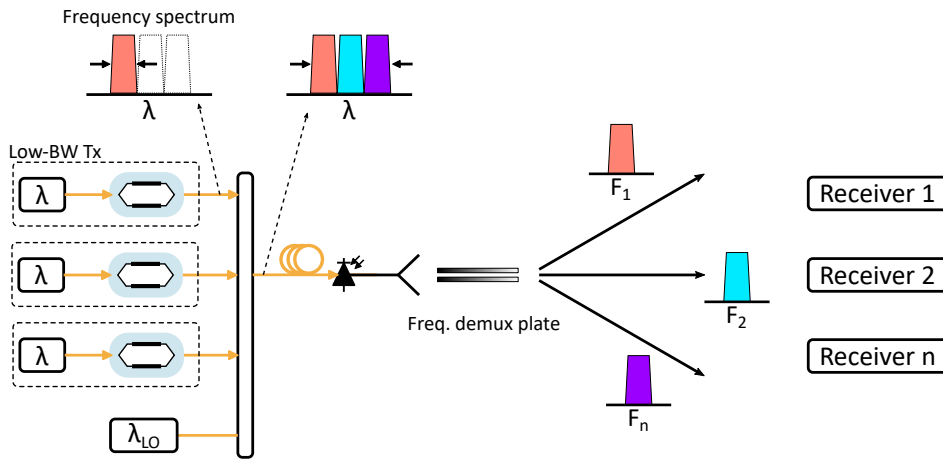


Figure 2.4: (a) Time-to-space beam steering concept (adapted from [7]) and (b) Time-to-space beam steering concept (adapted from [8]). TTD: true time delay

plexing is used to allocate the different receivers. In such case, all the data will have be encoded to the same carrier with a single modulator. As the total transmitter modulation bandwidth will be equal to the number of channels multiplied by the bandwidth of a single channel [7], the use of (low-spectral efficiency) intensity modulation imposed by envelope detectors may place a very stringent requirement on the modulator bandwidth. In reality, hence, complex modulation formats with phase multiplexing are likely to be necessary to decrease this requirement. As for the freq. demultiplexer approach, the bandwidth load can be shared between multiple low-capacity transmitters as shown in Fig. 2.4 (b). In this case the non-coherent

Table 2.1: Summary of THz applications

Application	Optical interface	Distance	Window	Rate (Gbit/s)	Modulation
Fixed links					
Backhauling	Yes	Few km	I	Several tens - 100	Higher order
Wireless bridges	Yes	Hundreds of m - few km	I&II	Few tens - 100	Higher order
Single-hop	Yes	1 km	I&II	Several tens	Higher order
Multi-hop	No	Hundreds of m	I&II	Several tens	Higher order
Data centers	Yes	10 m - 100 m	I,II,III&IV	Several tens	Higher order
Chip-to-chip	No	Few mm - few cm	all	Several tens	OOK
Links w/ active tracking					
Data kiosk	Yes	10 cm	all	Few tens	OOK
THz hotspot	Yes	10 m	I	Few tens	OOK

approach may be feasible.

In the case of near field applications such as data kiosks or chip-to-chip communications, where targeted distances are below 10 cm, atmospheric absorption peaks are negligible and a continuum of bandwidth will be available. In these cases, hence, bandwidth is not likely to be the main limitation. Furthermore, in both cases, the receiver will be in a portable device and, hence, a receiver based on an ED will be particularly convenient not only to simplify the system architecture but also minimize the energy consumption. In the case of THz hotspots, where the main emphasis will probably be on system simplicity and cost as well, a non-coherent receiver is also likely to be the preferred option. Beyond the reasoning of simpler receivers for simpler systems, it should be mentioned that, as noted in [20], coherent receivers can also be advantageous in the case of portable receivers due to their higher sensitivity. In fact, this increased sensitivity could pave the way to use lower gain antennas, which could be more easily integrated in such portable devices. In table 2.1, the main features and requirements of the envisaged THz applications are summarized. After going through all the applications, one can conclude that non-coherent receivers may only prevail in the cases where the receiver is in a portable device. On all other applications, however, complex modulation formats will be required to maximize the data, for which coherent detection will be required. In such case, the phase stability of the THz signal will affect the sensitivity of the system. Hence, to operate at an acceptable power level, mechanisms to reduce the phase

noise of the transmitted signal will be required. In the next section, some of the techniques that have been applied to THz communication systems to combat the phase noise are reviewed.

2.3 Phase noise reduction techniques

2.3.1 DSP

In a photonic THz system there are two types of impairments associated with the phase of the recovered signal: (a) frequency offset, which arises from the frequency difference between the signal and the LO used to down-convert the signal to baseband and translates into a linear phase variation with time and (b) phase noise, which arises mainly from the combined laser linewidths and can normally be modeled as a random walk distribution over time. Broadly, both the frequency offset estimation (FOE) and phase estimation (PE) algorithms that aim to correct these impairments operate by removing the modulation before estimating the frequency and phase deviations.

2.3.1.1 M^{th} power algorithms

The M^{th} power algorithms describe a class of nonlinear carrier recovery techniques for M -ary (where M is the modulation order) phase shift keying (PSK) modulated signals. By raising the digitized symbols to the M^{th} power, the modulation can be removed, allowing to estimate and eliminate both the frequency offset and phase noise of the incoming signal through different digital operations. If an M -PSK signal is modulated as follows:

$$s(t) = A \cos \left[2\pi f_c t + \frac{2\pi}{M} m \right], \quad m = 1, 2, \dots, M \quad (2.1)$$

where f_c is the carrier frequency and m is the PSK, then the equivalent digitized baseband signal can be represented as a complex number, z

$$z(k) = \exp^{j(2\pi\Delta f k T_s + \frac{2\pi}{M} m + \phi(k))} + n(k) \quad (2.2)$$

where $n(k)$ is the channel noise, Δf is the frequency offset, T_s is the symbol period, $\phi(k)$ is the phase noise and k is the sample number. By raising Z to the power M , the modulated component becomes $2\pi m$, which is always a multiple of 2π and, therefore, evaluates to unity in equation 2.2. Once the data has been removed, the FOE, $\hat{\Delta f}$, can be obtained through a fast Fourier transform (FFT) according to [21]:

$$\begin{aligned} X(K) &= \text{FFT}[z^M(k)] \\ X(K_0) &= \max[X(K)] \\ \hat{\Delta f} &= \frac{K_0}{NT_s M} \end{aligned} \quad (2.3)$$

where N is the number of samples used in the FFT.

After the frequency offset has been removed, the phase noise can be estimated by re-raising the samples to the M^{th} power a second time and then applying a block averaging filter [22]. This is done to eliminate the effect of additive white Gaussian noise (AWGN). Mathematically, this can be expressed as:

$$\hat{\phi}_{block} = \frac{1}{M} \left[\arg \left(\sum_{k=1}^N z^M(k) \right) \right], \quad (2.4)$$

where N is the size of the averaging filter. It is important to note, that, using the filter in 2.4, all samples within a block get the same phase error estimate. This PE algorithm for PSK signals is called the Viterbi-Viterbi (VV) algorithm.

2.3.1.2 QAM-adapted M^{th} power algorithms

The M^{th} power algorithms presented before can be adapted to square quadrature amplitude modulation (QAM) signals. In the case of FOE, the same procedure (see 2.3) can be used [21]. In the case of PE, before removing the data it is necessary to take amplitude decisions on the incoming samples (this requires equalization) so that only samples lying on constellation rings with QPSK phase distributions are selected [23]. For a unity power-normalized square 16-QAM signal this can be achieved with the following algorithm:

if $|x(k)| < 0.5(\sqrt{0.2} + 1)$ **or** $|x(k)| > 0.5(1 + \sqrt{1.8})$ **then**

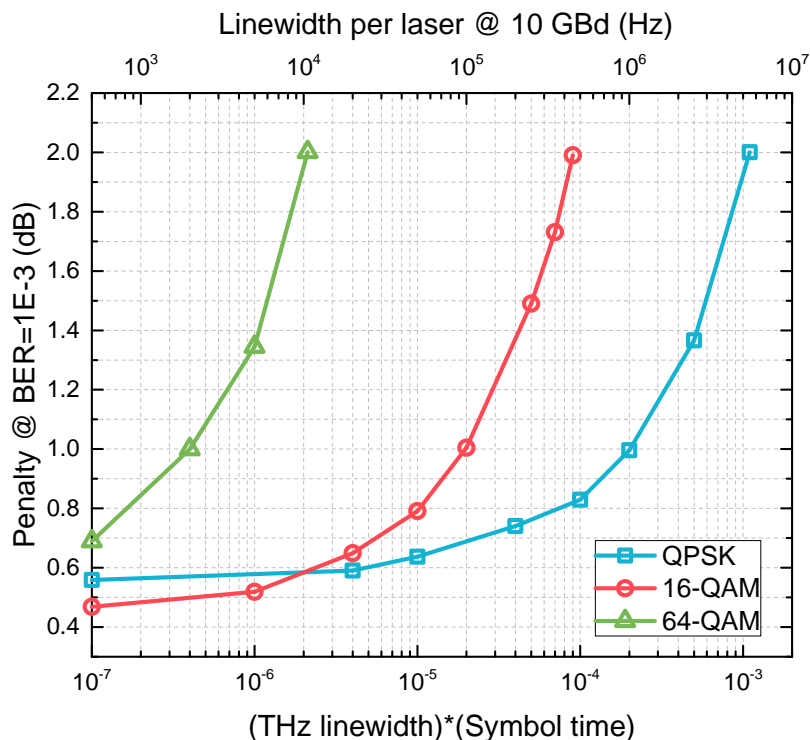


Figure 2.5: Sensitivity penalty of the QAM-adapted VV at a BER of 10^{-3} and an optimum block filter length N . The lower x axis shows the linewidth \times symbol product (figure of merit of PE algorithms [24]), while the upper x axis shows the required linewidth per laser (assuming two identical lasers) at a symbol rate of 10 GBd.

$$x(k) \leftarrow x_{class1}(k)$$

else

$$x(k) \leftarrow x_{class2}(k)$$

end if

where $x(k)$ is the output of the equalizer and x_{class1} are the samples with a QPSK phase distribution. After this, the selected samples are raised to the power of four and the estimate is calculated by averaging over a filter of length N according to:

$$\hat{\phi}_{block} = \frac{1}{4} \left[\arg \left(\sum_{k=1}^N \frac{x_{class1}^4(k)}{|x_{class1}^4(k)|} \right) \right]. \quad (2.5)$$

As can be seen from 2.5, before being summed, the complex samples have to be normalized to account for the fact that samples from different amplitude rings are used in the estimation. The sensitivity penalty of this algorithm (compared to the sensitivity of a system using differential decoding) is plotted in Figure 2.5.

2.3.1.3 Cycle slips and differential decoding

The $\arg(\cdot)$ function provides with a wrapped phase error estimate, however, the actual phase error extends from $+\infty$ to $-\infty$. Hence, to correctly track it, it is necessary to unwrap the output of the averaging filter. As the jump tolerance of the unwrapping operation is $\pm\pi$ and the phase error after the M th power operation is scaled by M , the estimate will be assigned a wrong quadrant number every time the phase error exhibits a jump higher than $\pm\frac{\pi}{M}$ between blocks. This is known as cycle slip and will cause all subsequent symbols to be misclassified until the receiver is reset [24].

Differential logical detection can be used to overcome cycle slips [24]. In this technique, data is encoded on the difference between the phase of two consecutive symbols rather than in the absolute phase of each symbol. At the receiver, this data is recovered by subtracting the phase of two consecutive received symbols. In doing so, the information received is dependent only on the phase of the currently detected and previously detected symbols and the propagation of errors through the symbol sequence is avoided.

An easy way to implement differential decoding in square-QAM constellations is by expressing the transmitted symbol as a function of the N differential angles determined by the N pairs of bits that are encoded in one symbol (i.e., $N = \log_2(M)/2$) [25]. For 16-QAM, for example, a symbol would be represented in terms of two differential angles $\{\Delta\theta_1, \Delta\theta_2\}$ and $\Delta\theta_1$ would be determined by the first two bits and $\Delta\theta_2$ by the last two bits. Expressing a 16-QAM symbol, a_k , as the summation of two vectors:

$$a_k = b_k + c_k, \quad (2.6)$$

then

$$b_k = 2/\sqrt{5} \cdot e^{j(\theta_{1,k-1} + \Delta\theta_{1,k})} \quad (2.7)$$

and

$$c_k = 1/\sqrt{5} \cdot e^{j(\theta_{2,k-1} + \Delta\theta_{2,k})} \quad (2.8)$$

where it is assumed that the signal has an average power of unity. This decomposi-

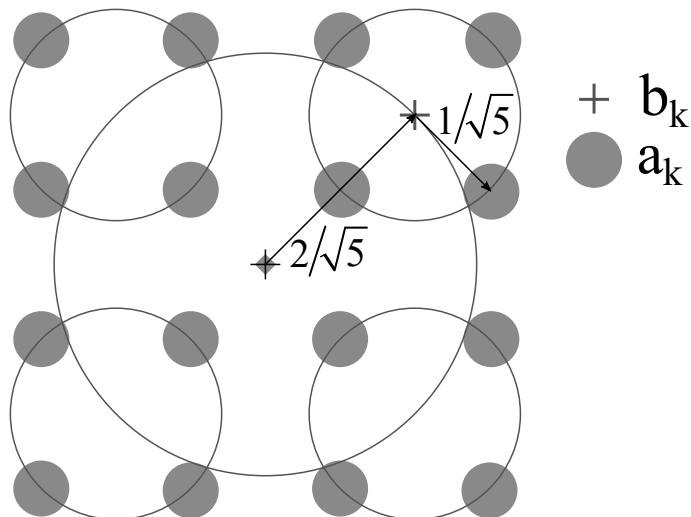


Figure 2.6: Differential decoding process

tion is shown in Figure 2.6. As can be seen, this method decomposes the M -QAM constellation to $\log_2(M)/2$ QPSK constellations.

Expressing the received signal as r_k , the differentially-encoded quadrant of the received symbol, \hat{b}_k , can be obtained as:

$$\hat{b}_k = 2/\sqrt{10}[\text{sign}(\Re\{r_k\}) + j\text{sign}(\Im\{r_k\})] \quad (2.9)$$

where \Re and \Im denote the real and imaginary components, respectively, and sign is the signum function. To obtain $\Delta\hat{\theta}_1$, one simply has to compute the phase difference between the quadrant vectors of two consecutive symbols (i.e. $\hat{b}_k \cdot \hat{b}_{k-1}^*$). After this, \hat{c}_k can be computed as follows:

$$\hat{c}_k = 1/\sqrt{10}[\text{sign}(\Re\{r_k - \hat{b}_k\}) + j\text{sign}(\Im\{r_k - \hat{b}_k\})] \quad (2.10)$$

where we have displaced the smaller QPSK constellation to the origin. $\hat{\theta}_2$ is then obtained by calculating $\hat{c}_k \cdot \hat{c}_{k-1}^*$.

2.3.1.4 Pilot tone-assisted carrier recovery

Another DSP technique that can be used for carrier recovery is the tone-assisted technique, where a pilot tone is added to the baseband signal and transmitted through the link [26]. At the digital receiver this tone is filtered out and then mixed

with the unfiltered signal to remove the frequency offset and phase noise. The pilot tone can be added to the baseband through the single sideband (SSB) with carrier modulation format, for example.

2.3.2 Optical frequency comb filtering

As we have seen in the previous section, although DSP can be used to mitigate the phase noise of free-running lasers, it can increase considerably the power consumption of the receiver and introduce some latency to the link. Furthermore, if using low-cost foundry-fabricated lasers (linewidths > 1 MHz [27]) or high-order modulation formats, they can incur in notably high penalties as seen in Figure 2.5. To avoid excessive digital complexity, two phase-correlated optical tones can be used for the beating process in the ultrafast PD.

The easiest way of creating two locked modes is modulating an optical continuous wave (CW) optical signal with an external modulator. In that case, two sidebands are generated at both sides of the optical carrier at a frequency distance equal to the driving signal frequency. This technique, however is not suitable for THz generation since it already requires an electrical signal at the desired frequency. To extend the frequency of an electrical signal in the optical domain the nonlinear transfer function of an external Mach-Zehnder modulator (MZM) can be exploited to create a carrier-suppressed modulation. The output signal consists now of two modes with a frequency separation equal to two times the driving frequency signal. For the THz regime, however, this technique still remains impractical given the frequency limitation of the available sources and the modulators.

A further increase in the frequency separation of two phase-locked modes, can be achieved by using several cascaded modulators [28] or a single dual-drive MZM driven by large-amplitude signals [29]. The output in this case, referred to as an optical frequency comb, is made of multiple optical wavelengths spanning over a wide optical wavelength range (comb span), all equidistant from each other by a fixed value (comb spacing), and all phase correlated to each other. The comb spacing is equal to the driving signal frequency. The subsystem used for creating such optical frequency comb (i.e. the CW laser, the modulator(s) and the RF LO)

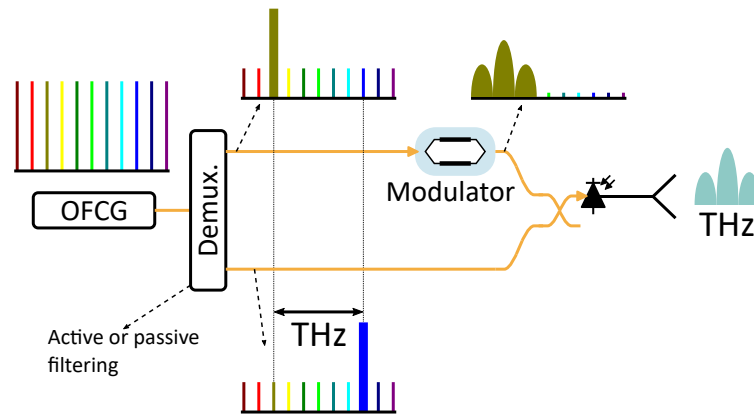


Figure 2.7: Photonic THz system with comb generation

is known as optical frequency comb generator (OFCG). When using an OFCG for coherent THz communications, two optical modes are filtered and sent to individual optical arms where one of them is modulated as seen in Figure 2.7.

For filtering two modes, passive filters may be used such as arrayed waveguide gratings (AWG) or ring-based filters. The problem with these filters is that their passband remains in the GHz-range level and their insertion loss is typically high (10 dB) [30]. If tight filtering is required and/or the peak power per comb line is low, a laser locking technique can be implemented instead to select the two OFCG modes. Injection locking, for instance, can be used for such a purpose [31]. However, the homodyne nature of this technique (i.e., the output of the slave laser can not be offset from that of the master) can limit the tunability of the THz signal if the line spacing of the OFCG cannot be quickly adjusted. To overcome all these problems, an optical phase-locked loop (OPLL) can be implemented instead.

An OPLL enables electronic control of the phase of an output of a laser source, locking the two wavelengths to a microwave reference electrical signal [32]. It is formed by a master and a slave laser, a PD, a phase detector (i.e., mixer), a low pass loop filter, and a microwave reference oscillator. The operation principle is based on comparing the signal generated by heterodyning the two lasers on the PD against that from the microwave reference. This process is done in the mixer, which is typically implemented as a double balanced mixer to minimize the unwanted direct current (DC) terms [33]. The error signal generated after proper filtering is fed back

to the phase section of the slave laser, forcing it into tracking the master laser at a frequency offset equal to the microwave reference frequency. To filter two OFCG modes, a dual arm OPLL—as that shown in Figure 2.8—can be used.

2.3.2.1 Phase noise in OFCGs-based systems

As shown in Figure 2.7, after selecting the two modes with the active/passive filter, one of them is passed through a modulator. Since both modes travel through different optical paths until they are recombined in the coupler, a time delay between the two optical modes will arise. This means that the phases of the two modes will not be totally correlated when they reach the ultra-fast PD causing a broadening in the THz signal linewidth. The degree of decorrelation depends on the coherence length—which is inversely proportional to the linewidth—of the laser driving the OFCG so that using a laser with a high coherence length—or a narrow linewidth—can mitigate the problem. Alternatively, if narrow-linewidth lasers are not economically viable, path-matching fibers can be used to effectively compensate the mismatch [34].

Apart from physical path mismatches, optical path fluctuations between the two optical paths can also arise due to temperature and acoustic noise in the optical fiber cables. These, as reported in [19], also compromise the phase of the generated signal. To mitigate this problem in reference [35], a method based on locking the two filtered modes (decorrelated) to the original unfiltered modes (correlated) of the OFCG is proposed. To do so a phase shifter (PS) in each arm is driven by the error

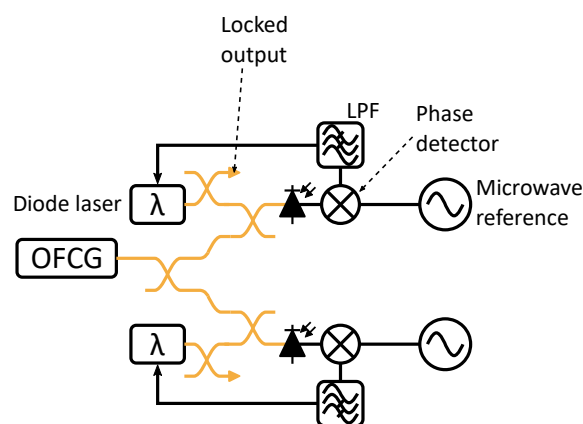


Figure 2.8: Dual-arm OPLL

signal resulting from photomixing the two filtered modes with the OFCG output. Since the photomixing process takes place in a low-speed PD, it only outputs the mixing products from modes oscillating at the same frequency. Multiple modes can be independently locked in a single PD by using dither signals as shown in Fig. 2.9. Another approach to decrease such time fluctuations is to integrate all the components in a single chip. This ensures better thermal tracking between the generated spectral line and can result in improved stability [36].

Even if the physical and the optical lengths mismatches between the two arms are well managed, the THz signal will exhibit the phase noise arising from the multiplication of the local oscillator signal driving the modulator in the OFCG. The resultant phase noise associated with this process is directly proportional to the number of times that the LO frequency has to be multiplied to achieved the proper frequency separation between modes [37]. For THz generation this multiplication factor can be quite high: for a LO frequency of 20 GHz and a target THz frequency of 300 GHz, the multiplication factor is 15. The contribution of this multiplication factor to the phase noise spectral density is given by $20 \times \log(N)$ (i.e., for $N = 15$, the phase noise spectral density will be scaled by 23.5 dB).

Furthermore, if the system is intended for RoF, the degree of correlation of the two modes reaching the PD will ultimately be limited by chromatic dispersion. This would have an effect similar to a path mismatch between the two transmitted modes [38]. Although these effects may not be critical if low-noise optical and electrical

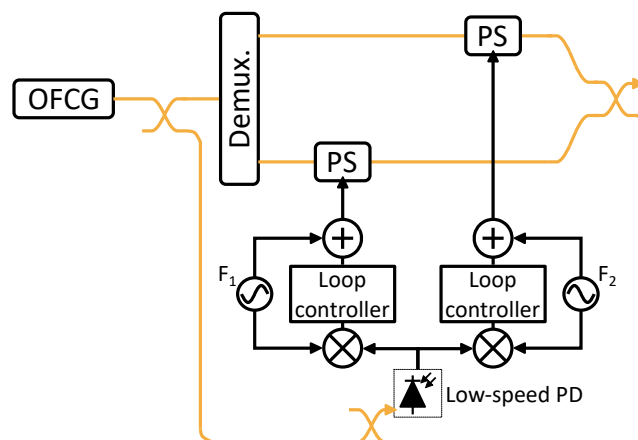


Figure 2.9: Stabilization of two OFCG's filter modes with PSs. Adapted from [35].

Table 2.2: Notable THz transmissions with OFCGs

Data rate (Gbit/s)	Frequency	Multiplexing	Modulation	Carrier recovery DSP	Reference
20	325 GHz	-	QPSK	Yes	[15]
100	200 GHz	Frequency	QPSK	Yes (only PE)	[39]
100	237.5 GHz	Frequency	16- & 8-QAM	Yes	[40]
106	400 GHz	-	16-QAM	Yes	[41]
100	320 GHz	-	QPSK	No	[42]

sources are available, they may become limiting factors if cost-efficient sources are required and higher-order modulation formats like 16-QAM are needed. For all these reasons, most of the systems employing OFCGs for THz generation have also used DSP compensation in the receiver. In table 2.2, notable THz communication experiments using OFCG are shown.

2.3.3 Envelope detector-based systems

Direct detection of THz with an envelope detector can be used to eliminate the penalty due to phase noise. To enable the use of QAM or PSK with an envelope detector, the complex baseband signal must be up-converted to an RF [43]. This signal plus a DC term are then modulated to an optical carrier to produce an intensity modulated (IM) signal with a double sideband-with carrier (DSB+C) spectrum. This signal is then combined with another optical tone at the proper frequency separation and sent to a high-speed PD to produce a DSB+C THz signal. The problem with this technique is that the optical DSB+C signal has low spectral efficiency and is sensitive to power fading due to chromatic dispersion. To solve these problems one of the redundant sidebands can be suppressed by using the SSB modulation format [44].

One of the ways to achieve a SSB signal is via the Hilbert transform (HT) [45]. The HT is a mathematical operator in which all negative frequency components of a signal are phase advanced by 90° whereas all positive frequency components are phase-delayed by 90° (i.e. it introduces a 180° phase difference between the negative and positive components of the input signal). The amplitude of the spectrum remains unchanged. The frequency response of a HT, $G_{HT}(\omega)$, can be therefore

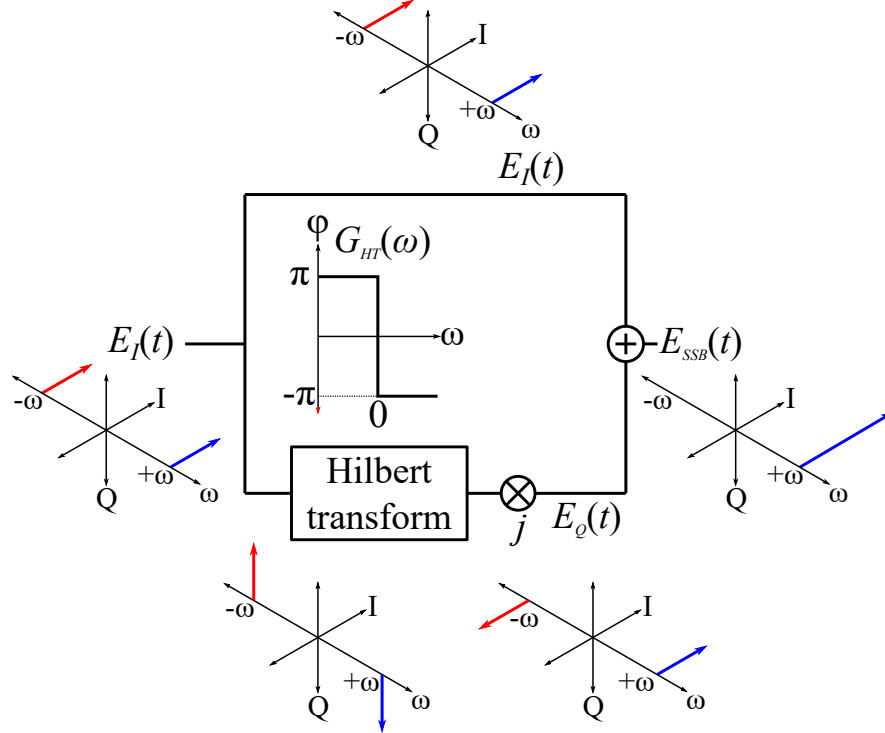


Figure 2.10: SSB signal generation using Hilbert transform

expressed as:

$$G_{HT}(\omega) = \begin{cases} e^{-j\pi/2}, & \text{if } \omega > 0 \\ 0, & \text{if } \omega = 0 \\ e^{j\pi/2}, & \text{if } \omega < 0 \end{cases} \quad (2.11)$$

where ω denotes the angular frequency. The HT can be implemented in the analog domain with a 90° phase shifter or in the digital domain with frequency- (exact response function) or time-based (approximate response function) filters.

To generate an optical SSB signal, a setup like that shown in Figure 2.10 is required. The RF up-converted signal is first split into two paths. In one of them the signal is passed through a block implementing the HT operator whereas in the other the signal remains unchanged. Both outputs are then used as the driving signals of an optical IQ-modulator. Analytically, if we express the up-converted signal as:

$$\begin{aligned} b(t) &= A_{mod}(t) \cos(\omega_{RF}t + \theta_{mod}(t)) \\ &= \frac{A_{mod}(t)}{2} [e^{j(\omega_{RF}t + \theta_{mod}(t))} + e^{-j(\omega_{RF}t + \theta_{mod}(t))}], \end{aligned} \quad (2.12)$$

where ω_{RF} is the up-conversion frequency, then its HT $\hat{b}(t)$ is:

$$\begin{aligned}\hat{b}(t) &= \mathbf{H}[b(t)] = A_{mod}(t) \sin(\omega_{RF}t + \theta_{mod}(t)) \\ &= \frac{jA_{mod}(t)}{2} [-e^{j(\omega_{RF}t + \theta_{mod}(t))} + e^{-j(\omega_{RF}t + \theta_{mod}(t))}],\end{aligned}\quad (2.13)$$

where $\mathbf{H}[\bullet]$ denotes the HT. By writing the output of the CO laser as $E_S(t) = A_S e^{j(\omega_S t + \varphi_S(t))}$, where $\varphi_S(t)$ denotes the phase noise of the laser, and assuming a sufficiently small modulation index, the IQ-modulator linearly maps $b(t)$ and $\hat{b}(t)$ to the optical domain, so that the output electric field can be expressed as:

$$\begin{aligned}E_{out}(t) &\propto E_S(t) \cdot [(V_I + b(t)) + j(V_Q + \hat{b}(t))] \\ &\propto A_C e^{j(\omega_S t + \theta_{bias} + \varphi_S(t))} + A_{mod}(t) e^{j((\omega_S + \omega_{RF})t + \theta_{mod}(t) + \varphi_S(t))},\end{aligned}\quad (2.14)$$

where V_I and V_Q are the biasing points of the I- and Q-components respectively,

$$\theta_{bias} = \arctan(V_Q/V_I), \quad (2.15)$$

and

$$A_C = \sqrt{V_I^2 + V_Q^2}. \quad (2.16)$$

As can be seen from 2.14, the output of the IQ-modulator is a SSB signal with the optical carrier (first term) and the upper sideband (second term). As shown in Figure 2.11, for THz generation, this signal is then combined with another optical tone, which may be written as $E_{LO}(t) = A_{LO} e^{j(\omega_{LO} t + \varphi_{LO}(t))}$, where $\varphi_{LO}(t)$ denotes the phase noise of the laser. The combined signal is then sent to a PD, where a current oscillating at a frequency equal to the frequency difference between the two lasers (here assumed to be in the range of THz) is generated according to:

$$\begin{aligned}E_{THz}(t) &\propto E_{out}(t) \cdot (jE_{LO}(t))^* \\ &\propto A_C e^{j(\omega_{THz} t + \theta_{bias} + \Delta\varphi(t))} + A_{mod}(t) e^{j((\omega_{THz} + \omega_{RF})t + \theta_{mod}(t) + \Delta\varphi(t))},\end{aligned}\quad (2.17)$$

where $\omega_{THz} = |\omega_S - \omega_{LO}|$, and $\Delta\varphi(t) = \varphi_S(t) - \varphi_{LO}(t) - 90^\circ$ represents the phase noise of the THz signal and includes the 90° degree phase shift introduced by the

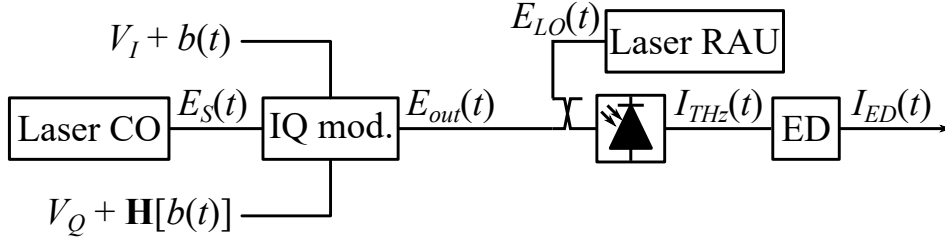


Figure 2.11: Photonic generation and envelope detection of THz SSB signals

3-dB coupler.

Finally, modeling the THz ED as a square-law device where the output is low pass filtered, the final signal can be expressed as:

$$\begin{aligned}
 I_{ED}(t) &\propto E_{THz}(t) \cdot E_{THz}^*(t) \\
 &\propto A_C^2 + A_{mod}^2(t) + 2RA_{mod}(t) \cos(\omega_{RF}t + \theta_{mod}(t) - \theta_{bias}),
 \end{aligned} \tag{2.18}$$

From 2.18 it is easy to see that the recovered signal does not include the combined phase noise contribution of the two lasers $\Delta\phi(t)$ since it vanishes when the unmodulated tone beats with the sideband in the ED. On the other hand, it does contain the phase term introduced by the biasing points of the I- and Q-components in the optical modulator θ_{bias} . Although this only causes a fixed phase rotation of the received signal (i.e. it does not vary with time), it needs to be removed during the demodulation process. From 2.18, one can also see that the detected signal, apart from the useful signal, includes a DC component (first term) and a term which is the beating of the signal with itself (second term). This term spans from DC up to the signal bandwidth and as we shall see later can interfere with the useful signal if no counter techniques are used.

Bibliography

- [1] IEEE 802.15 TG 3d. IEEE 802.15 WPAN Task Group 3d 100 Gbit/s Wireless (TG 3d (100G)). URL http://www.ieee802.org/15/pub/index_TG3d.html.
- [2] IEEE 802.15 TG 3d. Technical Requirements. Technical report, IEEE, 2008.
- [3] IEEE 802.15 TG 3d. THz-Phy. Technical report, IEEE, 2016.
- [4] IEEE 802.15 TG 3d. Applications requirements. Technical report, IEEE, 2015.
- [5] IEEE 802.15 TG 3d. Technical expectations. Technical report, IEEE, 2014.
- [6] ITU-R. Technology trends of active services in the frequency range 275-3 000 GHz SM Series. Technical report, 2015.
- [7] Romain Bonjour, Samuel Welschen, and Juerg Leuthold. Time-to-space division multiplexing for Tb/s mobile cells. *IEEE Transactions on Wireless Communications*, 17(7):4806–4818, 2018. ISSN 15361276. doi: 10.1109/TWC.2018.2832046.
- [8] Jianjun Ma, Nicholas J. Karl, Sara Bretin, Guillaume Ducournau, and Daniel M. Mittleman. Frequency-division multiplexer and demultiplexer for terahertz wireless links. *Nature Communications*, 8(1):1–7, 2017. ISSN 20411723. doi: 10.1038/s41467-017-00877-x. URL <http://dx.doi.org/10.1038/s41467-017-00877-x>.
- [9] Thomas Kürner, Ingmar Kallfass, Katsuhiro Ajito, Akifumi Kasamatsu, David Britz, and Sebastian Priebe. Whats next? Wireless Communication beyond 60 GHz Tutorial, 2012.
- [10] Atsushi Kanno, Pham Tien Dat, Toshiaki Kuri, Iwao Hosako, Tetsuya Kawanishi, Yuki Yoshida, and Ken-ichi Kitayama. Waveform over fiber: DSP-aided coherent fiber-wireless transmission using millimeter and terahertz waves. 9387:93870C, 2015. ISSN 1996756X. doi: 10.1117/12.2077056. URL <http://proceedings.spiedigitallibrary.org/proceeding.aspx?doi=10.1117/12.2077056>.
- [11] Alan Davy, Luis Pessoa, Cyril Renaud, Edward Wasige, Mira Naftaly, Thomas Kurner, Glenn George, Oleg Cojocari, Niamh O. Mahony, and Marco A.G. Porcel. Building an end user focused THz based ultra high bandwidth wireless access network: The TERAPOD approach. *International Congress on Ultra Modern Telecommunications and Control Systems and Workshops*, 2017-Novem:454–459, 2018. ISSN 2157023X. doi: 10.1109/ICUMT.2017.8255205.
- [12] Thomas Kürner and Sebastian Priebe. Towards THz communications - Status in research, standardization and regulation. *Journal of Infrared, Millimeter, and Terahertz Waves*, 35(1):53–62, 2014. ISSN 18666906. doi: 10.1007/s10762-013-0014-3.
- [13] V. Petrov, A. Pyattaev, D. Moltchanov, and Y. Koucheryavy. Terahertz band communications: Applications, research challenges, and standardization activities. *International Congress on Ultra Modern Telecommunications and Control Systems and Workshops*, 2016-Decem:183–190, 2016. ISSN 2157023X. doi: 10.1109/ICUMT.

- 2016.7765354.
- [14] Tadao Nagatsuma, Kazuki Oogimoto, Yuki Inubushi, and Jiro Hirokawa. Practical considerations of terahertz communications for short distance applications. *Nano Communication Networks*, 10:1–12, 2016. ISSN 18787789. doi: 10.1016/j.nancom.2016.07.005. URL <http://dx.doi.org/10.1016/j.nancom.2016.07.005>.
- [15] Atsushi Kanno, Toshiaki Kuri, Isao Morohashi, Iwao Hosako, Tetsuya Kawanishi, Yuki Yoshida, and Ken ichi Kitayama. Coherent Terahertz Wireless Signal Transmission Using Advanced Optical Fiber Communication Technology. *Journal of Infrared, Millimeter, and Terahertz Waves*, 36(2):180–197, 2015. ISSN 18666906. doi: 10.1007/s10762-014-0132-6.
- [16] Afif Osseiran, Federico Boccardi, Volker Braun, Katsutoshi Kusume, Patrick Marsch, Michal Maternia, Olav Queseth, Malte Schellmann, Hans Schotten, Hidekazu Taoka, Hugo Tullberg, Mikko A. Uusitalo, Bogdan Timus, and Mikael Fallgren. Scenarios for 5G mobile and wireless communications: The vision of the METIS project. *IEEE Communications Magazine*, 52(5):26–35, 2014. ISSN 01636804. doi: 10.1109/MCOM.2014.6815890.
- [17] Sebastian Priebe, David M. Britz, Martin Jacob, Stephen Sarkozy, Kevin M.K.H. Leong, Jennifer E. Logan, Ben S. Gorospe, and Thomas Kürner. Interference investigations of active communications and passive earth exploration services in the THz frequency range. *IEEE Transactions on Terahertz Science and Technology*, 2(5):525–537, 2012. ISSN 2156342X. doi: 10.1109/TTHZ.2012.2208191.
- [18] Tadao Nagatsuma, Guillaume Ducournau, and Cyril C. Renaud. Advances in terahertz communications accelerated by photonics. *Nature Photonics*, 10(6):371–379, 2016. ISSN 17494893. doi: 10.1038/nphoton.2016.65. URL <http://dx.doi.org/10.1038/nphoton.2016.65>.
- [19] Tadao Nagatsuma, Shogo Horiguchi, Yusuke Minamikata, Yasuyuki Yoshimizu, Shintaro Hisatake, Shigeru Kuwano, Naoto Yoshimoto, Jun Terada, and Hiroyuki Takahashi. Terahertz wireless communications based on photonics technologies. *Optics Express*, 21(20):23736, 2013. ISSN 1094-4087. doi: 10.1364/OE.21.023736. URL <https://www.osapublishing.org/oe/abstract.cfm?uri=oe-21-20-23736>.
- [20] Guillaume Ducournau, Pascal Szriftgiser, Fabio Pavanello, Emilien Peytavit, Mohammed Zaknour, Denis Bacquet, Alexandre Beck, Tahsin Akalin, Jean Francois Lampin, and Jean Francois Lampin. THz Communications using Photonics and Electronic Devices: the Race to Data-Rate. *Journal of Infrared, Millimeter, and Terahertz Waves*, 36(2):198–220, 2015. ISSN 18666906. doi: 10.1007/s10762-014-0112-x.
- [21] M. Selmi, Y. Jaouen, and P. Ciblat. Accurate digital frequency offset estimator for coherent PolMux QAM transmission systems. *2009 35th European Conference on Optical Communication*, (1):3–4, 2009. ISSN 1550-381X. doi: 10.1109/LPT.2013.2241050.
- [22] Andrew J. Viterbi and Audrey M. Viterbi. Nonlinear Estimation of PSK-Modulated Carrier Phase with Application to Burst Digital Transmission. *IEEE Transactions on Information Theory*, 29(4):543–551, 1983. ISSN 15579654. doi: 10.1109/TIT.1983.1056713.
- [23] Matthias Seimetz. Laser linewidth limitations for optical systems with high-order modulation employing feed forward digital carrier phase estimation. *OFC/NFOEC 2008 - 2008 Conference on Optical Fiber Communication/National Fiber Optic Engi-*

- neers Conference*, pages 2–4, 2008. doi: 10.1109/OFC.2008.4528637.
- [24] Michael G. Taylor. Phase estimation methods for optical coherent detection using digital signal processing. *Journal of Lightwave Technology*, 27(7):901–914, 2009. ISSN 07338724. doi: 10.1109/JLT.2008.927778.
- [25] Irshaad Fatadin, David Ives, and Seb J. Savory. Compensation of frequency offset for differentially encoded 16- and 64-QAM in the presence of laser phase noise. *IEEE Photonics Technology Letters*, 22(3):176–178, 2010. ISSN 10411135. doi: 10.1109/LPT.2009.2037329.
- [26] Sebastian Randel, Susmita Adhikari, and Sander L. Jansen. Analysis of RF-pilot-based phase noise compensation for coherent optical OFDM systems. *IEEE Photonics Technology Letters*, 22(17):1288–1290, 2010. ISSN 10411135. doi: 10.1109/LPT.2010.2053528.
- [27] Mu-Chieh Lo, Alberto Zarzuelo, Robinson Guzman, and Guillermo Carpintero. Monolithically Integrated Microwave Frequency Synthesizer on InP Generic Foundry Platform. *Journal of Lightwave Technology*, 36(19):4626–4632, 2018. ISSN 0733-8724. doi: 10.1109/JLT.2018.2836298. URL <https://ieeexplore.ieee.org/document/8358771/>.
- [28] Tadao NAGATSUMA and Guillermo CARPINTERO. Recent Progress and Future Prospect of Photonics-Enabled Terahertz Communications Research. *IEICE Transactions on Electronics*, E98.C(12):1060–1070, 2015. ISSN 0916-8524. doi: 10.1587/transele.E98.C.1060. URL https://www.jstage.jst.go.jp/article/transele/E98.C/12/E98.C_1060/_article.
- [29] T. Sakamoto, T. Kawanishi, and M. Izutsu. Widely wavelength-tunable ultra-flat frequency comb generation using conventional dual-drive Mach-Zehnder modulator. *ELECTRONICS LETTERS*, 43(19), 2007. ISSN 00309982. doi: 10.1049/el.
- [30] K. Balakier, H. Shams, M. J. Fice, L. Ponnampalam, C. S. Graham, C. C. Renaud, and A. J. Seeds. Photonic integrated circuit optical phase lock loop tuneable active filter. *2017 IEEE Photonics Conference (IPC) Part II*, pages 1–2, 2018. doi: 10.1109/PC.2017.8283409.
- [31] Katarzyna Balakier, Martyn J. Fice, Frederic van Dijk, Gael Kervella, Guillermo Carpintero, Alwyn J. Seeds, and Cyril C. Renaud. Optical injection locking of monolithically integrated photonic source for generation of high purity signals above 100 GHz. *Optics Express*, 22(24):29404, 2014. ISSN 1094-4087. doi: 10.1364/OE.22.029404. URL <https://www.osapublishing.org/oe/abstract.cfm?uri=oe-22-24-29404>.
- [32] Katarzyna Balakier, Martyn J. Fice, Lalitha Ponnampalam, Chris S. Graham, Adrian Wonfor, Alwyn J. Seeds, and Cyril C. Renaud. Foundry fabricated photonic integrated circuit optical phase lock loop. *Optics Express*, 25(15):16888–16897, 2017. ISSN 1094-4087. doi: 10.1364/OE.25.016888. URL <https://www.osapublishing.org/abstract.cfm?URI=oe-25-15-16888>.
- [33] Stephan R Kurtz. Mixers as Phase Detectors (Watkins-Johnson Company Tech. Notes). *The Communications Edge*, 5, 1978. URL www.wj.com.
- [34] Tong Shao, Haymen Shams, Prince M. Anandarajah, Martyn J. Fice, Cyril C. Renaud, Frederic Van Dijk, Alwyn J. Seeds, and Liam P. Barry. Phase Noise Investigation of multicarrier Sub-THz Wireless Transmission System Based on an Injection-Locked Gain-Switched Laser. *IEEE Transactions on Terahertz Science and Technology*, 5(4): 590–597, 2015. ISSN 2156342X. doi: 10.1109/TTHZ.2015.2418996.
- [35] Yasuyuki Yoshimizu, Shintaro Hisatake, Shigeru Kuwano, Jun Terada, Naoto Yoshi-

- moto, and Tadao Nagatsuma. Generation of coherent sub-terahertz carrier with phase stabilization for wireless communications. *Journal of Communications and Networks*, 15(6):569–575, 2013. ISSN 12292370. doi: 10.1109/JCN.2013.000105.
- [36] Guillermo Carpintero, Efthymios Rouvalis, Katarzyna Ławniczuk, Martyn Fice, Cyril C. Renaud, Xaveer J. M. Leijts, Erwin A. J. M. Bente, Mourad Chitoui, Frederic Van Dijk, and Alwyn J. Seeds. 95GHz millimeter wave signal generation using an arrayed waveguide grating dual wavelength semiconductor laser. *Optics Letters*, 37(17):3657, 2012. ISSN 0146-9592. doi: 10.1364/OL.37.003657. URL <https://www.osapublishing.org/abstract.cfm?URI=ol-37-17-3657>.
- [37] Lalitha Ponnampalam, Martyn Fice, Haymen Shams, Cyril Renaud, and Alwyn Seeds. Optical comb for generation of a continuously tunable coherent THz signal from 1225GHz to >27THz. *Optics Letters*, 43(11):2507, 2018. ISSN 0146-9592. doi: 10.1364/OL.43.002507. URL <https://www.osapublishing.org/abstract.cfm?URI=ol-43-11-2507>.
- [38] Rolf Hofstetter, Harald Schmuck, and Rolf Heidemann. Dispersion Effects in Optical Millimeter-Wave Systems Using Self-Heterodyne Method for Transport and Generation. *IEEE Transactions on Microwave Theory and Techniques*, 43(9):2263–2269, 1995. ISSN 15579670. doi: 10.1109/22.414574.
- [39] H. Shams, T. Shao, M. J. Fice, P. M. Anandarajah, C. C. Renaud, F. Van Dijk, Liam P. Barry, and Alwyn J. Seeds. 100 Gb/s multicarrier THz wireless transmission system with high frequency stability based on a gain-switched laser comb source. *IEEE Photonics Journal*, 7(3), 2015. ISSN 19430655. doi: 10.1109/JPHOT.2015.2438437.
- [40] S. Koenig, D. Lopez-Diaz, J. Antes, F. Boes, R. Henneberger, A. Leuther, A. Tessmann, R. Schmogrow, D. Hillerkuss, R. Palmer, T. Zwick, C. Koos, W. Freude, O. Ambacher, J. Leuthold, and I. Kallfass. Wireless sub-THz communication system with high data rate. *Nature Photonics*, 7(12):977–981, 2013. ISSN 17494885. doi: 10.1038/nphoton.2013.275.
- [41] Shi Jia, Xiaodan Pang, Oskars Ozolins, Xianbin Yu, Hao Hu, Jinlong Yu, Pengyu Guan, Francesco Da Ros, Sergei Popov, Gunnar Jacobsen, Michael Galili, Toshio Morioka, Darko Zibar, and Leif K. Oxenlowe. 0.4 THz Photonic-Wireless Link with 106 Gb/s Single Channel Bitrate. *Journal of Lightwave Technology*, 36(2):610–616, 2018. ISSN 07338724. doi: 10.1109/JLT.2017.2776320.
- [42] Tadao Nagatsuma, Yusuke Fujita, Yu Yasuda, Yusuke Kanai, Shintaro Hisatake, Masamichi Fujiwara, and Junichi Kani. Real-time 100-Gbit / s QPSK Transmission Using. In *International Topical Meeting on Microwave Photonics (MWP)*, volume 1, pages 27–30, 2016. ISBN 9781509016020.
- [43] Maria Freire Hermelo, Po-Tsung (Boris) Shih, Matthias Steeg, Anthony Ngoma, and Andreas Stöhr. Spectral efficient 64-QAM-OFDM terahertz communication link. *Optics Express*, 25(16):19360, 2017. ISSN 1094-4087. doi: 10.1364/OE.25.019360. URL <https://www.osapublishing.org/abstract.cfm?URI=oe-25-16-19360>.
- [44] Christina Lim, Ampalavanapillai Nirmalathas, Masuduzzaman Bakaul, Prasanna Gamage, Ka Lun Lee, Yizhuo Yang, Dalma Novak, and Rod Waterhouse. Fiber-wireless networks and subsystem technologies. *Journal of Lightwave Technology*, 28(4):390–405, 2010. ISSN 07338724. doi: 10.1109/JLT.2009.2031423.
- [45] Spiros Mikroulis, Manoj P. Thakur, and John E. Mitchell. Evaluation of OOK and OFDM on an SMF-MMF-SMF Link Targeting a PON/60-GHz Topology for beyond 4G. *IEEE Photonics Technology Letters*, 28(4):449–452, 2016. ISSN 10411135. doi:

10.1109/LPT.2015.2499159.

Chapter 3

Envelope detector-based THz systems

THz systems based on EDs have several advantages. On the one hand, they substantially simplify the receiver as no LO is needed. On the other hand, as shown in Equation 2.18, these systems are robust against phase noise, which enables the use of free-running lasers. This, in turn, brings another set of advantages. The most obvious one is the complexity and cost reduction associated with these type of lasers, as opposed to systems based on OFCGs and narrow-band filters. Crucially this also allows placing one of the lasers on the RAU. This arrangement, apart from freeing CO channels, thereby increasing the bandwidth efficiency and facilitating the integration with PONs, it also increases the energy efficiency as the laser in the RAU does not get attenuated by the optical fiber connecting the CO and RAU. On the other hand, these benefits could be tainted by the fact that placing a laser on the RAU would increase the cost of such unit [1]. However, if the link is to support full-duplex operation, then the RAU will need to have an optical source anyway (for the uplink data). Although laser-free RAUs have been proposed, they require complex filtering schemes [2]. By reusing the free-running laser at the RAU for the uplink and the downlink, the system can be greatly simplified, obtaining units very similar to what is currently being proposed for future optical networks ONUs [3].

In this chapter, THz system architectures based on envelope detection and high-order modulation formats are investigated. In section 3.1, the DSP used for generation and detection of SSB signals is presented, briefly explaining the main algorithms used in this work. Then, in the second part of section 3.1, the experi-

mental arrangement used throughout this chapter is outlined. In section 3.2, important parameters of SSB signals, like the signal-signal beat interference (SSBI) or the carrier-to-sideband power ratio (CSPR) are discussed. The phase noise robustness of SSB signals is then experimentally tested by means of linewidth emulation [4]. In the last part of section 3.2, the bandwidth-efficiency gain of a SSBI-cancellation algorithm known as Kramers-Kronig (KK) is studied. After this, the linewidth tolerance of a system based on baseband signals (throughout this thesis we refer to THz QAM signals as baseband signals to distinguish them from the IM SSB signals) and carrier recovery is tested and compared to that achieved with SSB signals and ED.

In section 3.3, two techniques for SSB signal generation that lower the analog bandwidth requirements of the digital-to-analog converter (DAC) in the transmitter, are presented, highlighting the main features of each technique. Following this, simulation results are provided comparing the quality of the sideband signal generated by each technique. In the last part of section 3.3, end-to-end implementation of a THz system incorporating each of these techniques is performed. Finally, the obtained BER results for each technique, including those obtained with the conventional SSB generation technique through the HT, are analyzed and compared.

3.1 Tx and Rx DSP and experimental arrangement

3.1.1 DSP for SSB generation and reception

Due to the phase robustness of envelope-detected signals, no FOE or PE algorithms are required in their demodulation process. Next, the main DSP blocks used in this work for systems based on ED are briefly described and explained as well as the complete DSP chain used both at the transmitter and receiver.

3.1.1.1 Root raised cosine filters

Root raised cosine (RRC) filters are used throughout this thesis for pulse shaping purposes. The frequency response of such filters is derived from that of the raised cosine filter, whose time characteristics satisfy the Nyquist intersymbol interference (ISI) condition, while having a band-limited spectrum in the frequency domain. To take advantage of matched filtering, the pulse shaping load of the raised cosine

can be implemented as the product of two identical responses. In such cases, the response becomes a square-root raised cosine. The frequency response of such filters is given as:

$$H(\omega) = \begin{cases} \sqrt{T_s}, & \text{if } 0 \leq \omega \leq c \\ \sqrt{T_s} \left(\cos \left[\frac{T_s(\omega-c)}{4\alpha} \right] \right), & \text{if } c \leq \omega \leq d \\ 0, & \text{if } \omega > d \end{cases} \quad (3.1)$$

where ω is the radian frequency, T_s denotes the symbol period, $c = \frac{\pi(1-\alpha)}{T_s}$ and $d = \frac{\pi(1+\alpha)}{T_s}$. As can be seen from this, the stop band frequency (f_{stop}), defined as the frequency at which the response first reaches zero magnitude, is related to α by $f_{stop} = (1 - \alpha) \frac{R_s}{2}$, where R_s is the symbol rate. While low values of α increase the spectral efficiency of a system, they also lead to higher peak to average power ratios and can increase the likelihood of ISI. Thus the specific election of α is a trade-off between these features.

3.1.1.2 Equalization

Adaptive equalization is used in this thesis for two purposes: for symbol re-timing (i.e., to get the ideal sampling phase) and to approximate the inverse channel response. The equalizers used here are blind (do not require training sequences for their initialization) and adaptive. Such filters adapt their tap weights after each iteration based on the output of an error function. This error function is a measure of the deviation from the property that equalizer aims to restore, which is determined a priori based on the knowledge of the modulation format.

Two different equalizers are used throughout this thesis: the radius directed equalizer (RDE) and the decision-directed (DD) equalizer. The RDE has the following error function:

$$e(k) = y(k)(R_y - |y(k)|^2), \quad (3.2)$$

where $y(k)$ is the equalized output and R_y is the radius of the nearest constellation symbol for each equalizer output. To determine (R_y), amplitude decision need to be taken on the equalizer output. For 16-QAM the algorithm in section 2.3.1.2 can be

used. On the other hand, the error function of the DD equalizer is defined as:

$$e(k) = \hat{a}(k) - y(k) \quad (3.3)$$

where $\hat{a}(k)$ is the decision value using a standard rectilinear grid of decision regions in the constellation (hard decision). The convergence of this algorithm, thus, depends on making a series of successive correct decisions for symbols. For this reason, this equalizer is used at the final stage of the receiver DSP routine and often in conjunction with other equalizers.

After the error function has been calculated, the tap weights of the two equalizers are updated with the least mean squares (LMS) algorithm according to

$$w(k+1) = w(k) + \mu \cdot x(k) \cdot e^*(k) \quad (3.4)$$

where $w(k)$ are the tap weights, μ is the step size parameter of the LMS algorithm and $x(k)$ is the equalizer input.

3.1.1.3 Complete transmitter and receiver DSP routine

The DSP blocks used to generate the SSB signal waveform are shown in Figure 3.1. Four 2^{11} De Bruijn bit sequences decorrelated by approximately 25% of the pattern length were used for symbol generation. The length of the De Bruijn sequence is an important parameter as a short sequence can inaccurately predict the impact of ISI. Assuming the main source of ISI in our system comes from chromatic dispersion (CD), then the minimum required order of the symbol sequence is given by [5] :

$$n_s = D_{max} \frac{c}{f_s^2} B_s r_s + 1 \quad (3.5)$$

where n_s is the symbol order, r_s the symbol rate, D_{max} is the accumulated chromatic dispersion, f_s the optical carrier frequency and B_s the signal bandwidth. From all the transmission experiments carried throughout this thesis, the maximum length of optical fiber was 50 km, which (at an optical carrier frequency of 193.1 THz and a dispersion coefficient of 16ps/(nm·km)) gives a minimum symbol order of 2. For

16-QAM this translates into a symbol sequence of $16^2 \times 4 = 1024$ symbols, which is less than the one used here.

After bit-to-symbol mapping, a pair of RRC filters with $\alpha = 0.1$ (giving a passband bandwidth of 5.5 GHz) are applied to the I- and Q-components. The RRC-shaped signal is then digitally up-converted to an RF frequency (f_{sc}) by feeding it to a digital IQ modulator. After this, a HT is applied to the Q-component to remove the lower frequency sideband.

In Figure 3.2 the DSP blocks used to recover the envelope detected signals are shown. The digitalized signal is first fed into a digital IQ demodulator for down-conversion to baseband. After this, a coherent DSP routine consisting of: RRC matched filtering, resampling, power normalization, and equalization is carried out. The equalizer is initialized using the RDE and then switched to the DD equalizer. Before switching to the DD equalizer, θ_{bias} in Equation 2.18 is corrected with the square QAM-adapted VV algorithm. Note that in a practical system, θ_{bias} may be removed with a single-phase rotation without the VV algorithm to reduce digital complexity [6]. A typical constellation diagram after each block is shown in Figure 3.3. After all these blocks, symbol-to-bit mapping was performed for BER measurements.

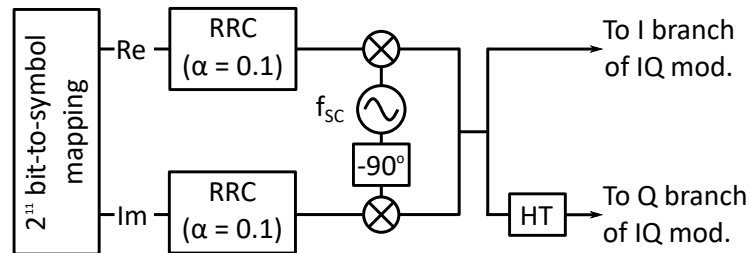


Figure 3.1: Transmitter DSP for the generation of SSB signals.

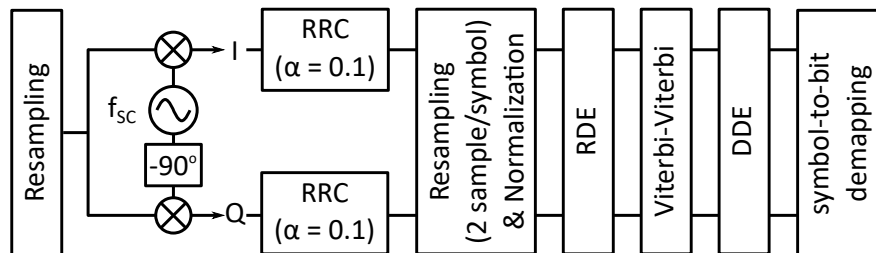


Figure 3.2: Receiver DSP for the demodulation of envelope-detected SSB signals.

3.1.2 Complete experimental arrangement

The complete experimental arrangement used in the transmission experiments is shown in Figure 3.4. The digital waveforms resultant after applying the transmitter DSP described in section 3.1, were uploaded to an arbitrary waveform generator (AWG) with an analog bandwidth of 12 GHz and operating at a sampling rate of 50 GSa/s. As shown in Figure 3.4, the generated waveforms were time-aligned with two PSs before being electrically amplified. This was done to correct a slight delay between the two channels so that a high optical sideband suppression ratio (OSSR) could be achieved. The maximum OSSR achievable with an optical modulator is approximately equal to its extinction ratio (ER) and only obtained when the signals driving the IQ-modulator are amplitude-, phase- and time-matched (i.e., there is no IQ imbalance) [7]. As can be seen from the generated optical SSB signal (inset of Figure 3.4) an OSSR of about 30 dB was obtained which matches well with the measured ER of our IQ-modulator (30.5 dB).

On the transmitter side, an external cavity laser (ECL #1) with a linewidth of 11 kHz and a wavelength of 1549 nm was used as the CW source for data modulation. After optical modulation, amplification (with an erbium-doped fiber amplifier, EDFA) and filtering, the signal was transmitted through 10 km of optical single mode fibre (SMF). When no linewidth emulation was carried out, the transmitted optical signal was combined with a second ECL (ECL #2) with a 11 kHz linewidth and a wavelength of 1551 nm (the frequency difference between the two lasers was 250 GHz). After optical amplification and filtering, the signal and the unmodulated tone were sent to an ultrafast PD. This ultrafast PD was a uni-travelling carrier (UTC) PD. In UTC PDs the absorption occurs in the p-doped layer and—unlike

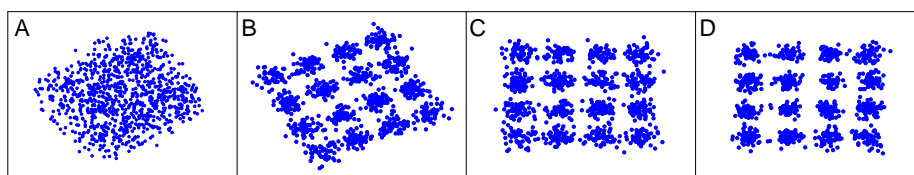


Figure 3.3: Typical constellation diagram after (A) normalization, (B) RDE, (C) VV and (D) DD equalizer.

in p-i-n PDs—only electrons diffuse into the depletion layer. As electrons have higher drift velocities than holes, UTC PDs offer higher bandwidths than p-i-n PDs, where holes also drift through the depletion layer (thus limiting their frequency response). To overcome the low responsivity of vertically-illuminated UTCs while keeping the absorber thickness required for fast operation, the UTC PD was edge-coupled. Apart from enhancing the responsivity, this configuration enabled the use of a travelling wave design to further enhance the frequency response of the UTC [8].

Horn antennas with a gain of 25 dBi were used for both transmission and reception and placed at a distance of 0.3 m from each other. A pair of lenses were

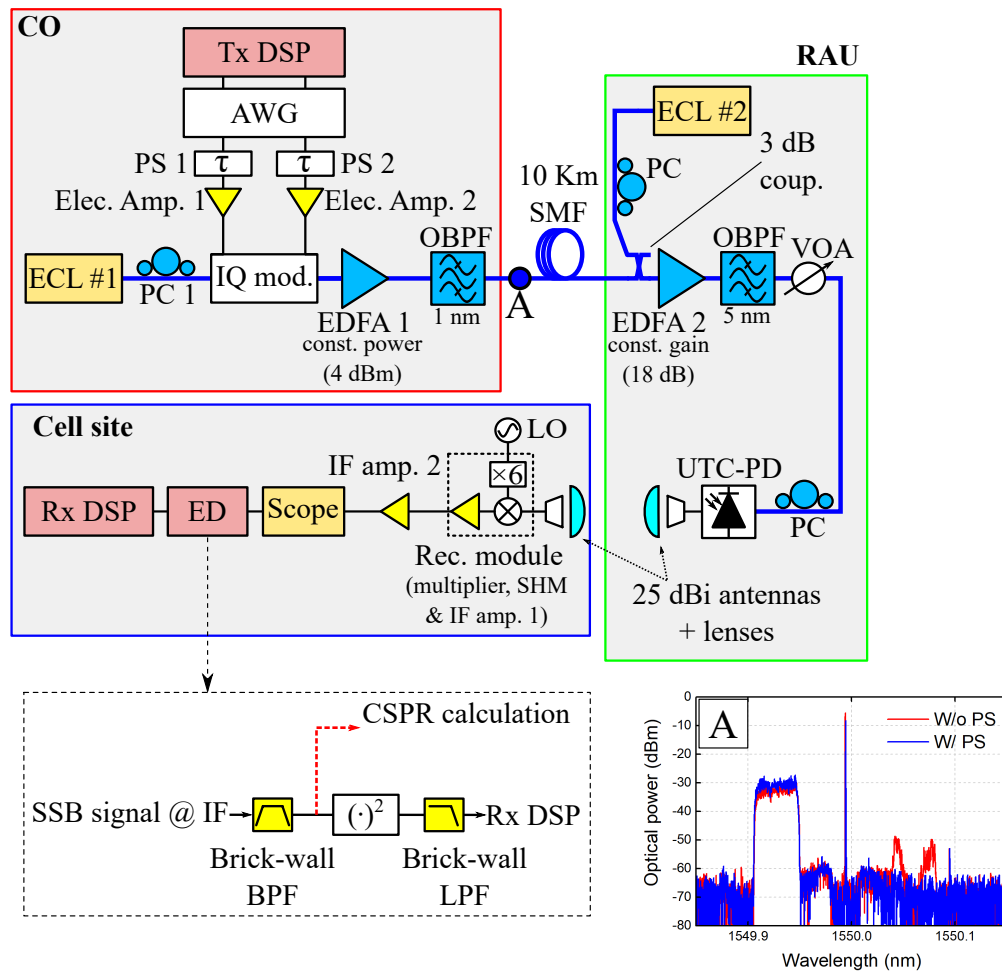


Figure 3.4: Block diagram of the experimental arrangement for the transmission of SSB THz signals (including the digital ED and the CSRR measurement point). The inset shows the optical spectrum of the generated SSB signal at point A (i.e., after EDFA1).

inserted between the two antennas to increase the collimation of the THz beam and achieve a higher transmission gain. These lenses had a diameter of 50 mm, which gives a theoretical gain of 42 dBi per lens—according to $G = (4\pi S)/\lambda^2$, where G is the gain, S is the area of the lens, and λ is the wavelength of the electromagnetic wave and corresponding to the diffraction-limited lossless case [9]—and a total 84 dB gain for the two lens-antenna pairs. Note, however, that, due to the short transmission distance used in the experiments, a link budget calculation using the Friis formula would give unrealistic results [10].

Due to the lack of a THz ED at the time of performing the measurements, the envelope detection was implemented here in the digital domain after the ADC. This is why a THz LO was used to down-convert the SSB signals to an IF. It should be noted that this configuration was only intended to replicate the performance of a system with an analog ED. The module for down-conversion consisted of a $\times 6$ multiplier, a SHM, and an IF amplifier. After down-conversion, the IF signal was amplified again and then digitized in an analog-to-digital converter (ADC) operating at 80 GSa/s. In all the transmission experiments, the duration of the recorded signal was 10 μ s, giving a total number of bits of around $2 \cdot 10^5$. With this number of bits, the lowest statistically-reliable BER that can be measured is well below 10^{-4} . This figure is much lower than the BER limits of the FEC schemes considered in this work ($\text{BER} > 10^{-3}$).

The flow chart of the ED together with the CSPR measurement point are also shown in Figure 3.4. The ED consists of a brick-wall band pass filter (BPF) to filter out the SSB signal, a squaring operation, and a brick-wall low pass filter (LPF) to remove the second order terms. All this was carried out at the sample rate of the ADC. In Table 3.1, important parameters of the components used in the experimental arrangement are summarized. Parameters such as the NF of the electrical amplifiers, the AWG effective number of bits (ENOB) and full-scale voltage (V_{FS}), as well as the modulator π voltage (V_π), will be used in section 3.3 for simulation purposes.

Table 3.1: Parameters of components used in the transmission experiments

Component	Manufacturer; version	Parameters
Elec. amp. 1, Elec. amp. 2	SHF; 807 B	Gain: 23 dB NF: 5 dB
Receiver module	VDI; WR3.4SAX	SHM conversion loss: 14 dB IF amp. 1 gain: 10 dB NF: 24 dB
IF amp. 2	Microsemi; AML618P3502	Gain: 35 dB NF: 4 dB
ECL #1, ECL #2	Pure Photonics; PPCL100	Δv : 11 kHz Max. power: 15 dB
IQ mod.	Covega; 086-40-16-SFF	ER: 30 dB V_{π} : 3.25 V
AWG	Tektronix; AWG70001A	ENOB: 4.6 V_{FS} : 500 mV

3.2 Phase robustness and spectral efficiency of SSB signals

As was shown in Equation 2.18, the envelope-detected signal has a term which is the beating of the signal with itself. If the up-conversion frequency of the SSB signal, f_{sc} , is not high enough this term can interfere with the useful signal, giving origin to the SSBI. As the mixing of the signal with itself extends from DC to the passband signal bandwidth (BW) the minimum f_{sc} that prevents the SSBI is that which generates a guard band (GB) between carrier and signal equal to the BW i.e., $f_{sc} = \frac{3}{2}BW = \frac{3R_s}{2}(1 + \alpha)$. While this is optimum in terms of SSBI it severely limits the spectral efficiency of the system. Thus, before characterizing the phase-noise tolerance of the ED-based THz system, its BER performance was characterized for different values of f_{sc} in order to determine the highest spectral efficiency allowed by the system (i.e., the SSB signal with the lowest f_{sc} that could be successfully recovered).

In Figure 3.6, the BER versus the received electrical power (measured from the recorded waveforms in the real-time oscilloscope) is shown for different f_{sc} values. On the top axis of the figure, the THz power after the the Rx antenna is also shown. This is calculated from the parameters in Table 3.1, assuming 1-dB

waveguide losses and taking into account a 3-dB attenuator that was inserted before the ADC. All this amounts to a gain factor of 27 dB which is subtracted from the received electrical power displayed in the bottom axis of Figure 3.6. For all the BER curves, the maximum input power to the PD (measured with an in-line power meter inserted before the fibre feeding the PD) was limited to 12 dBm to avoid saturation effects.

As can be seen, a f_{sc} of 6.25 GHz (GB of 3.5 GHz) was enough to satisfy the hard decision (HD)-FEC requirement (BER of $3.8 \cdot 10^{-3}$). This f_{sc} value was, therefore, the one used in the linewidth emulation measurements. The BER curve for a GB as wide as the BW (GB of 5.5 GHz) is also included to show the performance of the system when there is no SSBI. The optimum CSPR obtained for each GB is

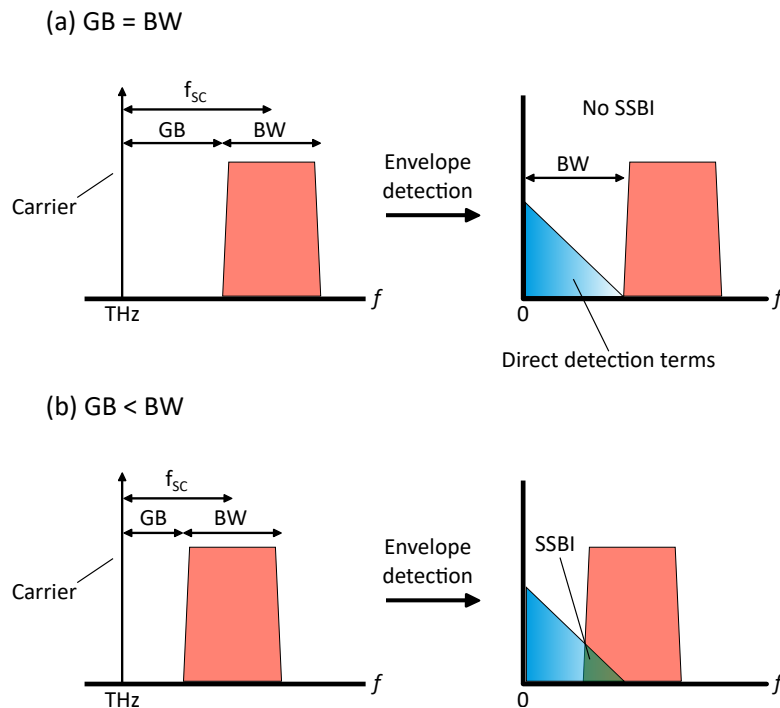


Figure 3.5: The spectrum of envelope-detected signals when (a) the guard band between carrier and signal (GB) is equal to the signal passband bandwidth (BW) and (b) when the GB is lower than the BW. In the first case the direct detection terms do not overlap with the down-converted signal after envelope detection and there is no SSBI. On the latter case there is some overlap and hence there is SSBI.

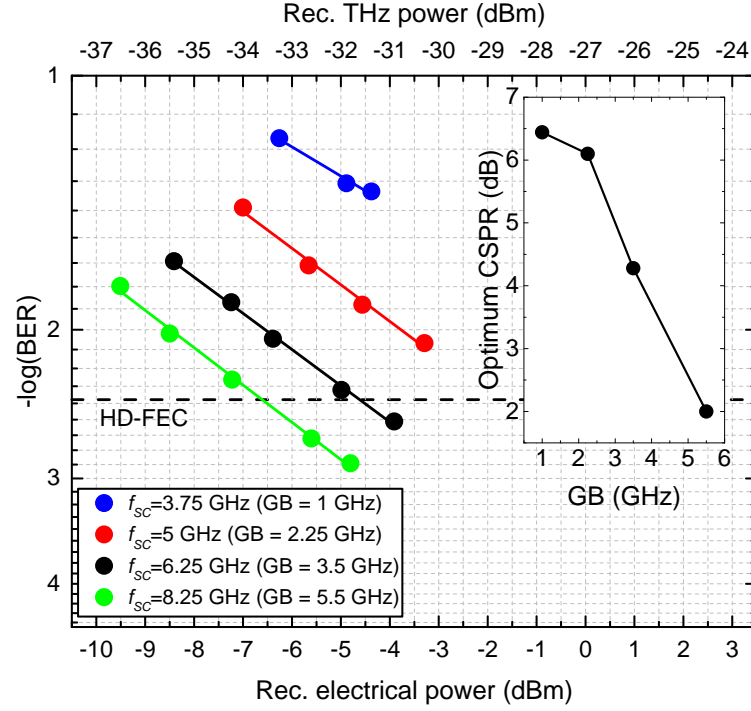


Figure 3.6: BER versus received electrical power for SSB signals with different GBs. The inset shows the optimum CSPR versus the GB.

shown as the inset. The CSPR, defined as

$$\text{CSPR}(\text{dB}) = 10 \log \left(\frac{A_C^2}{\text{E}[A_{mod}^2(t)]} \right) \quad (3.6)$$

where $\text{E}[\cdot]$ denotes statistical expectation and A_C and $A_{mod}(t)$ are the carrier and sideband amplitudes, respectively (as defined in Equation 2.14), is an important parameter in systems using envelope detection. SSB signals with low CSPR suffer from high SSBI, while high CSPR leads to reduced SNR. Thus, it is important to ensure the system always operates at the optimum CSPR value. As can be seen from Figure 3.6, the optimum CSPR increases as the GB is reduced. This is because the narrower the GB is, the higher the SSBI becomes, requiring high values of CSPR to compensate it. Wide GBs, on the other hand, can reduce or completely eliminate the SSBI, allowing operation at lower CSPRs to increase the SNR of the received signal. When using the HT and an IQ-modulator to generate the SSB signal, the tuning of the CSPR is achieved by adjusting the biasing points of the I- and Q-components in the optical modulator. To achieve high CSPRs (i.e., narrow GBs), the biasing

points must be set close to the quadrature point. On the other hand, to reduce the CSPR (i.e., wide GBs), the modulator must be biased close to the null point. To find the optimum CSPR value, at a fixed optical power input to the PD of 12 dBm, the biasing points of the I- and Q- components in the optical modulator were tuned while measuring the BER for each biasing configuration. The configuration that yielded the lowest BER was taken as the optimum one.

Once the the spectral efficiency of the system was optimized, the experiments to test the phase robustness of the SSB system were conducted. For this, a linewidth emulation stage consisting of a second AWG and an IQ modulator fed by ECL #2 was used as the optical source in the RAU. ECL #2 was modulated by several white frequency noise sequences as described in [4]. The combined linewidth of the signal laser and the linewidth emulator output was characterized separately by measuring the frequency modulation (FM) noise spectrum of the heterodyne signal between these two sources at a frequency of around 6.5 GHz. The beat note at this frequency was recorded by a 20 Gsample/s ADC and processed digitally off-line (down-converted, filtered and re-sampled) before computing the white frequency noise component [11]. The measured Lorentzian linewidths of the heterodyne signal (i.e., including ECL #1 linewidth) for the three different emulated linewidths used in the experiment were 229 kHz, 493 kHz and 905 kHz (for emulated linewidths of 200 kHz, 500 kHz, and 1 MHz, respectively). This value was used as an estimate of the linewidth of the THz signal. The results of the linewidth emulation for a f_{sc} of 6.25 GHz are plotted in Figure 3.7. In all the cases, the CSPR was optimized for the highest value of received power and then kept constant over each BER curve measurement. As can be seen, a remarkable phase noise robustness was obtained since no hint of a penalty associated with higher linewidths was observed.

If the spectral efficiency of the SSB signals is critical and the use of GBs is not acceptable, the use of DSP algorithms for SSBI cancellation can be useful. From all the algorithms that have been proposed for this purpose, the KK receiver (first demonstrated in [12]) has shown promising results in direct detection (DD) optical

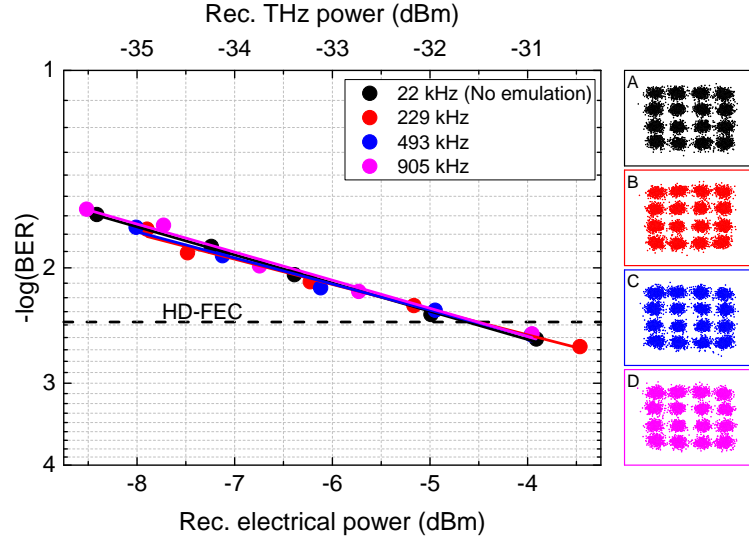


Figure 3.7: BER versus received electrical power for SSB signals with f_{SC} of 6.25 GHz and different combined optical linewidths. Insets A, B, C, and D: constellation diagrams at the lowest BER value for the 22 kHz, 229 kHz, 493 kHz and 905 kHz linewidths respectively.

networks [13]. The KK relies on the fact that the complex envelope of SSB signals is formed by an analytic signal. Analytic signals are those where the complex and real parts are linked by a HT. This relation can be exploited to retrieve the phase of a SSB signal by first measuring its amplitude, and this can be done with an ED. Taking up the notation from section 2.3.3 the THz signal from equation 2.17 can be expressed as:

$$E_{THz}(t) = \Re \left\{ U(t) e^{j(\omega_{THz}t + \theta_{bias} + \Delta\varphi(t))} \right\}, \quad (3.7)$$

where

$$U(t) = A_C + A_{mod}(t) e^{j(\omega_{RF}t + \theta_{mod}(t) - \theta_{bias})} = |U(t)| e^{j\theta(t)}, \quad (3.8)$$

From equation 3.8, one can see that the complex envelope $U(t)$ of the THz signal is formed by a DC component, A_C , and the analytic signal¹ $b(t) + j\hat{b}(t)$ (rotated by θ_{bias}). If the natural logarithm is now applied to equation 3.8, one arrives at:

$$\ln(U(t)) = \ln(|U(t)|) + j\theta(t). \quad (3.9)$$

The key point here is to know that if $A_{mod}(t) e^{j(\omega_{RF}t + \theta_{mod}(t) - \theta_{bias})}$ is an analytic

¹remember from section 2.3.3 that $b(t) + j\hat{b}(t) = A_{mod}(t) e^{j(\omega_{RF}t + \theta_{mod}(t))}$

signal, then $\ln(U(t))$ is also an analytic signal and its real and imaginary components are linked by a HT so that

$$\theta(t) = \mathbf{H}[\ln(|U(t)|)]. \quad (3.10)$$

Since $|U(t)|$ can be obtained by taking the square root of the ED output (i.e., $|U(t)| = \sqrt{I_{ED}(t)}$) one can readily obtain the data-carrying signal from equations 3.8 and 3.10 :

$$A_{mod}(t)e^{j(\omega_{RF}t + \theta_{mod}(t) - \theta_{bias})} = U(t) - A_C = |U(t)|e^{j\mathbf{H}[\ln(|U(t)|)]} \quad (3.11)$$

To arrive at equation 3.10, there is one extra condition that $U(t)$ must fulfill: it must be a minimum phase signal. This condition is ensured if $A_C > \max(A_{mod}(t))$ (i.e., if the CSPR is sufficiently big). If this condition is fulfilled, the KK receiver successfully reconstructs the complex envelope of the THz signal reaching the ED. For practical purposes, this means eliminating the DD terms and, thus, the SSBI. To see the spectral efficiency gain that can be achieved with this algorithm, the KK receiver was implemented after envelope detection and before the coherent Rx DSP (see Figure 3.2).

In Figure 3.8, the BER curves obtained with the KK algorithm are plotted for different values of f_{sc} . As can be seen, although the implementation of this algorithm was not sufficient to successfully recover a signal with no GB (at a maximum optical input power to the PD of around 12 dBm), it did allow the recovery of a signal with a GB as low as 1 GHz. For comparison, the linear-fit curves for GBs of 1 GHz and 5.5 GHz without the KK receiver are also shown in Figure 3.8. It is worth noting that, in the KK algorithm, oversampling is required to account for the square root and logarithmic operations [14]. In our case, sample rates of 6 sample/symbol and 9 sample/symbol were used for f_{sc} of 2.75 GHz and 3.75 GHz, respectively.

In Figure 3.9, the BER at a received power of -4 dBm (which is close to the maximum power recorded by the ADC in the transmission experiments) is plotted as a function of the net information spectral density (ISD) of the SSB signals (both

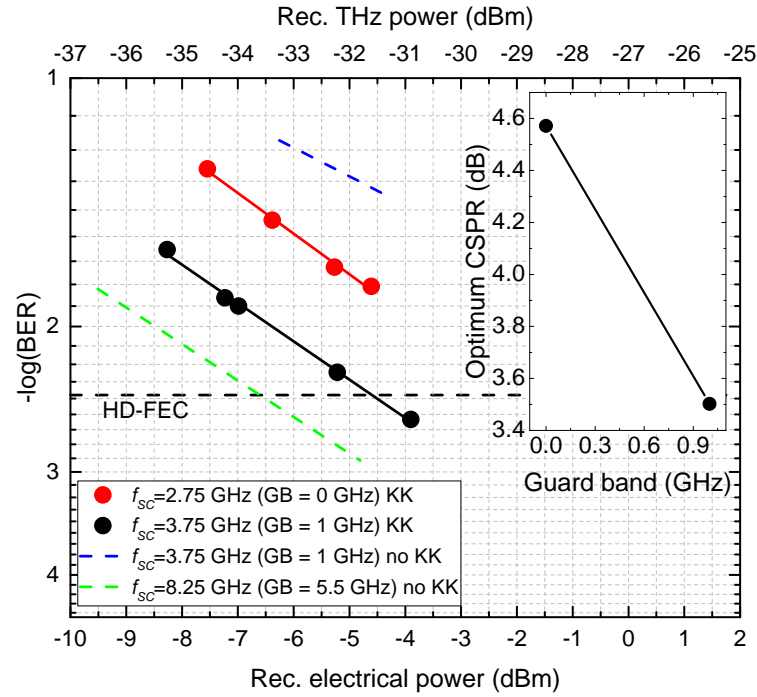


Figure 3.8: BER versus received electrical power for SSB signals using the KK receiver. The inset shows the optimum CSPPR versus the GB for the two curves taken with the KK receiver.

w/o and w/ the KK receiver). The net ISD, which is just another way to refer to the spectral efficiency of a signal, is defined as: $r \times (R_s \cdot \log_2(M)/BW)$, where r is the code rate of the FEC process (here assumed to be 0.96). It should be noted that, in the cases where the maximum received power was less than -4 dBm, the linear fit was extrapolated to find the intersection point. As expected, in both cases, the BER performance improves when the GB is increased (i.e., the ISD is reduced). The maximum ISD achievable with a SSB signal is obtained when no GB is used and is equal to that associated with the bandwidth of the data-carrying signal (i.e., BW). In our case, since the data-carrying signal was a 16-QAM signal with a RRC roll-off factor of 0.1, the maximum achievable net ISD was 3.49 b/s/Hz (this value of ISD corresponds to the left vertical axis in Figure 3.9). Compared to this upper limit, and when the KK receiver was not used, the ISD of the SSB signal had to be reduced by 39% (ISD of 2.13 b/s/Hz) to satisfy the HD-FEC requirement. On the other hand, using the KK receiver, a BER below the FEC limit could be achieved with a SSB signal with an ISD as high as 2.95 b/s/Hz, which represents just a 15%

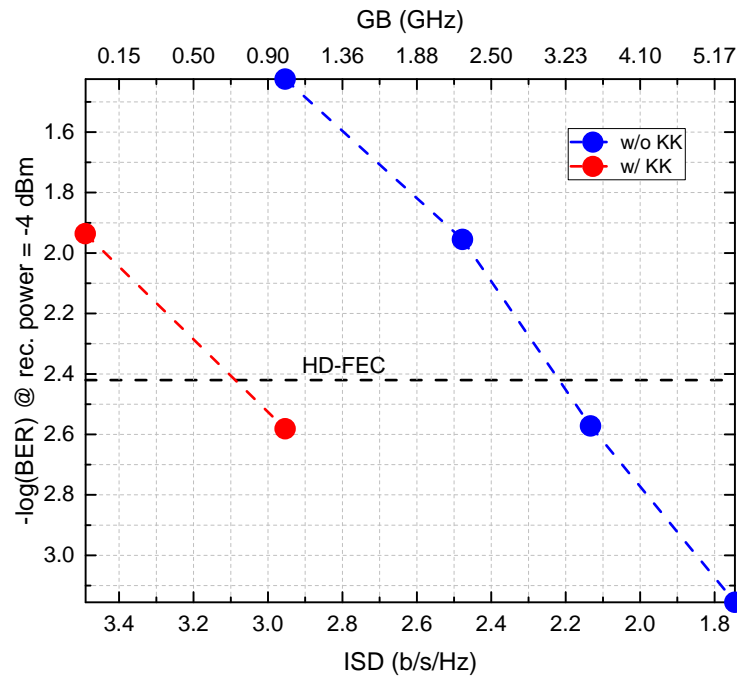


Figure 3.9: BER at a received electrical power of -4 dBm versus the net ISD of the transmitted SSB signal.

reduction with respect to the upper limit (or an improvement of 38% with respect to the system w/o KK receiver).

Compared to coherent detection of THz baseband signals, envelope-detected IM SSB signals have the disadvantage of the SSBI, which limits the sensitivity of the system. However, owing to their phase noise insensitivity, this signals can be useful in systems with high levels of phase noise. Recalling the system architecture that was presented at the beginning of the chapter, the use of low cost lasers in the RAU will be mandatory to keep a low cost per RAU. In this case, foundry-fabricated lasers (linewidths > 1 MHz) can be expected to be the choice. In this scenario and depending on the overall linewidth of the link, baseband signals, whose performance degrades with phase noise, may yield worse performance than SSB signals. To determine at which linewidth the performance surpass happens, a second linewidth emulation experiment but in this occasion with THz baseband signals was carried out.

The DSP for reception of baseband signals included, apart from the blocks used for SSB signals, the FFT-based FOE algorithm explained in section 2.3.1.2, the VV

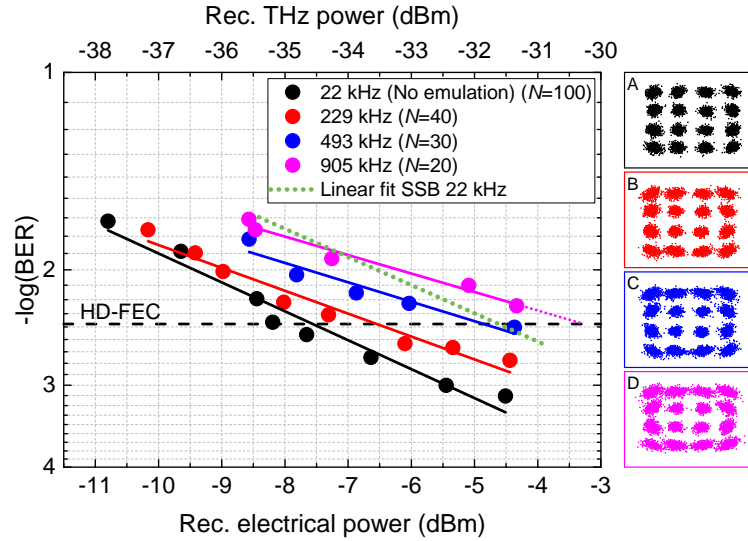


Figure 3.10: BER versus received electrical power for baseband signals and different combined optical linewidths. Insets A, B, C, and D: constellation diagrams at the lowest BER values for 22 kHz, 229 kHz, 493 kHz, and 905 kHz linewidths, respectively. The linear fit for the BER curve obtained for a SSB signal when no emulation was performed is also shown for comparison. N denotes the size of the averaging filter in the VV algorithm.

algorithm and differential decoding. The BER obtained for the baseband signals and each of the four emulated optical linewidths is shown in Figure 3.10. For each linewidth, the block length of the VV algorithm (N), was optimized for the highest received power and then kept constant over the BER measurements. As can be seen there is a clear penalty associated with phase noise. This degradation comes as the averaging filter of the VV algorithm is shortened to track the faster phase deviations introduced by broader linewidths. The shorter the averaging filter the less effective it becomes against AWGN and, hence, the higher the SNR is needed to produce a pre-determined BER. The BER curve obtained for a SSB signal and a linewidth of 22 kHz is also shown for comparison.

In Figure 3.11, the penalty at the HD-FEC threshold versus the (combined linewidth) \times (symbol period) product is plotted for both the baseband and the SSB signals. Using the dashed lines for each type of signal (for the case w/ the KK receiver we assume the penalty remains constant and extrapolate the value obtained when no linewidth emulation is performed), one can see that the penalty of baseband signals becomes higher than that of the SSB signals, both w/o and w/ KK receiver,

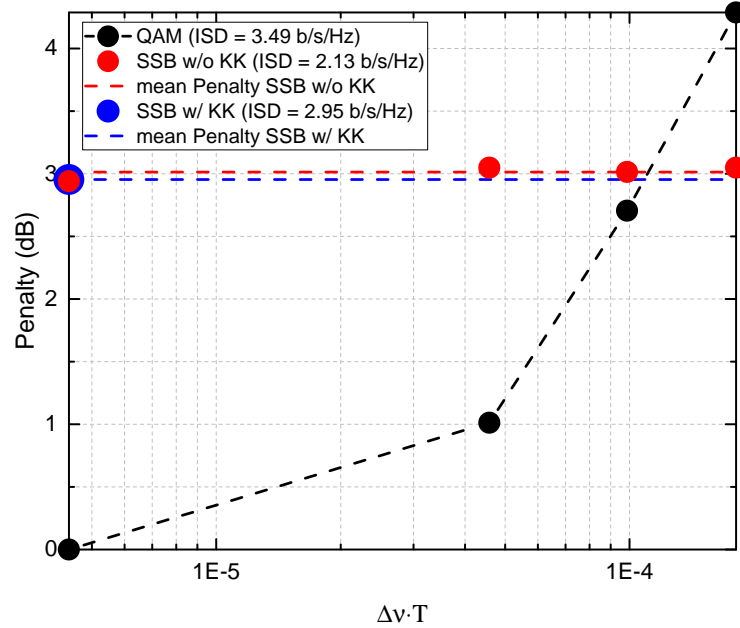


Figure 3.11: Penalty at the HD-FEC limit due to combined linewidth. In the case of the SSB signals w/ KK receiver, the penalty is assumed to remain constant with linewidth (this is experimentally verified for SSB signals w/o the KK receiver).

for a $(\Delta\nu \cdot T)$ product of approximately $1.1 \cdot 10^{-4}$. Assuming a linewidth for the RAU laser of 2 MHz (which is similar to the ones reported for foundry-fabricated DFB lasers [15]) and of 100 kHz for the laser in the CO (linewidth of off-the-shelf ECL lasers²), a combined linewidth of 2.1 MHz is obtained, which, solving for T^{-1} yields a symbol rate of approximately 19 GBd. For symbol rates lower than this, the envelope detection of SSB signals should be more effective. On the other hand, if we assume fixed symbol rates of 10 GBd and 5 GBd, combined linewidths of 1.1 MHz and 0.55 MHz, respectively, are obtained. Assuming a CO laser linewidth of 100 kHz, this translates into RAU-laser linewidths of 1 MHz and 0.45 MHz, respectively. For RAU-laser linewidths wider than this, the SSB approach should be more effective. These results seem to indicate, hence, that the envelope detection of SSB signals can offer good prospects for the deployment of low cost RAU units for THz-over-fibre systems without necessarily compromising the spectral efficiency of such links.

²Note that the use of narrow linewidth lasers in the CO is acceptable as the cost is shared between all customers supported by the network [16].

3.3 Techniques for SSB signal generation

Recalling from section 3.2, there are two possible ways to mitigate the SSBI: (a) using SSBI-cancellation DSP algorithms at the receiver and (b) allocating a GB between carrier and sideband. While the KK receiver has a great potential in terms of performance, the increased DSP associated with this technique can be a critical factor in wireless receivers, which usually have more stringent power and cost requirements than their optical counterparts. Moreover, at THz frequencies, given the large unregulated spectrum, the use of wide GBs may be a reasonable choice. However, considering the large data rates envisaged from THz communications, this approach can place stringent requirements on the analog bandwidth of the DAC used at the transmitter. In [17], the only ED-based higher-order transmission published in literature above 100 GHz (apart from the works stemming from this thesis), the bandwidth of the GB was set equal to that of the passband signal to entirely cancel the SSBI. Under these circumstances a DAC with an analog bandwidth of at least 20 GHz was required to perform the transmission.

If GBs comparable to the signal bandwidth are to be a feasible approach in THz SSB systems, it would be advantageous, thus, to find SSB generation techniques that relax the DAC bandwidth requirements. To do so, one can turn to DD optical networks, where two types of techniques have been proposed for such a purpose: the digital virtual SSB (DVSSB) [18] and the analog virtual SSB (AVSSB) [19]. In this section, the two techniques are described, paying special attention to important parameters such as required bandwidth or CSPR tuning mechanism. The quality of the optical signal generated by each technique is then studied through numerical simulations and compared to that achieved with the conventional way of generating SSB signals through the HT (in this chapter referred to as conventional SSB, CSSB). Finally end-to-end system demonstrations implementing the three techniques are realized. The SSB performance obtained for each technique is analyzed for three different GBs: 5.5 GHz, 4.75 GHz, and 3.5 GHz.

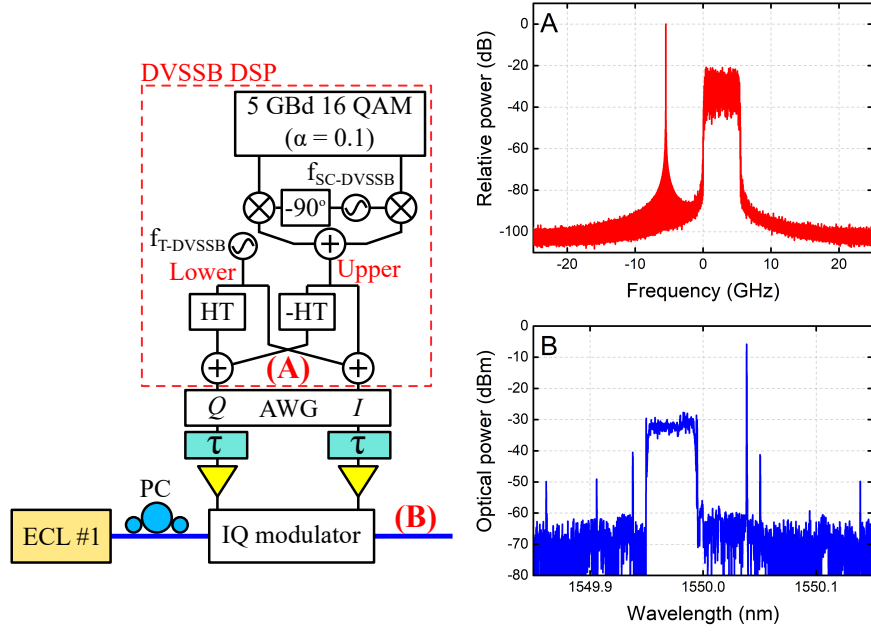


Figure 3.12: Optical DVSSB transmitter design. Inset (A) complex spectrum of the off-line digital signal for $f_{SC-DVSSB} = 2.75$ GHz and $f_{T-DVSSB} = -5.5$ GHz and (B) spectrum of the resultant optical signal (resolution bandwidth of 10 MHz). $|f_{T-DVSSB}| = 1/2[GB + S_R(1 + \alpha)]$ and $|f_{SC-DVSSB}| = GB/2$, where GB is the guard band, S_R is the symbol rate and α is the roll-off factor of the RRC filter.

3.3.1 Digital virtual SSB (DVSSB) implementation

In the DVSSB technique, the tone and the baseband signal are digitally multiplexed (see Figure 3.12) and sent to an IQ modulator, in which the I- and Q-components must be biased at the null point to suppress the optical carrier [18]. By properly setting the digital tone and sub-carrier frequencies ($f_{T-DVSSB}$ and $f_{SC-DVSSB}$, respectively), the maximum frequency of the digital signal can be reduced by a factor of 2 compared with that of CSSB (i.e. the required DAC bandwidth is now $1/2[BW + GB]$).

The CSPR is set digitally by varying the amplitude of the digital tone (for a normalized power of the baseband signal, $A = [10^{(CSPR/10)}]^{-1/2}$, where A is the amplitude of the digital tone). The digital and optical spectra for the 5.5 GHz-GB signal are shown in Figure 3.12 insets (A) and (B) respectively. As can be seen from Figure 3.12 inset (B), the OSSR achieved using this technique is also around 30 dB. The peaks >30 dB below the virtual tone are spurious peaks generated in the AWG.

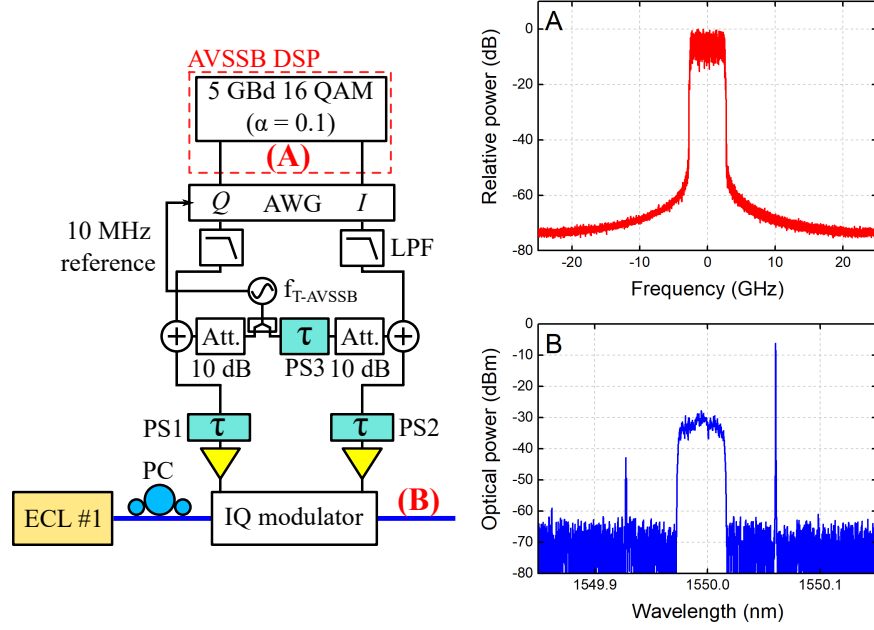


Figure 3.13: Optical AVSSB transmitter design. Inset (A) complex spectrum of the off-line digital signal, and (B) spectrum of the resultant optical signal for $|f_{T-DVSSB}| = 8.25$ GHz (resolution bandwidth of 10 MHz). $|f_{T-DVSSB}| = GB + S_R(1 + \alpha)/2$ where GB is the guard band, S_R is the symbol rate and α is the roll-off factor of the RRC filter.

3.3.2 Analog virtual SSB (AVSSB) implementation

In the AVSSB scheme, the AWG is used only to generate the baseband signal, which is then multiplexed with an RF tone in the analog domain [19], as shown in Figure 3.13. The frequency of this tone ($f_{T-AVSSB}$) is equal to the subcarrier frequency of the CSSB technique ($f_{SC-CSSB}$). Since the DAC only generates the baseband signal, the required bandwidth is $BW/2$, which compared to that in the CSSB technique, is a factor of two lower when the GB and BW are the same. As in the DVSSB technique, the IQ modulator bias points must also be set at the null point. Ideally, the CSPR is tuned by adjusting only the power from the RF synthesizer but CSPR tuning can also be achieved by decreasing the AWG output power.

The RF oscillator 10 MHz reference output signal was used as the clock signal for the AWG to ensure a good phase relationship between the data subcarrier and analog tone. The PS after the RF oscillator (PS 3 in Figure 3.13) was adjusted to provide a 90° phase shift to the RF tone. As can be seen, an OSSR between the desired and image optical tones of around 35 dB was achieved. To achieve a good suppression, both branches of the analog circuit must have the same amplitude and

phase response (as no data goes through, time-matching is not as important provided the RF oscillator has sufficiently low phase noise). To prevent the crosstalk between the I- and Q-channels, the two branches must also be properly isolated. In our case, using two 10 dB attenuators was found to be enough to suppress the crosstalk.

LPF were used to prevent excessive RF power from going into the AWG output ports. The bandwidth of these LPFs set the minimum value of GB allowed by this technique, which is the reason why the 3.5 GHz GB was chosen as the lower bound in the comparison experiments. The digital and optical spectra generated with this technique for $f_{TAVSSB} = 8.25$ GHz, are shown in Figure 3.13 insets (A) and (B) respectively.

3.3.3 Simulation results

To determine the quality of the signal produced by each technique (including the CSSB) numerical simulations were carried out in Matlab. Following the experimental configuration shown in Figures 3.12, 3.13, and the red rectangle on Figure 3.4. the waveforms generated for each technique (as explained in Section 3.3) were electronically amplified, fed to an IQ modulator and then optically amplified to a constant output power of 4 dBm. For the AVSSB technique, before electronic amplification, the waveform was combined with a tone and passed through a 7 dB attenuator (emulating the insertion loss of adapters and cables and the intrinsic 6 dB loss of the power combiner). The noise of the AWG was modelled as AWGN whose variance was calculated using the parameters provided in Table 3.1 and according to:

$$\sigma_{AWG}^2 = \left(\frac{V_{FS}^2}{8}\right) \left(\frac{BW_{sim}}{BW_{SNDR}}\right) 10^{-(0.602N+0.176)}, \quad (3.12)$$

where BW_{sim} and BW_{SNDR} are the simulation and signal-to-noise-and-distortion ratio (SNDR) measurement bandwidths respectively, and N is the ENOB. The noise generated in the electronic circuit was estimated from the NF of the transmitter amplifiers by calculating their equivalent noise temperature. For the AVSSB technique, the NF of the attenuator block, which was set as its attenuation value, was also considered in the calculation. The gain of the electronic amplifiers was ad-

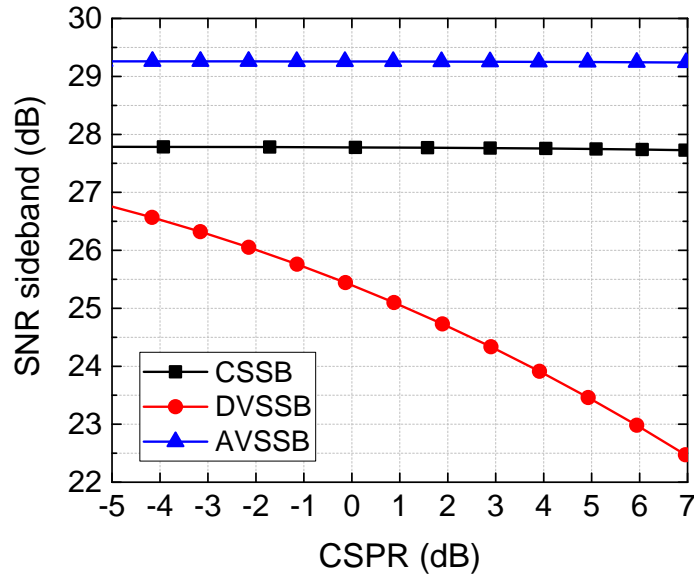


Figure 3.14: Optical sideband SNR versus CSPPR for each technique.

justed to avoid nonlinear distortions in the IQ modulator, which was illuminated with an optical power of 5 dBm. As in the experimental transmissions, the output of the modulator was amplified to an optical power of 4 dBm with an EDFA. To compute the amplified spontaneous emission (ASE) noise, a spontaneous factor of 1.5 was used.

The SNR of the optical SSB signal was used as the figure of merit for the comparison and was evaluated as:

$$\text{SNR} = \frac{\text{E}[|X|^2]}{\text{E}[|Y - X|^2]}, \quad (3.13)$$

where X and Y are the symbols generated at the digital transmitter and after optical amplification, respectively, and $\text{E}[\cdot]$ denotes statistical expectation. Figure 3.14 shows the sideband SNR versus the CSPPR for the three techniques. Assuming a linear conversion from the electronic to the optical domain (and neglecting the frequency response of the system), the SNR of the sideband is independent of the GB so only the results for the 5.5 GHz GB are shown.

As can be seen from Figure 3.14, the SNR of both the AVSSB and CSSB techniques remains constant while that of the DVSSB degrades with CSPPR. This is because, unlike in the first two schemes, the electrical power allocated to the

sideband in the DVSSB technique decreases as the CSPR is increased. The higher SNR of the AVSSB technique compared to that of the CSSB scheme, accounts for the fact that the average power of the baseband waveform (i.e. the AVSSB technique) was higher than that of the up-converted waveform (CSSB). In the digital waveforms used in the experiment, the difference was 1.8 dB. The lower value found in Figure 3.14 between the AVSSB and CSSB curves (1.5 dB) comes from the slight SNR degradation that is caused by the attenuator in the AVSSB signal. Contrary to what could be expected, this attenuation does not degrade much the quality of the signal because of two reasons: (a) the noise from the AWG is much higher than the noise introduced by the attenuator and (b) even attenuated, the electrical noise dominates over ASE noise.

3.3.4 System demonstrations

In this section all the techniques are implemented in a THz system using the experimental arrangement shown in Figure 3.4 (but without fiber transmission between the CO and RAU) . In the THz transmissions, receiver noise (dominated by the large NF of the WR3.4SAX module, see Table 3.1) prevailed over transmitter noise. Taking into account this and the fact that the power of the optical SSB signal was the same in all techniques (EDFA was operated in constant output power mode) similar results between the technique are to be expected.

In Figure 3.15, the obtained BER with each technique is shown as function of the CSPR for the 5.5 GHz, 4.75 GHz and 3.5 GHz GBs (at an input optical power to the PD of 12.9 dBm). As can be seen, in all the cases, the BER reaches a minimum for a certain CSPR value and then it degrades for both lower and higher CSPRs. For the 4.75 GHz- and the 3.5 GHz-GB transmissions, where the GB was less than the BW, the performance degradation at lower CSPR values is caused by the SSBI, as noted in Figure 3.15 (B) and (C), respectively. In the case of the transmission with the 5.5 GHz-GB signal, where the GB was equal to the BW (i.e., there was no SSBI), the BER performance deterioration at lower CSPRs is caused by the sideband-noise beating interference [20], as noted in Figure 3.15 (A). On the other hand, at higher CSPRs, the system becomes limited by the decrease in

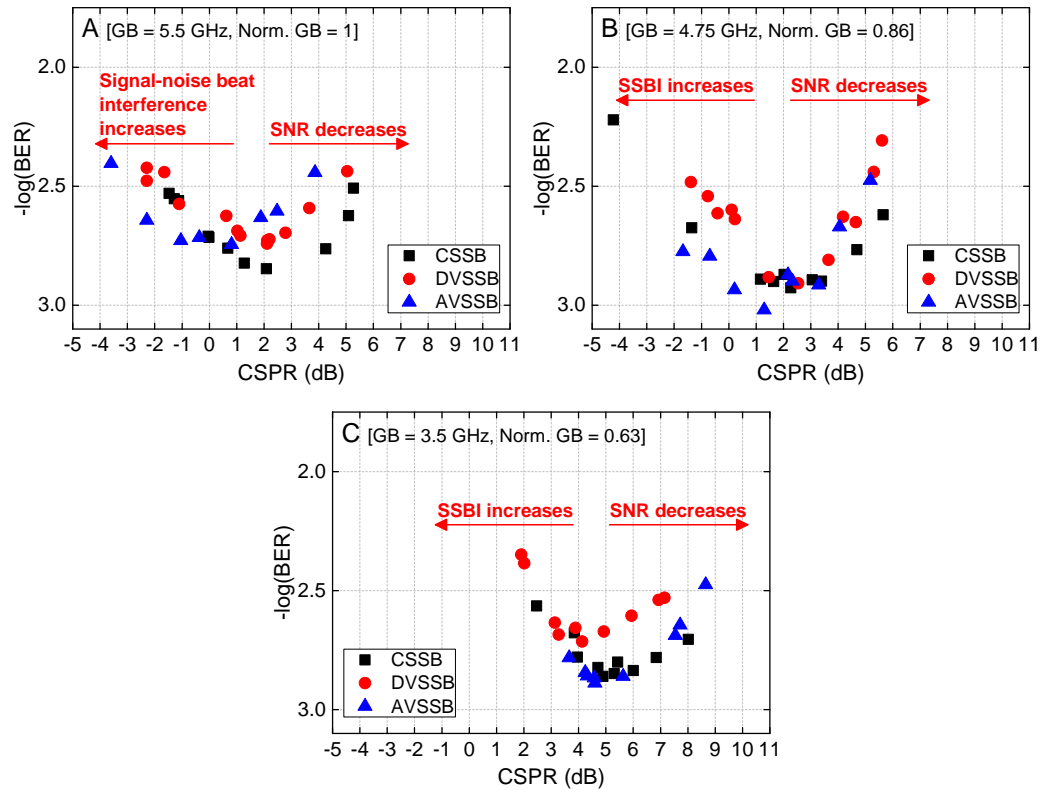


Figure 3.15: BER versus CSPP for the (A) 5.5 GHz, (B) 4.75 GHz, and (C) 3.5 GHz GBs and at an input optical power to the PD of 12.9 dBm. The normalized GB (GB/BW) is also indicated inside the brackets.

SNR that results from the reduction in sideband power. Note that, although the SNR and the electrical power of the sideband remain constant in the CSSB and AVSSB techniques, the power of the sideband after optical amplification decreases with CSPP in the three techniques, as a consequence of EDFA 1 being operated in a constant output power mode.

In Figure 3.16, the optimum CSPP as function of the normalized GB (GB/BW) is shown for each technique. As expected the optimum CSPP increases as the GB decreases to tackle the increase of SSBI. As can be seen, the AVSSB technique presents lower values of optimum CSPP for the 5.5 GHz and 4.75 GHz GBs. For a certain GB, a lower optimum value of CSPP means the technique suffers from lower SNR [21]. Since these deviations do not match with the simulation results, these lower values are likely to be due to experimental errors (due to the quantized nature of the CSPP measurements or a decrease in the transmitted THz power due

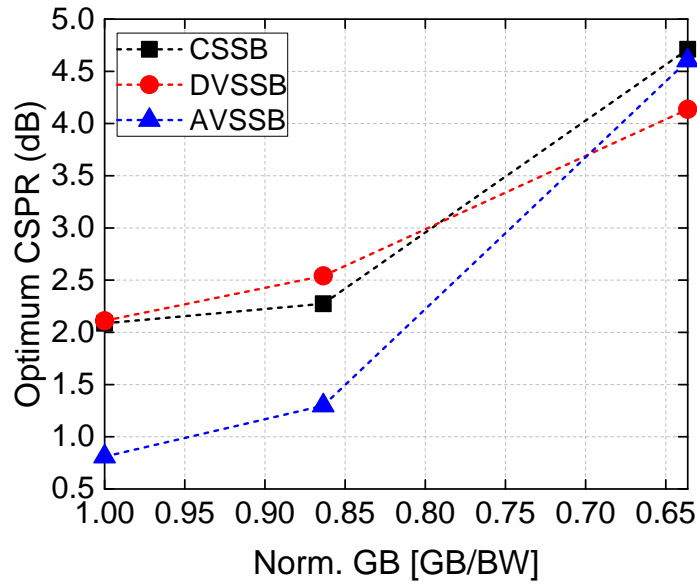


Figure 3.16: Optimum CSPR versus normalized GB.

to fiber-PD misalignments or polarization mismatches, for example).

In Figure 3.17, the BER curves for each GB and technique are plotted as a function of the total received electrical power, as measured from the recorded waveform in the ADC. The CSPR was adjusted to match the optimum one shown in Figure 3.16 and then kept fixed over each BER measurement. In Figure 3.18, the penalty at the HD-FEC limit is shown as function of the normalized GB.

While the absolute performance of the three schemes is very similar for the 4.75 GHz and 5.5 GHz GBs, the penalty substantially increases for the 3.5 GHz GB due to increased SSBI. In terms of relative performance, one can see that the AVSSB exhibits a slight penalty at the 5.5 GHz and 4.75 GHz GBs, but no penalty at the 3.5 GHz GB with respect to the CSSB technique. This penalty (which is less than 0.6 dB) could have been caused by a non-optimum CSPR due to the reasons discussed previously. Regarding the DVSSB technique, it can be seen from Figure 3.18 that its penalty increases progressively as the GB is reduced, eventually reaching 1 dB at the 3.5 GHz GB. This could seem to be due to the decrease in SNR with CSPR associated with this technique. However, since transmitter AWGN should not increase with CSPR (i.e., receiver noise still dominates), this is not likely to be the cause. We rather attribute this to nonlinear distortions (in the AWG, electronic amplifier or

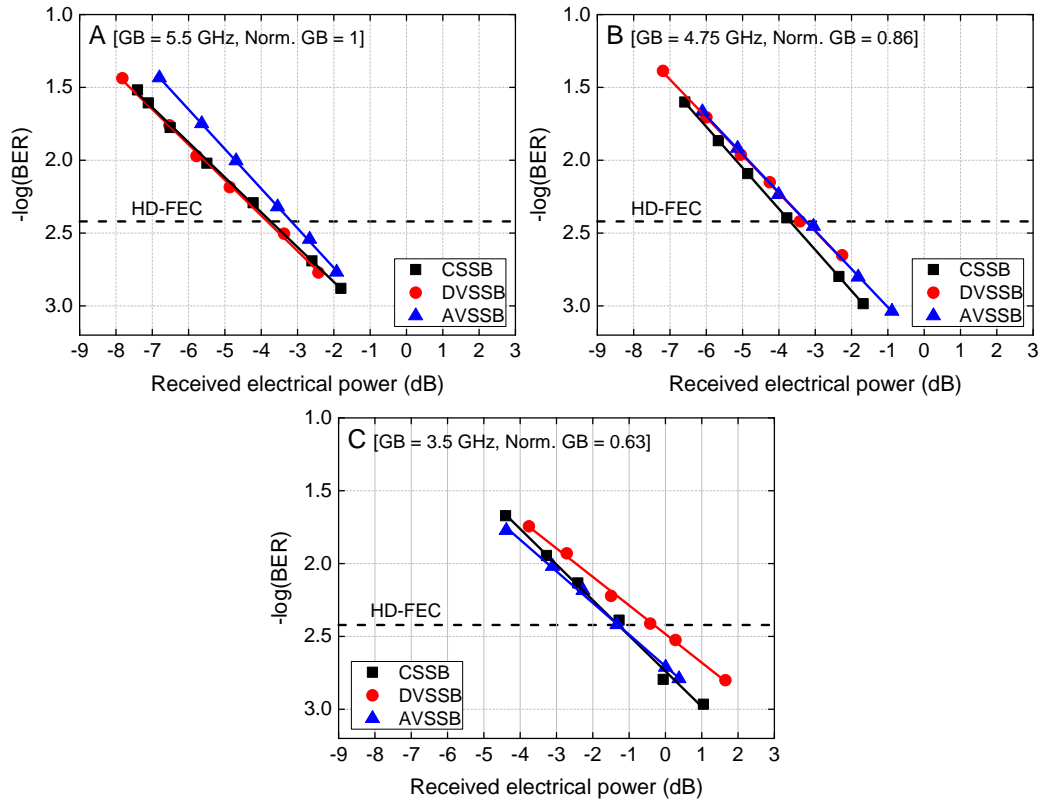


Figure 3.17: BER versus received electrical power for the (A) 5.5 GHz, (B) 4.75 GHz, and (C) 3.5 GHz GBs. The normalized GB is also indicated inside the brackets.

optical modulator) caused by the increase in the virtual tone power.

3.4 Summary and conclusions

The sensitivity to optical LO linewidth of a THz-over-fibre system based on SSB signals & envelope detection has been characterized. Before doing so, the impact of GB has been investigated to determine the highest spectral efficiency allowed by the system. Finally, the obtained results have been compared with those obtained with baseband signals & carrier recovery. Using 5 GBd 16-QAM signals, it has been confirmed that the SSB scheme, unlike the baseband approach, shows no penalty associated with linewidth. Furthermore, it has been found that, for a total optical linewidth wider than 0.55 MHz, this approach yields better sensitivity. This, however, was achieved at the expense of reducing the ISD of the SSB signal by 39% compared to the maximum achievable (which is obtained when no GB is used between carrier and sideband). On the other hand, using the KK receiver to mitigate

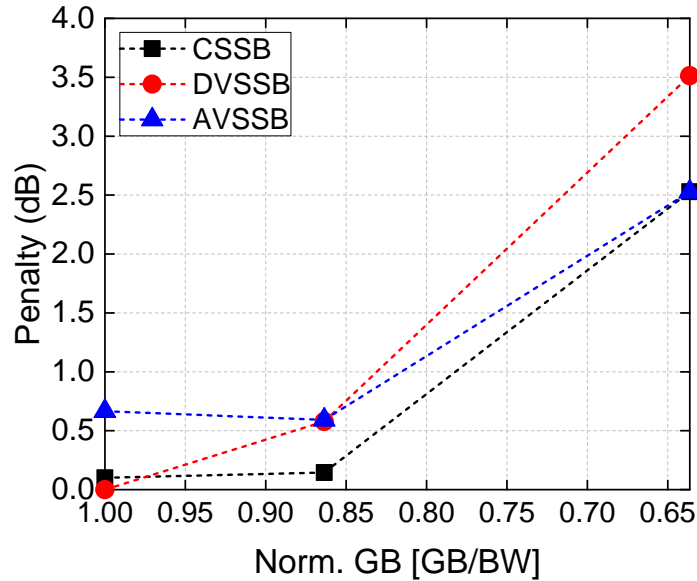


Figure 3.18: Penalty (taking the lowest received electrical power yielding a BER below the FEC limit on Figure 3.17 as reference) versus normalized GB.

the SSBI, only a 15% reduction of the ISD was needed to meet the HD-FEC requirement. The envelope detection of SSB signals, therefore, is a promising solution to enable the use of low-cost free-running lasers in THz-over-fibre systems.

In the second part of this chapter, Two SSB techniques that relax the bandwidth requirements of the DAC, namely AVSSB and DVSSB, were introduced to the field of THz communications. Their performance was compared against that of the CSSB technique through numerical simulations. Then the end-to-end implementation of a THz system employing each of the three technique was demonstrated for three different GBs. The results of the simulations show that, unlike in the CSSB and AVSSB schemes, the quality of the sideband generated with the DVSSB degrades as the CSPR is increased. This is because, in this scheme, the electrical power allocated to the sideband also decreases with CSPR. Between the CSSB and AVSSB techniques, the AVSSB exhibits slightly better SNR as the average power of the baseband waveform is higher than that of the up-converted one. In the transmission experiments, where receiver noise dominates, similar behavior was found between the three techniques. At the 3.5 GHz GB, however, the DVSSB exhibited a penalty of 1 dB with respect the other two. This is likely to be due to nonlinear distortions caused by the increase in the virtual tone power. As a sum-

Table 3.2: Summary of SSB techniques

	CSSB	DVSSB	AVSSB
DAC bandwidth	High $BW + GB$	Medium $1/2[BW + GB]$	Low $BW/2$
CSPR tunning	IQ-mod. biasing points	DSP	RF synthesizer power
IQ-mod. biasing points	Accorsing to desired CSPR	Null	Null
DSP complexity	High	High	Low
Analog complexity	Low	Low	High
Main problem	High DAC bandwidth	Reduction in sideband SNR with CSPR	Analog complexity

mary, the main features of each technique, together with the main problem faced by each of them, are summarized in Table 3.2.

Bibliography

- [1] Christina Lim, Ampalavanapillai Nirmalathas, Masduzzaman Bakaul, Prasanna Gamage, Ka Lun Lee, Yizhuo Yang, Dalma Novak, and Rod Waterhouse. Fiber-wireless networks and subsystem technologies. *Journal of Lightwave Technology*, 28 (4):390–405, 2010. ISSN 07338724. doi: 10.1109/JLT.2009.2031423.
- [2] Jianjun Yu, Zhensheng Jia, Ting Wang, and Gee Kung Chang. A novel radio-over-fiber configuration using optical phase modulator to generate an optical mm-wave and centralized lightwave for uplink connection. *IEEE Photonics Technology Letters*, 19 (3):140–142, 2007. ISSN 10411135. doi: 10.1109/LPT.2006.890087.
- [3] M Sezer Erklnc, Zhixin Liu, Thomas Gerard, Robert I Killey, and Polina Bayvel. Bidirectional Symmetric 25G Coherent ONU Using a Single Laser , Single-ended PIN and a 2-bit ADC. 2018.
- [4] Zuraidah Zan and Arthur James Lowery. Experimental demonstration of a flexible and stable semiconductor laser linewidth emulator. *Optics express*, 18(13):13880–13885, 2010. ISSN 1094-4087. doi: 10.1364/OE.18.013880.
- [5] Matthias Seimetz. *High-Order Modulation for Optical Fiber Transmission*, volume 143 of *Springer Series in Optical Sciences*. Springer Berlin Heidelberg, Berlin, Heidelberg, 2009. ISBN 978-3-540-93770-8. doi: 10.1007/978-3-540-93771-5. URL <http://link.springer.com/10.1007/978-3-540-93771-5>.
- [6] Yixiao Zhu, Mingxuan Jiang, Xiaoke Ruan, Chenjia Li, and Fan Zhang. 112Gb / s Single-Sideband PAM4 WDM Transmission over 80km SSMF with Kramers-Kronig Receiver. In *Optical Fiber Communcation*, San Diego, 2018.
- [7] M. Sezer Erkilinc, Manoj P. Thakur, Stephan Pachnicke, Helmut Griesser, John Mitchell, Benn C. Thomsen, Polina Bayvel, and Robert I. Killey. Spectrally efficient WDM nyquist pulse-shaped subcarrier modulation using a dual-drive Mach-Zehnder modulator and direct detection. *Journal of Lightwave Technology*, 34(4):1158–1165, 2016. ISSN 07338724. doi: 10.1109/JLT.2015.2497343.
- [8] Efthymios Rouvalis, Cyril C. Renaud, David G. Moodie, Michael J. Robertson, and Alwyn J. Seeds. Continuous wave Terahertz generation from ultra-fast InP-based photodiodes. *IEEE Transactions on Microwave Theory and Techniques*, 60(3 PART 1):509–517, 2012. ISSN 00189480. doi: 10.1109/TMTT.2011.2178858.
- [9] David Pozar. *Microwave engennering*. 1385. ISBN 9780470631553. doi: TK7876.P692011. URL <http://scholar.google.com/scholar?hl=en&btnG=Search&q=intitle:No+Title#0>.
- [10] Harald Friis. Simple Transmission Formula. *Proceedings of the IRE and Waves and Electrons May*, (1):254–256, 1946. ISSN 0096-8390. doi: 10.1109/JRPROC.1946.234568.
- [11] Irshaad Fatadin, David Ives, and Seb J. Savory. Differential carrier phase recovery for QPSK optical coherent systems with integrated tunable lasers. *Op-*

- tics Express*, 21(8):10166, 2013. ISSN 15383598. doi: 10.1001/jama.1991.03460050119042. URL <https://www.osapublishing.org/oe/abstract.cfm?uri=oe-21-8-10166>.
- [12] Herbert Voelcker. Demodulation of Single-Sideband Signals Via Envelope Detection. *IEEE Transactions on Communication Technology*, 14(1):22–30, 1966. ISSN 00189332. doi: 10.1109/TCOM.1966.1089285.
- [13] Zhe Li, M. Sezer Erkilinc, Kai Shi, Eric Sillekens, Lidia Galdino, Benn C. Thomsen, Polina Bayvel, and Robert I. Killey. SSBI mitigation and the kramers-kronig scheme in single-sideband direct-detection transmission with receiver-based electronic dispersion compensation. *Journal of Lightwave Technology*, 35(10):1887–1893, 2017. ISSN 07338724. doi: 10.1109/JLT.2017.2684298.
- [14] Mark Shtaif Antonio Mecozzi, Cristian Antonelli. Kramers Kronig coherent receiver. *Optica*, 3(11):1220–1227, 2016. URL <https://www.osapublishing.org/optica/abstract.cfm?uri=optica-3-11-1220>.
- [15] Mu-Chieh Lo, Alberto Zarzuelo, Robinson Guzman, and Guillermo Carpintero. Monolithically Integrated Microwave Frequency Synthesizer on InP Generic Foundry Platform. *Journal of Lightwave Technology*, 36(19):4626–4632, 2018. ISSN 0733-8724. doi: 10.1109/JLT.2018.2836298. URL <https://ieeexplore.ieee.org/document/8358771/>.
- [16] M. S. Erklilng, D. Lavery, K. Shi, B. C. Thomsen, R. I. Killey, S. J. Savory, and P. Bayvel. Bidirectional wavelength-division multiplexing transmission over installed fibre using a simplified optical coherent access transceiver. *Nature Communications*, 8(1):1–10, 2017. ISSN 20411723. doi: 10.1038/s41467-017-00875-z.
- [17] Maria Freire Hermelo, Po-Tsung (Boris) Shih, Matthias Steeg, Anthony Ngoma, and Andreas Stöhr. Spectral efficient 64-QAM-OFDM terahertz communication link. *Optics Express*, 25(16):19360, 2017. ISSN 1094-4087. doi: 10.1364/OE.25.019360. URL <https://www.osapublishing.org/abstract.cfm?URI=oe-25-16-19360>.
- [18] Wei-Ren Peng, Xiaoxia Wu, Kai-Ming Feng, Vahid R. Arbab, Bishara Shamee, Jeng-Yuan Yang, Louis C. Christen, Alan E. Willner, and Sien Chi. Spectrally efficient direct-detected OFDM transmission employing an iterative estimation and cancellation technique. *Optics Express*, 17(11):9099, 2009. ISSN 1094-4087. doi: 10.1364/OE.17.009099. URL <https://www.osapublishing.org/oe/abstract.cfm?uri=oe-17-11-9099>.
- [19] Cheng Ju, Na Liu, Xue Chen, and Zhiguo Zhang. SSBI Mitigation in A-RF-Tone-Based VSSB-OFDM System with a Frequency-Domain Volterra Series Equalizer. *Journal of Lightwave Technology*, 33(23):4997–5006, 2015. ISSN 07338724. doi: 10.1109/JLT.2015.2495340.
- [20] Arthur James Lowery. Amplified-spontaneous noise limit of optical OFDM lightwave systems. *Optics Express*, 16(2):860, 2008. ISSN 1094-4087. doi: 10.1364/OE.16.000860. URL <https://www.osapublishing.org/oe/abstract.cfm?uri=oe-16-2-860>.
- [21] M. Sezer Erkilinc, Zhe Li, Stephan Pachnicke, Helmut Griesser, Benn C. Thomsen, Polina Bayvel, and Robert I. Killey. Spectrally Efficient WDM Nyquist Pulse-Shaped 16-QAM Subcarrier Modulation Transmission with Direct Detection. *Journal of Lightwave Technology*, 33(15):3147–3155, 2015. ISSN 07338724. doi: 10.1109/JLT.2015.2427111.

Chapter 4

THz wireless bridges

As highlighted in section 2.1.1, wireless bridges are one of the main applications currently envisaged for THz links. This chapter focuses on the design and experimental demonstration of THz wireless bridges. In section 4.1, the experimental arrangement used throughout this chapter, as well as the DSP used in the digital receiver, is highlighted. In this section, the results obtained for a single-channel wireless bridge transmitting 20 Gbit/s are discussed. Furthermore, the phase noise tolerance of the proposed system is experimentally characterized by replacing the RAU ECL with a DFB laser. The performance of the same system transmitting baseband signals is also characterized and used as a reference for comparison with the proposed system. In section 4.2, the proposed wireless bridge is demonstrated in the context of a WDM network scenario, where the CO transmits several optical channels and the RAU selects one of them for wireless transmission. In section 4.3, two wireless channels are transmitted simultaneously in an effort to increase the number of users supported by the wireless bridge, achieving a net data rate of 35 Gbit/s under the assumption of soft decision (SD)-FEC. Finally, in section 4.4, a 40 Gbit/s wireless bridge is realized by using advanced DSP both in the transmitter and receiver.

4.1 Tone-assisted THz wireless bridge

Figure 4.1 presents a depiction of a THz wireless bridge based on photonic technologies. As can be seen, various methods for THz-to-optical conversion can be

used in the receiver RAU (only schemes supporting higher-order modulation are considered). The simplest one is the direct mapping of the incoming THz field to the optical domain via an ultra-wide bandwidth optical modulator. Recently, several demonstrations of this concept using plasmonic modulators (which can exhibit remarkably high electrical bandwidths) have been reported [1] [2]. After optical mapping, an optical filter is needed to select one of the data-carrying sidebands. However, since the wavelength separation between carrier and sideband will be at least a couple of nm if the transmission is at THz frequencies, a narrow-bandwidth optical band pass filter (OBPF) is not required.

The alternative approach is to down-convert the THz signal first and then perform the up-conversion to the optical domain via a conventional optical modulator. For THz down-conversion either an homodyne [3], heterodyne [4] [5], or ED-based receiver can be used. The advantage of the homodyne receiver is that no redundant signal is generated and, hence, it does not require a narrow-bandwidth OBPF to remove it. On the other hand, down-conversion to an IF, either with an ED or heterodyne receiver, greatly simplifies the number of high-frequency components in the receiver RAU, making it a more cost-effective solution.

In Table 4.1, relevant experiments on wireless bridges supporting higher order modulation formats are summarized. For the sake of comparison only transmissions achieving (gross) BERs below the HD-FEC limit of $3.8 \cdot 10^{-3}$ are shown. The highest data rate fulfilling this condition so far is 80 Gbit/s, which was achieved using polarization multiplexing (PM) and 16-QAM modulation. However, this was obtained in a system operating at a carrier frequency below 100 GHz [6]. Above 100 GHz, systems supporting only QPSK — in either single carrier or multi-carrier (i.e., orthogonal frequency division multiplexing, OFDM) formats — have been demonstrated to date. The realization of a wireless bridge at THz frequencies with a more efficient format is, thus, a pending task. Although an electronic approach is used in [3] for THz generation, this reference is included for completeness.

As shown in Figure 4.1, depending on the type of receiver used at the ONU, the link can have either 3 or 4 free-running lasers (note that only schemes 2 and 3 are

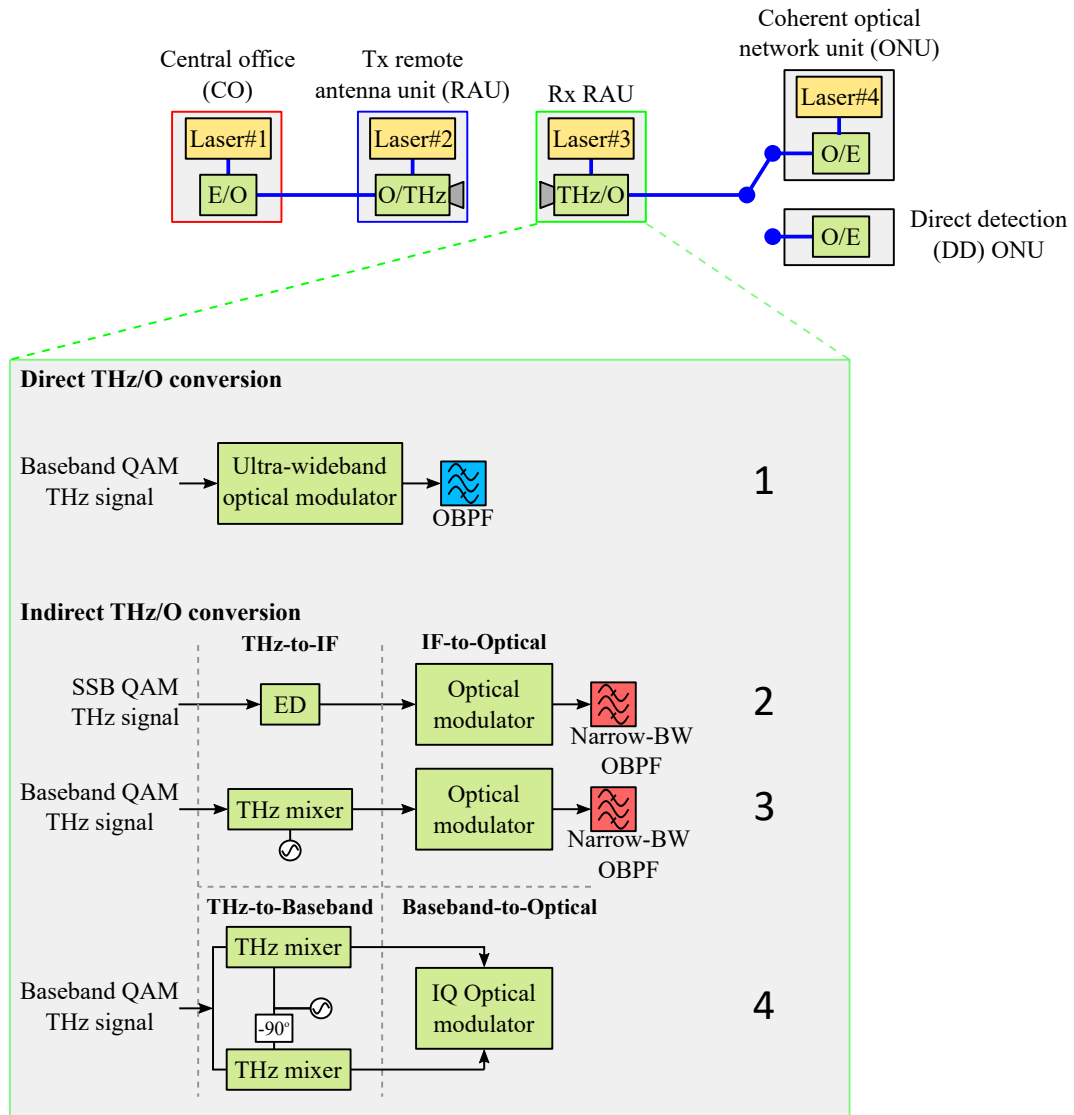


Figure 4.1: Schematic representation of a wireless bridge based on photonic THz generation.

compatible with a DD ONU; in schemes 1 and 4 a coherent optical receiver must be employed to recover the signal). Thus, to enable the use of foundry-fabricated lasers while not incurring on a high penalty, a phase noise-robust technique is essential in this type of links. For this reason, an ED may seem the most appropriate solution. However, the increased sensitivity associated with mixers may be crucial to achieve an adequate SNR upon optical conversion at the Rx RAU . To keep the phase noise tolerance associated with EDs while using heterodyne down-conversion, one may use the pilot tone-assisted technique. In this scheme, a pilot tone is added to the

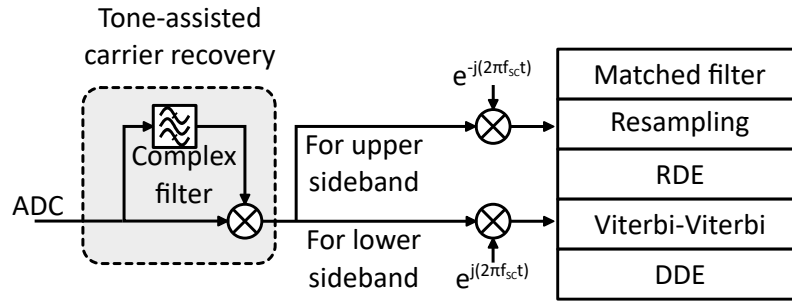


Figure 4.2: Receiver DSP including the tone-assisted technique.

baseband signal and transmitted through the link. In the digital receiver, this tone is first filtered out and then mixed with the unfiltered signal for frequency offset and phase noise compensation. Note that, although the mixing is, in this case, performed digitally rather than with an ED, the same analysis as in section 2.3.3 holds true.

The carrier recovery approach implemented in this work at the ONU is divided into two stages. In the first stage, the pilot tone-assisted technique is used for FOE and coarse PE. In the second stage, the square QAM-adapted VV is only used to compensate a fixed phase offset. To add the pilot tone to the data-carrying signal, the SSB-with carrier format is employed. Note that the phase offset that the second stage aims to correct arises from the biasing points of the I- and Q-components in the optical modulator as detailed previously in Equation 2.14. The complete receiver DSP, including RDE and DD equalization is shown in Figure 4.2. Using such a data recovery scheme at the ONU made it possible to achieve single channel transmission at 250 GHz and a net data rate of 20 Gbit/s (5 GBd 16-QAM signals). In the first instance, the experiment was performed without optical transmission. A total length of optical fiber of 50 km (10 km between CO and Tx RAU and 40 km between Rx RAU and ONU) was then inserted. In such transmissions, the Tx RAU and Rx RAU shared an ECL. To see the phase noise penalty of the proposed carrier recovery scheme, the ECL was replaced by a DFB laser at the Tx RAU. Finally, the obtained results were compared with those obtained when transmitting baseband signals. The DSP used in the reception of baseband signals, included the FFT-based FOE, the VV algorithm for PE, and differential decoding to avoid cycle slips.

Table 4.1: Summary of relevant wireless bridge transmission experiments supporting higher order modulation

Freq. (GHz)	Rate (Gbit/s); Format	Wireless distance (cm)	THz emitter	Optical distance (km)	THz/O tech.	Ref.
60	10/20; QPSK	500/100	PD	-	1	[1]
95	80; PM-16QAM	100	PD	100	3	[6]
220	9; OFDM-QPSK	50	MMIC	40	3	[3]
288.5	36;QPSK	1600	PD	-	1	[2]
300	40;QPSK	10	PD	10.5	3	[4]
450	13;QPSK	380	PD	12.2	3	[5]

The complete experimental arrangement used for transmission is shown in Figure 4.3. For digital signal generation, four 2^{11} de Bruijn bit sequences were mapped into the 5 GBd 16-QAM symbols using Matlab. For SSB signal generation, after applying a RRC filter with a roll-off factor of 0.1, the signal was up-converted to a frequency of 3.5 GHz, giving a GB between tone and signal of 500 MHz (note that in this case, since the tone and the data-carrying signal are linearly mixed, no DD terms are present upon detection and, thus, there is no need for large GBs). The resultant waveforms after applying the transmitter DSP were uploaded to an AWG operating at 50 GSa/s. The two signals generated in the AWG were time-aligned with two PS and electronically amplified before being fed to the optical modulator. At the CO, an ECL (ECL#1) emitting at a wavelength of 1549 nm was used for data modulation.

The optical signal received at the Tx RAU was combined with a second optical tone (from ECL#2 or DFB#1) at a wavelength of 1551 nm. After optical amplification and filtering, the two optical tones were fed into an unpackaged PD by means of a lensed fiber. Horn antennas with a gain of 25 dBi were used for both transmission and reception and placed at 0.2 m from each other. A pair of lenses were inserted between the two antennas to increase the collimation of the THz beam. On the Rx RAU, the signal was down-converted to a frequency of around 11 GHz with an enclosed receiver module consisting of a 6 multiplier, a SHM, and an IF amplifier. After down-conversion, the IF signal was passed through two additional IF ampli-

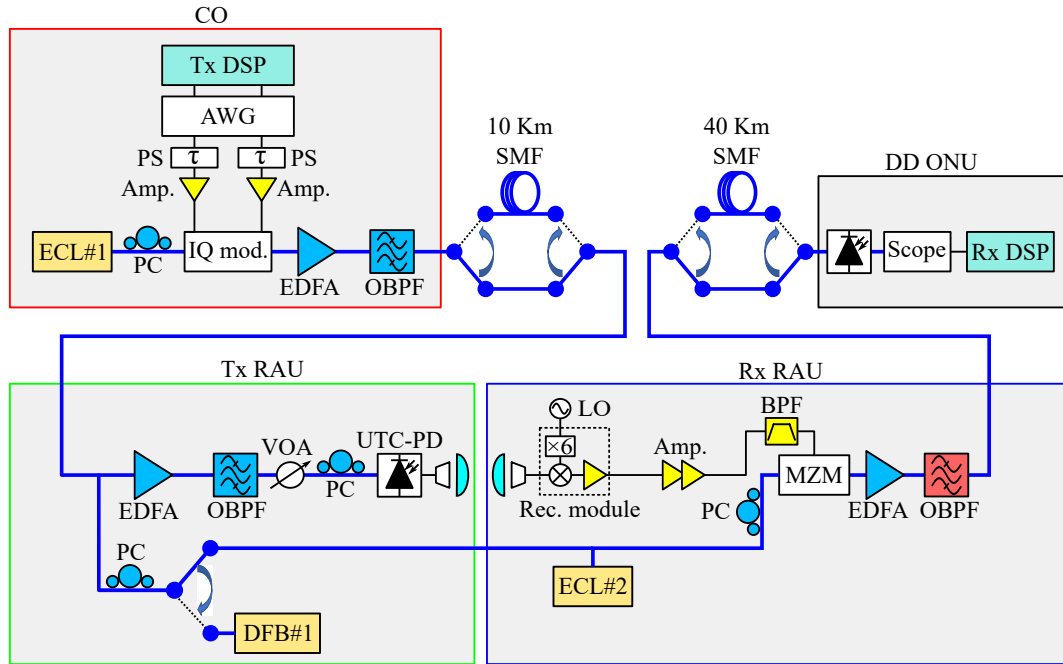


Figure 4.3: Experimental arrangement for single optical/single wireless channel THz bridge.

fiers and a BPF, which was used to remove the low-frequency noise of the receiver module. The resultant electrical signal was used to drive an IM biased between the quadrature and null points. After optical amplification, the DSB-with carrier signal from the IM was filtered with a narrow-band OBPF to suppress the upper sideband. Finally, a DD receiver was employed to recover the SSB-with carrier signal. The signal was digitized in an ADC operating at 80 GSa/s and with an analog bandwidth of 36 GHz.

The linewidth of the received signal at the ONU (i.e. including all sources of phase noise throughout the link) was measured for each laser used in the Rx RAU (i.e., ECL#2 and DFB#1) when no data was being transmitted. The product of the carrier and sideband tone of the SSB-with carrier signal generated in the Rx RAU after optical filtering was recorded by an ADC and processed digitally offline (down-converted, filtered and resampled) before computing the white frequency noise component. The linewidths obtained when ECL#2 and DFB#1 were used at the Tx RAU where 19 kHz and 1.8 MHz, respectively.

An important parameter in the pilot tone-assisted phase noise compensation

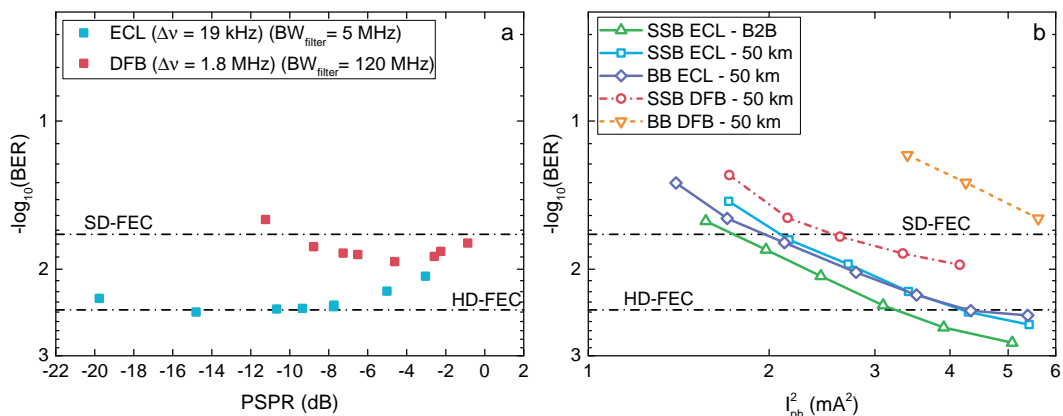


Figure 4.4: (a) BER versus PSPR for ECL#1 and DFB#1, and (b) BER curves for the various transmission configurations.

technique is the pilot tone-to-signal power ratio (PSPR). Similarly to the CSPR in envelope detected signals, there is a specific value of this ratio at which the link performance is optimal. Below this value, the pilot tone is not sufficiently above the noise level to obtain accurate phase information. At higher values, the system becomes limited by the SNR of the data-carrying signal. When using the HT and an IQ-modulator to generate the SSB signal, the PSPR can be tuned by adjusting the biasing points of the I- and Q-components. Thus, to find the optimum value, at a fixed optical power input to the PD of 13 dBm, the biasing points of the I- and Q-components in the optical modulator were tuned while measuring the BER for each biasing configuration. In Figure 4.4 (a), the BER versus the PSPR is plotted for the link with ECL#2 and the link with DFB#1. The legend in Figure 4.4 (a) indicates the linewidth of the signal reaching the ONU as well as the filter bandwidth used in the tone-assisted technique.

As can be seen, the optimum PSPR depends on the level of phase noise present in the received signal. At low levels, a narrow digital filter can be used to select the tone, minimizing the amount of AWGN introduced to the system. This enables the use of low PSPRs to maximize the SNR of the data-carrying signal. On the other hand, as the linewidth broadens, a wider filter is needed to correctly track the faster phase distortions, increasing the level of AWGN. To compensate for this and achieve a decent SNR in the filtered tone, the PSPR must be increased. This, however, compromises the SNR of the data-carrying signal as mentioned previ-

ously. The optimum PSPRs obtained for ECL#2 and DFB#1 were approximately -15 dBm and -5 dBm, respectively.

In Figure 4.4 (b), the BER curves obtained for the various transmission configurations are shown. The BER is plotted against the squared DC photocurrent generated in the PD, which is proportional to the transmitted THz power. As can be seen, at the HD-FEC limit, there is a penalty of around 1 dB (i.e., $10 \cdot \log_{10}[I_{50km}/I_{B2B}]^2 \approx 1$ dB) when the 50 km of optical fiber is inserted. This is because the optical amplifier in the Rx RAU could not entirely compensate for the extra 8 dB attenuation from the 40 km of optical fiber, which resulted in a decrease in the system's dynamic range. This could be solved by inserting an optical pre-amplifier and/or an electronic amplifier in the ONU. Regarding the comparison between baseband signals and SSB signals, the tone-assisted scheme offers a substantial advantage when linewidths comparable to those found in foundry-fabricated lasers are used. Although the use of the DFB laser prevented obtaining a BER below the HD-FEC, it was still possible to achieve a BER below the SD-FEC level (BER of $2 \cdot 10^{-2}$) with this technique, something which was not possible with baseband signals.

4.2 Wireless bridge on a WDM network

In realistic scenarios, the wireless bridge is likely to be part of a multi-user network where a single CO serves several ONUs by means of wavelength multiplexing. In Figure 4.5 (a) a depiction of such scenario is shown assuming a colorless PON, where a power split is used to address each ONU [7]. In Figure 4.5 (b), the experimental arrangement used to demonstrate a wireless bridge embedded in a WDM-PON network is shown. In this demonstration, the WDM network was configured to support 4 optical channels spaced by 17.5 GHz. The 4 optical channels were generated by means of an OFCG fed by an ECL with a linewidth of 10 kHz (ECL#3). The output of the OFCG, which consisted of 13 lines in a 10 dB bandwidth, was amplified and then filtered with a narrow-band OBPF to select 4 lines, which were fed to the IQ modulator. The IQ modulator was driven with similar signals as those

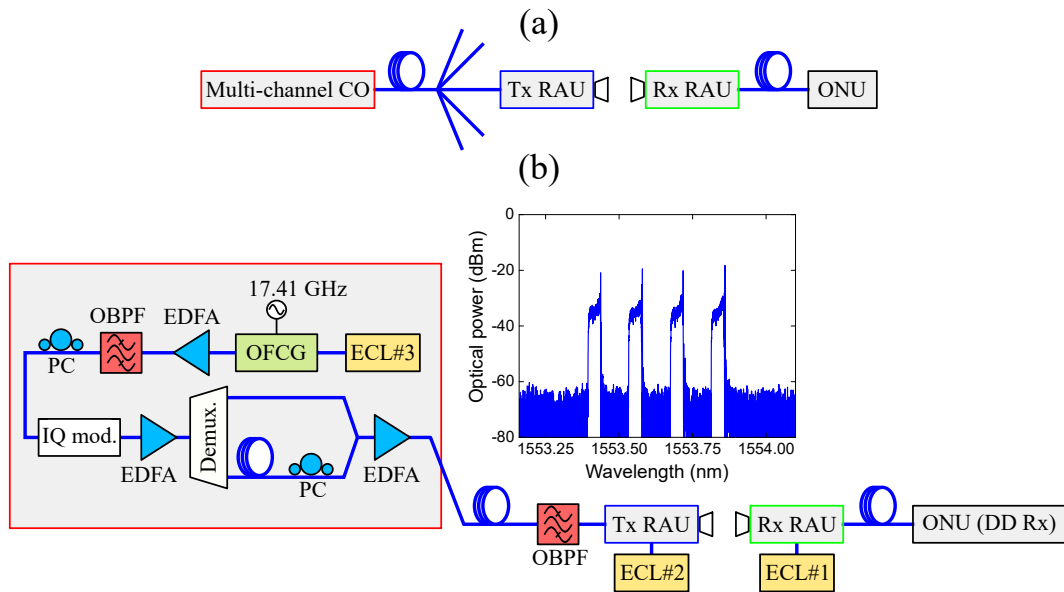


Figure 4.5: (a) Schematic representation of a wireless bridge embedded on a WDM network and (b) experimental arrangement for multiple optical-/single wireless-channel THz bridge. The inset shows the spectra of the 4 modulated optical channels before fiber transmission.

described in section 4.1. The only difference was that, based on the required digital filter bandwidths found in section 4.1, the up-conversion frequency of the baseband signal was reduced to 2.875 GHz giving a GB between tone and signal of 125 MHz.

To take into account any penalty due to inter-channel crosstalk, the 4 modulated lines were amplified and sent to a decorrelation stage. Here, the odd and even channels were first demultiplexed with a wavelength selective switch (WSS) and then delayed by more than 240 symbols (corresponding to a fiber length of around 10 m). Note that the use of this optical decorrelation technique is possible due to the use of pulse shaping filters and the large channel separation [8]. The decorrelated channels were amplified one last time (to 11 dBm) before being sent to the Tx RAU. The optical spectrum of the optical channels generated in the CO is shown in the inset of Figure 4.5 (b). At the entrance of the Tx RAU another narrow-band OBPF was used to select the channel intended for wireless transmission. The rest of the link is the same as that shown in Figure 4.3. In this case, ECL#2, whose wavelength was readjusted to always ensure a wavelength separation of 2 nm (corresponding to a carrier frequency of around 248.7 GHz) with the selected channel, was used at the

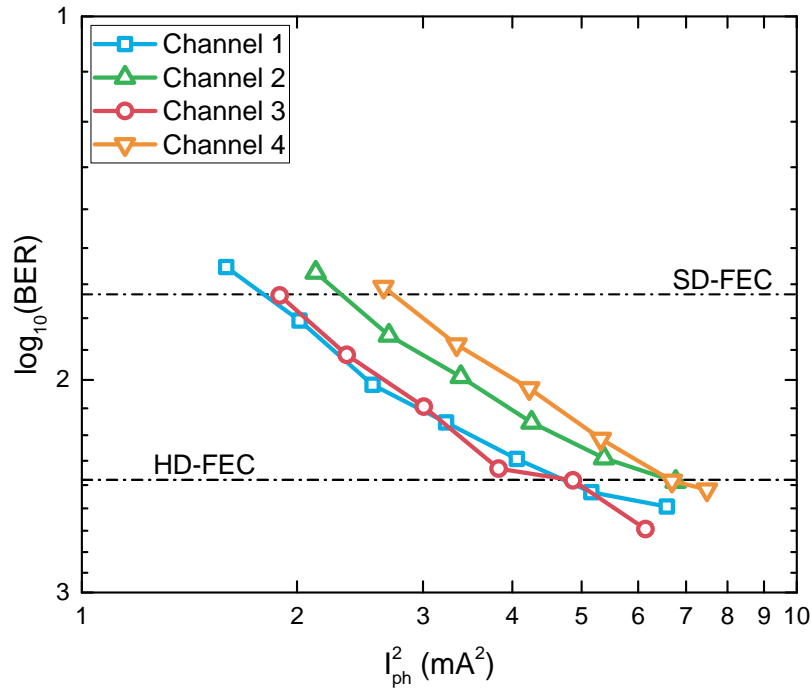


Figure 4.6: BER curves for the 4 optical channels.

Tx RAU. As in the previous demonstration, the separation between the lenses was 0.2 m. In Figure 4.6, the BER curves obtained for each channel are shown. The optimum PSPR was found to be around -12 dBm. As can be seen, a BER below the HD-FEC limit was obtained with all the channels. The higher penalty of the even channels is due to a higher signal leakage in the WSS port selecting the odd channels (i.e., a lower suppression of the even channels in this port compared to the suppression of the odd channels in the even-channels port). After decorrelation and optical recombination, this leakage interferes with the useful signal and causes a degradation in the OSNR.

4.3 Dual wireless channel transmission

Depending on the specific position of the wireless bridge in the access network, it may need to support multiple wireless-channel transmission. Assuming a tree-like PON network, if the wireless link is at the bottom of the hierarchical structure supporting only one user, then only one optical channel will need to be transmitted wirelessly. However, if the wireless link is further up in the tree network, multi-

channel wireless transmission will be required (the specific number of channels being subject to the number of subscribers supported by the node after the Rx RAU). Figure 4.7 (a), provides a depiction of such scenario. To demonstrate transmission of several wireless channels, the experimental arrangement in Figure 4.7 (b) was used. In this case, two wireless channels were supported by the THz bridge. The OFCG was replaced by two free running ECLs (ECL#3 and ECL#4) to avoid the need for narrow optical filtering and amplification and to increase the OSNR. Due to the limited IF response of the Rx RAU—with a flat region of only 9 GHz (5 GHz - 14 GHz) as can be seen from the blue curve of Figure 4.8—, the frequency separation between the two channels was decreased to around 12 GHz (the carrier frequency of the lower channel was around 236 GHz). To achieve this channel separation without incurring in a high channel crosstalk in the decorrelation stage, the WSS was replaced with two OBPFs with narrower bandwidths and sharper roll-offs. The THz response of the system (UTC and SHM) is plotted in the red curve of Figure 4.8. One can see that the THz response stayed reasonably flat over the range of carrier frequencies used in these transmissions (236 GHz - 250 GHz).

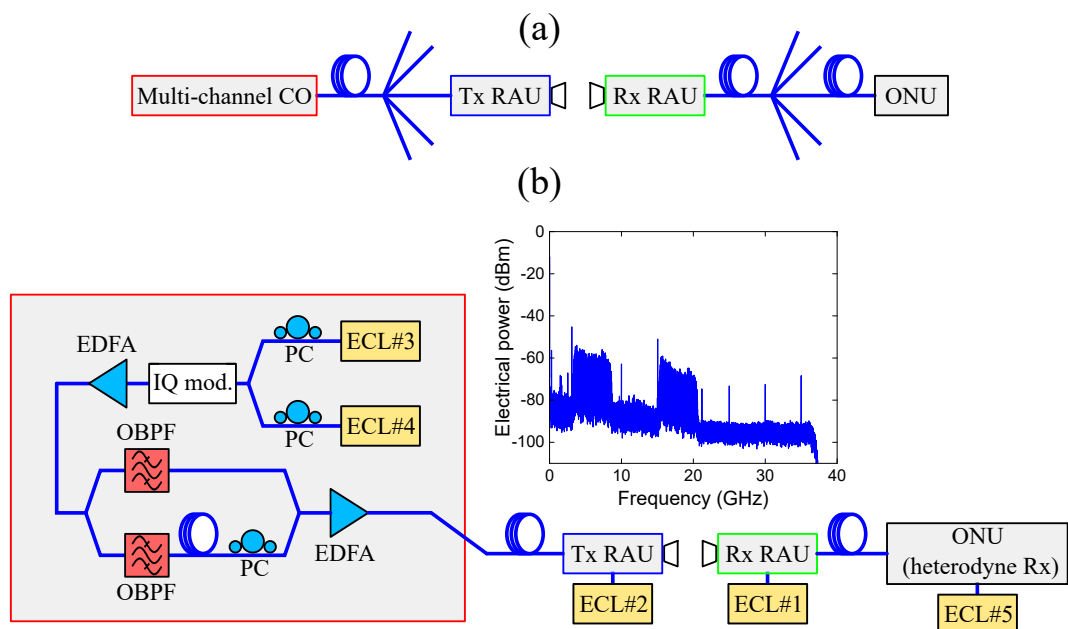


Figure 4.7: (a) Schematic representation of a wireless bridge supporting several users and (b) experimental arrangement for multiple optical-/multiple wireless-channels THz bridge. The inset shows the electrical spectra of the received signal at the ONU.

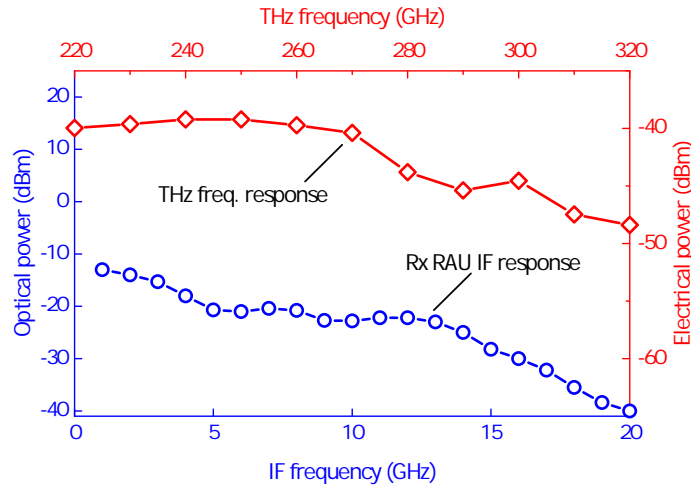


Figure 4.8: IF response of the Rx RAU (including SHM amplifiers and optical modulator) (blue curve) and combined THz response of UTC and SHM (red curve).

To maximize the sensitivity of the ONU, a coherent optical heterodyne receiver was used instead of a DD one. The laser used as optical LO was a 100 kHz-linewidth ECL (ECL#5). This also allowed biasing the Rx RAU IM at null point, maximizing the power of the generated optical sideband. To further maximize the power budget of the link, the antennas of the Rx and Tx RAUs were placed very close to each other (around 2 cm of separation) with no lenses in between. The spectrum of the electrical signal received at the ONU is shown in the inset of Figure 4.7 (b).

Figure 4.9 shows the BER curves of the two transmitted channels. Both channels were modulated at the same symbol rate, first at 4 GBd and then at 5 GBd. As can be seen, for 4 GBd (gross data rate of 32 Gbit/s), a BER below the HD-FEC limit was obtained with both channels. For 5 GBd (gross data rate of 40 Gbit/s), while only the first channel had a BER below the HD-FEC limit, the second one still exhibited a BER below the SD-FEC condition, giving a net data rate of 35 Gbit/s (assuming code rates of 0.84 and 0.94 for the SD-FEC and HD-FEC processes, respectively).

As can be seen from Figure 4.9 (a), channel 2 performed better than channel 1 at 4 GBd but worse at 5 GBd. The reason for this change is likely to be the IF response of the Rx RAU. For 5 GBd, the optical frequency of channel 2 was slightly increased to avoid cross-talk in the decorrelation stage. This, as shown in Figure 4.9

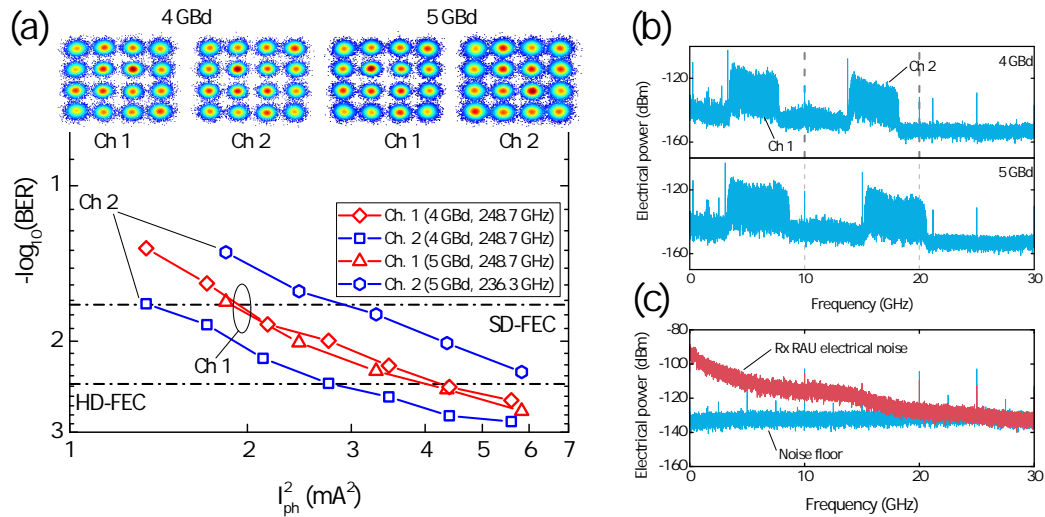


Figure 4.9: (a) BER curves of the 2 transmitted channels at 4 GBd and 5 GBd (the THz frequency of each channel is shown in the legend); (b) electrical spectrum of the signals received at the ONU for each modulation speed; (c) electrical noise in the Rx RAU.

(b), caused this channel to be downconverted to the region of the Rx-RAU response with a strong roll-off (see Figure 4.8). On the other hand, the better performance of this channel at 4 GBd is likely to be due to the increased noise at lower IFs in the Rx RAU (Figure 4.9 (c)).

4.4 40 Gbit/s wireless bridge

In section 4.3, the main factor limiting the system capacity, was the decorrelation stage. The finite dB/nm roll-off of the OBPFs prevented the closer allocation of the two channels. Because of this and the limited IF response of the Rx RAU, it was not possible to recover a BER below the FEC limit at 40 Gbit/s. To overcome this limitation, the two channels were multiplexed in the digital domain using a technique called twin-SSB [9]. Since the two channels can be generated from two independent symbol sequences, there is no need for a decorrelation stage. The DSP for twin-SSB signal generation is shown in Figure 4.10. The basic idea behind the twin-SSB technique is to generate two SSB signals, and through appropriate DSP map them to apposite sidebands. Since both sidebands contain useful information, a more efficient use of the dual-channel AWG is made.

As can be seen in Figure 4.10, the signals were pre-equalized to compensate

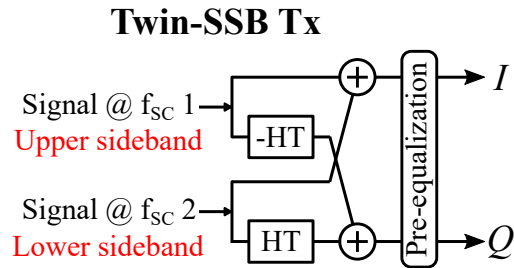


Figure 4.10: Digital transmitter and receiver for twin-SSB transmission.

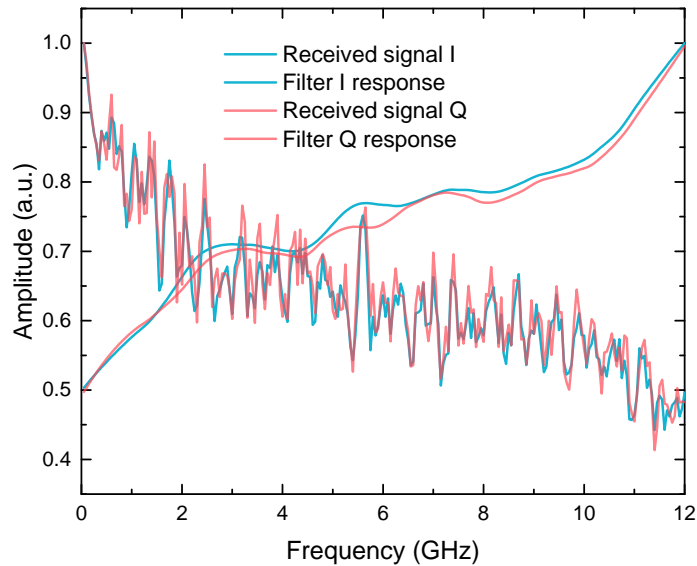


Figure 4.11: Electrical channel and pre-equalization filter responses

the frequency response of the equipment in the CO. The pre-equalizer was based in the zero forcing principle and was implemented in the frequency domain. To measure the frequency response of the transmitter, a frequency comb was generated in the AWG and passed through each electrical arm feeding the optical modulator. To avoid a high peak-to-average power ratio (PSPR), the phase of each comb tone was chosen randomly [10]. After recording each received waveform in the ADC, the comb lines were located to get the I- and Q-channel responses. After calculating the inverse of the response and applying a smoothing filter, the frequency response of the filter was generated. In Figure 4.11, the measured response (up to 12 GHz) of each electrical channel, as well as the calculated pre-equalization filter responses, is shown.

As was done in section 4.1, the performance of the system transmitting base-

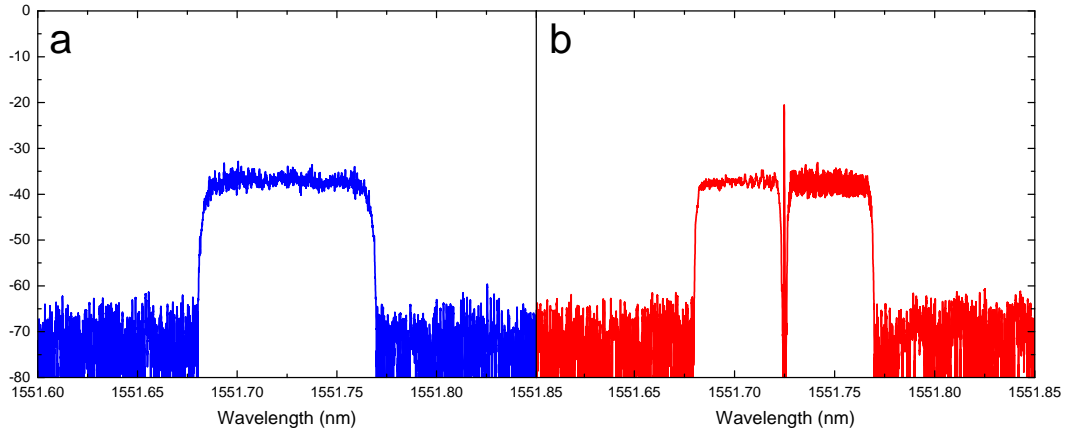


Figure 4.12: Optical spectra of (a) baseband signal and (b) twin-SSB signal.

band signals was also characterized for benchmarking purposes. In this case, to match the data rate and bandwidth of the twin-SSB signal, a 10 GBd QAM signal with a roll-off factor of 0.125 was used (the roll-off factor was increased to account for the frequency separation between tone and the two sidebands in the twin-SSB signal). Compared to previous occasions, the VV algorithm was replaced by the blind PE algorithm proposed in [11]. One of the drawbacks of the square QAM-adapted VV algorithm is that not all the received samples are used to calculate the symbol deviations introduced by phase noise. Because of this, tracking the phase deviations while keeping a reasonable filter length becomes harder as the linewidth increases. To solve this, the authors of [11], propose a different technique which does not rely on the M^{th} power operation. In this algorithm, the incoming samples are de-rotated by several test angles. After this, the distance to the closest constellation point is calculated. The squared distance of several adjacent symbols is then summed and the optimum phase estimate is that yielding the lowest sum of squared distances. Although the complexity of this algorithm is higher than that of the VV algorithm [12], it enables an improved sensitivity and, thus, is a good algorithm to benchmark the performance of the twin-SSB technique. The optical spectra of both the baseband and twin-SSB signals are shown in Figures 4.12 (a) and (b) respectively.

Using the experimental arrangement shown in Figure 4.3 and a coherent receiver at the ONU (the Rx RAU IM was biased at the null point), the BER produced

by each signal was calculated. In Figure 4.13, the BER obtained for each scheme is shown as a function of the squared photocurrent. To calculate the total BER of the twin-SSB signal, the number of errors produced by each channel in a time interval of $10 \mu\text{s}$ was divided by the sum of the symbols transmitted by each of them. For comparison with the results of section 4.3, the inset of Figure 4.13 shows the BER of each sideband. As can be seen, unlike in transmission of section 4.3, the two channels were able to produce a BER below the HD-FEC limit.

In terms of the relative performance between the two techniques, interestingly, the twin-SSB signal exhibited better performance at low values of photocurrent. On the other hand, for values of photocurrent higher than approximately 2 mA, the BER of this technique, unlike that of the baseband system, remained constant. This could be attributed, in principle, to an improper biasing of the IQ modulator, which would cause a lower OSSR and residual image noise. To rule out this possibility, the twin-SSB transmitter was rearranged to enable the use of the same biasing configuration as the baseband system. To do so, the optical tone from ECL#1 was split into two paths. One of them was passed through the IQ modulator and the other through a polarization controller to match both polarization states. Both paths were then recombined in a second 3 dB coupler. By doing this, the biasing points of the IQ modulator could also be set at the null point for twin-SSB transmission. Doing this, however, did not improve the results and the BER curve exhibited exactly the same behavior (see Figure 4.13).

Since neither changing the amplifiers nor increasing the degree of attenuation after the enclosed THz receiver corrected this (i.e., saturation effects occurred at the same value of photocurrent), these effects are likely to be caused by the THz receiver itself. It is important to mention that the saturation point when transmitting the QAM signal (i.e., without the pilot tone) occurred at higher photocurrents. This is likely to be due to the higher PSPR of the twin-SSB signal.

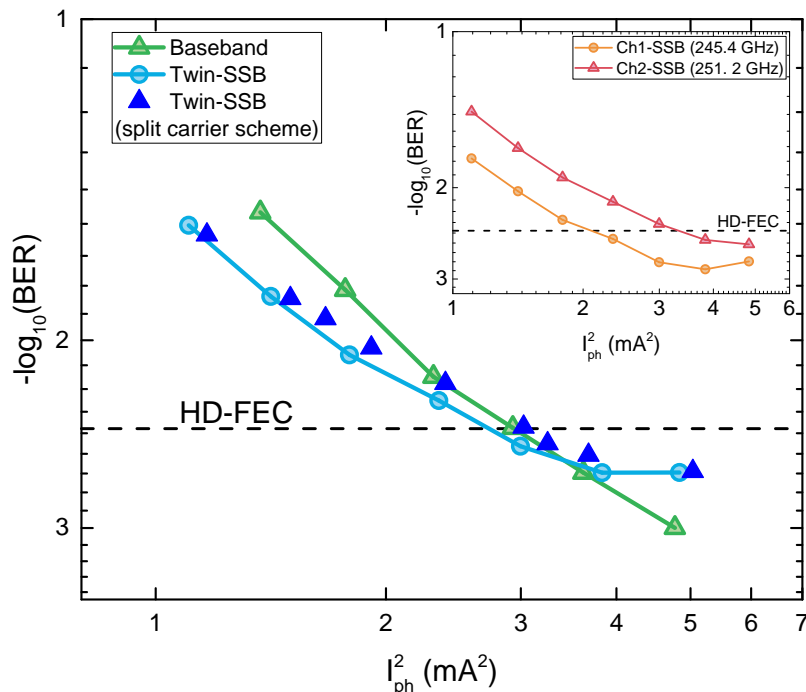


Figure 4.13: BER as a function of the squared photocurrent for twin-SSB (both for conventional approach and split carrier scheme) and baseband signals. The inset shows the BER produced by each of the sidebands in the twin-SSB signal.

4.5 Conclusions

Among the envisaged applications of sub-THz communications, wireless bridges have attracted significant interest due to the wide range of scenarios where they may be used. In this chapter, the tone-assisted carrier recovery is proposed to mitigate the phase noise of the free-running lasers present in such links. Using this technique, a single optical-/single wireless-channel THz bridge operating at 250 GHz and transmitting 5 GBd 16 QAM signals is realized. The proposed wireless bridge is also demonstrated in the context of a WDM network scenario, where the CO transmits several optical channels and the Tx RAU selects one of them for wireless transmission. After this, two wireless channels are transmitted simultaneously in an effort to increase the number of users supported by the wireless bridge, achieving a net data rate of 35 Gbit/s. Finally, to further scale the capacity of the wireless bridge the twin-SSB technique is proposed, whereby two SSB are multiplexed in the digital domain. For benchmarking purposes, the proposed scheme is compared against the performance of a baseband system using advanced carrier recovery at the digital

receiver. Interestingly, the twin-SSB technique showed better performance at lower values of photocurrent. On the other hand, at high values of photocurrent this technique seemed to saturate the THz enclosed receiver. This is likely to be due to the higher PSNR of the twin-SSB signal compared to that of a QAM signal.

Bibliography

- [1] Y. Salamin, B. Baeuerle, W. Heni, F. C. Abrecht, A. Josten, Y. Fedoryshyn, C. Haffner, R. Bonjour, T. Watanabe, M. Burla, D. L. Elder, L. R. Dalton, and J. Leuthold. Microwave plasmonic mixer in a transparent fibrewireless link. *Nature Photonics*, (Mim), 2018. ISSN 1749-4885. doi: 10.1038/s41566-018-0281-6. URL <http://www.nature.com/articles/s41566-018-0281-6>.
- [2] S Ummethala, T Harter, K Koehnle, Z Li, S Muehlbrandt, Y Kutuvantavida, Juned N.; Kemal, J. Schaefer, H. Massler, A. Tessmann, S. K. Garlapati, A. Bacher, L. Hahn, M. Walther, T. Zwick, S. Randel, W. Freude, and C. Koos. Wireless Transmission at 0.3 THz Using Direct THz-to-Optical Conversion at the Receiver. *European Conference on Optical Communication*, (1):We4.3, 2018.
- [3] S. Koenig, D. Lopez-Diaz, J. Antes, F. Boes, R. Henneberger, A. Leuther, A. Tessmann, R. Schmogrow, D. Hillerkuss, R. Palmer, T. Zwick, C. Koos, W. Freude, O. Ambacher, J. Leuthold, and I. Kallfass. Wireless sub-THz communication system with high data rate. *Nature Photonics*, 7(12):977–981, 2013. ISSN 17494885. doi: 10.1038/nphoton.2013.275.
- [4] Atsushi Kanno, Pham Tien Dat, Norihiko Sekine, Iwao Hosako, Naokatsu Yamamoto, Yuki Yoshida, Ken-ichi Kitayama, and Tetsuya Kawanishi. Seamless Fiber-Wireless Bridge in the Millimeter- and Terahertz-Wave Bands. *Journal of Lightwave Technology*, 34(20):4794–4801, 2016.
- [5] Can Wang, Jianjun Yu, Xinying Li, Pengqi Gou, and Wen Zhou. Fiber-THz-Fiber Link for THz Signal Transmission. *IEEE Photonics Journal*, 10(2), 2018. ISSN 19430655. doi: 10.1109/JPHOT.2018.2809433.
- [6] Xinying Li, Jianjun Yu, Jiangnan Xiao, and Yuming Xu. Fiber-wireless-fiber link for 128-Gb/s PDM-16QAM signal transmission at W-band. *IEEE Photonics Technology Letters*, 26(19):1948–1951, 2014. ISSN 10411135. doi: 10.1109/LPT.2014.2342711.
- [7] Domani Lavery, Robert Maher, David S. Millar, Benn C. Thomsen, Polina Bayvel, and Seb J. Savory. Digital coherent receivers for long-reach optical access networks. *Journal of Lightwave Technology*, 31(4):609–620, 2013. ISSN 07338724. doi: 10.1109/JLT.2012.2224847.
- [8] A.H. Gnauck, P.J. Winzer, S. Chandrasekhar, X. Liu, B. Zhu, and D.W. Peckham. 10 x 224-Gb/s WDM transmission of 28-Gbaud PDM 16-QAM on a 50-GHz grid over 1,200 km of fiber. *Optical Fiber Communication (OFC), collocated National Fiber Optic Engineers Conference, 2010 Conference on (OFC/NFOEC)*, pages 26–28, 2010. ISSN 21622701. doi: 10.1364/NFOEC.2010.PDPB8.
- [9] Zhenbo Xu, Rongqing Hui, and Maurice O Sullivan. Dual-band OOFDM system based on tandem single-sideband modulation transmitter. 17(16):13479–13486, 2009. ISSN 1094-4087. doi: 10.1364/OE.17.013479.
- [10] F. C. Abrecht, R. Bonjour, S. Welschen, A. Josten, B. Baeuerle, D. Hillerkuss,

- M. Burla, and J. Leuthold. Pre-equalization technique enabling 70 Gbit/s photonic-wireless link at 60 GHz. *Optics Express*, 24(26):30350, 2016. ISSN 1094-4087. doi: 10.1364/OE.24.030350. URL <https://www.osapublishing.org/abstract.cfm?URI=oe-24-26-30350>.
- [11] Timo Pfau, Sebastian Hoffmann, and Reinhold Noé. Hardware-efficient coherent digital receiver concept with feedforward carrier recovery for M-QAM constellations. *Journal of Lightwave Technology*, 27(8):989–999, 2009. ISSN 07338724. doi: 10.1109/JLT.2008.2010511.
- [12] Xiang Zhou. Efficient clock and carrier recovery algorithms for single-carrier coherent optical systems: A systematic review on challenges and recent progress. *IEEE Signal Processing Magazine*, 31(2):35–45, 2014. ISSN 10535888. doi: 10.1109/MSP.2013.2281071.

Chapter 5

Conclusions and further work

Different THz communication system configurations have been explored in this thesis. In this chapter, the salient results from these investigations are summarized (section 5.1). Suggestions for potential research directions in THz communications are given in section 5.2.

5.1 Summary of research

There is a need for bandwidth in wireless communications due to increased user adoption of higher bandwidth services. In recognition of this, research around the world has pushed the RF carrier frequencies beyond 60 GHz. After a period of technology development in what was usually referred to as the "THz gap", the status of THz communications has evolved to a stage of end-to-end system demonstrations. In this context, this thesis has investigated the feasibility of using photonic technologies for the generation of THz. A special focus has been placed on mitigating the phase noise problem associated with optical sources.

In the first part of the thesis, the envelope detection of THz IM SSB is proposed as a mean to combat phase noise. This approach enabled to completely eliminate the carrier recovery part of the receiver DSP routine. Although the VV algorithm is employed in the experiments reported in this thesis, this is only due to a phase offset (i.e. constant with time) that results from the power difference between the two optical tones generated in the IQ modulator. No significant phase noise penalty was observed in a 250 GHz system transmitting 5 GBd 16-QAM signals, with a fiber

length of 10 Km between CO, and RAU and for combined optical linewidths of around 1 MHz. This result confirms the feasibility of using cost-efficient foundry-fabricated lasers in the RAU, which is essential to keep the cost of this unit low.

The use of DSP for SSBI mitigation is also proposed in this work to increase the bandwidth efficiency of ED-based THz systems. In fact, the first demonstration of a photonic wireless link using the KK receiver is reported here. This algorithm has received renewed attention in DD optical networks due to its superior performance compared with other interference cancellation techniques. The spectral efficiency gain of this algorithm is experimentally verified, achieving an efficiency improvement of 38% with respect to the transmission without this algorithm.

The performance of the ED-based approach is also compared with that of a THz system transmitting QAM signals (in this thesis referred to as baseband signals) and using carrier recovery at the digital receiver for various optical linewidths. As was expected, a penalty dependence with linewidth was observed in the case of the baseband signals. Due to the SSBI associated with envelope detection, the SSB signals exhibited lower performance at low combined optical linewidths. However, owing to the phase noise insensitivity of this scheme, and the degradation of the VV at high optical linewidths, these signals exhibited better performance at high optical linewidths. In particular, the performance surpass was found to happen at a (combined linewidth)(symbol period) product of $1.1 \cdot 10^{-4}$, which translates into a combined linewidth of 1.1 MHz if we assume a symbol rate of 10 GBd. As said previously, this indicates that the approach of envelope detection can offer better prospects if cost-efficient lasers are to be used.

The use of wide GBs can also be used to combat the SSBI. In fact, given the large unregulated spectrum found at THz frequencies, THz systems using envelope detection may opt for this solution to reduce the amount of DSP used at the digital receiver. This, however, can place a stringent requirement on the analog bandwidth of the transmitter AWG if the the CSSB technique is used and considering the high symbol rates that are envisaged for THz communications. To avoid the need for very large analog bandwidths, two techniques that relax this requirement are introduced

to the field of THz-over-fiber in this thesis: DVSSB and AVSSB. The former one reduces the required bandwidth by a factor of 2 but, according to the simulations carried out in this thesis, suffers from a SNR penalty as the CSPR is increased. This comes from the fact that the total available AWG power has to be shared between the tone and sideband. This decrease is not observable either in the AVSSB or CSSB techniques, where the sideband SNR remains constant with CSPR. Between these two techniques, the best SNR in the simulation is obtained with the AVSSB, which also enables the highest reduction of bandwidth. This, on the other hand, comes at the expense of a considerable increase in the analog complexity of the transmitter. End-to-end implementation of the three techniques in a THz system are also demonstrated within this thesis. 20 Gbit/s transmissions at 250 GHz and several GBs were carried out for each technique. In these transmissions, similar results were obtained between all techniques. This accounts for the fact that receiver noise dominated over transmitter noise.

The second part of this thesis focuses on wireless bridges, which have attracted the interest of the THz community due to the wide range of scenarios where they could find application. To mitigate the phase noise associated with the high number of free-running lasers that form this type of links (up to 4 if a coherent optical receiver is used), the pilot tone-assisted technique is proposed in this thesis. Using this scheme, a single channel wireless bridge supporting a net data rate of 20 Gbit/s is realized. The proposed wireless bridge is also demonstrated in the context of a WDM network scenario, where the CO transmits several optical channels and the RAU selects one of them for wireless transmission. After this, two wireless channels are transmitted simultaneously in an effort to increase the number of users supported by the wireless bridge. With this configuration, a net data rate of 35 Gbit/s is achieved under the assumption of SD-FEC. Finally, to further increase the capacity of the proposed wireless bridge, the twin-SSB technique is proposed. Its performance is benchmarked with the alternative approach of transmitting a baseband signal and using advanced carrier recovery at the receiver. While the former approach yields better results at low PD photocurrents, it also leads to a more rapid

(i.e., for lower values of optical input power to the PD) system saturation than the baseband approach.

5.2 Further work

Before commenting on research lines arising specifically from the work carried out in this thesis, it is necessary to make a comment on research topics that apply to THz communications systems in general. The first one is the realization of a THz system with beam steering and active tracking capabilities. While concepts of each of these functionalities have been proposed and/or experimentally validated separately [1] [2], the realization of a THz system combining both of them has yet to be demonstrated. Regarding DSP, after an initial period where the use of optical coherent DSP for THz communications has been validated, experiments could now focus on the realization of real-time transmissions, studying the economical and latency viability of the proposed DSP algorithms for the different use cases. These two actions, together with efforts to increase link distances via more powerful THz technology, could then result in the first field trial demonstrations as the last step before commercial implementation.

Regarding the specific work carried out in this thesis, while the use of a digital DSP, served to prove the phase robustness of SSB signals and demonstrate the performance improvement obtained with the KK receiver, its use on real system is unlikely. The reason for this is the fact that a THz LO is required when the envelope detection is performed digitally, which undermines one of the main reasons to use an ED. For SSB transmission with heterodyne down-conversion, one can simply use the tone-assisted technique to avoid the SSBI (as it is done in the second part of this thesis). Hence, future demonstrations should focus on the use of a THz ED. This will bring another set of challenges which can potentially lead to new research lines. The first one has already been published and relates to the not necessarily quadratic transfer function of a THz ED. The implication of this in the implementation of the KK receiver in a THz system is investigated in [3], where the authors claim to get better results when approximating the ED transfer function to an exponential func-

tion instead of a quadratic one. The use of a THz KK could also reveal a different $(\text{linewidth}) \times (\text{symbol rate})$ product intersection in the comparison between the heterodyne and the ED system. This intersection could then be used to determine the most appropriate type of detector for the application under consideration.

Merging the two experimental chapters of this thesis, the realization of a wireless bridge using envelope detection at the Rx RAU could be a step towards the simplification of such unit. In this sense, given all the available techniques for THz-to-optical conversion, a detailed comparison between them would be interesting. Considering the stringent requirements of cost and size that these units must fulfill, figures of merits for such comparison would take into account things such as power consumption or potential to be integrated in a single chip, besides, of course, power sensitivity. Increasing data rates in wireless bridges is also a top priority since, as shown in Table 2.1, this type of links will require data rates up to 100 Gbit/s. Equally important will be the Demonstration of THz wireless bridges with full duplex capabilities. This, while has not been yet reported, will be key to assessing the full potential of this application. In fact, the transition from half- to full-duplex is a pending task for THz communications in general. In this regard, design considerations such as the use of independent antenna units for each link direction (as proposed in [4]) or single antenna units with circulators (as proposed in [5]) will need to be carefully studied and assessed for each of the envisaged applications.

Bibliography

- [1] Bile Peng, Ke Guan, and Thomas Kurner. Cooperative dynamic angle of arrival estimation considering space-time correlations for terahertz communications. *IEEE Transactions on Wireless Communications*, 17(9):6029–6041, 2018. ISSN 15582248. doi: 10.1109/TWC.2018.2854565.
- [2] Yang Zhou, Goki Sakano, Yusuke Yamanaka, Hiroshi Ito, Tadao Ishibashi, and Kazutoshi Kato. 600-GHz-Wave Beam Steering by Terahertz-Wave Combiner. *Optical Fiber Communication Conference*, page M4J.1, 2018. doi: 10.1364/OFC.2018.M4J.1. URL <https://www.osapublishing.org/abstract.cfm?URI=OFC-2018-M4J.1>.
- [3] Tobias Harter, Christoph Füllner, Juned N Kemal, Sandeep Ummethala, Miriam Brosi, Erik Bründermann, Wolfgang Freude, Sebastian Randel, and Christian Koos. 110-m THz wireless transmission at 100 Gbit/s using a Kramers-Kronig Schottky barrier diode receiver. *44th European Conference on Optical Communication (ECOC'18)*, (1):Th3F.7 (postdeadline paper), 2018.
- [4] Yasunao Katayama, Kohji Takano, Yasuteru Kohda, Nobuyuki Ohba, and Daiju Nakano. Wireless data center networking with steered-beam mmWave links. *2011 IEEE Wireless Communications and Networking Conference, WCNC 2011*, pages 2179–2184, 2011. ISSN 1525-3511. doi: 10.1109/WCNC.2011.5779470.
- [5] Haymen Shams and Alwyn Seeds. Photonics, Fiber and THz Wireless. *Optics and Photonics News*, (March):24–31, 2017.

Acronyms

ADC analog-to-digital converter.

ASE amplified spontaneous emission.

AVSSB analog virtual single sideband.

AWG arrayed waveguide grating.

AWG arbitrary waveform generator.

AWGN additive white Gaussian noise.

BBoF baseband-over-fibre.

BER bit error rate.

BPF band pass filter.

BPSK binary phase shift keying.

BS base station.

BW passband signal bandwidth.

CD chromatic dispersion.

CMOS complementary metal-oxide-semiconductor.

CO central office.

C-RAN cloud-radio access network.

CSPR carrier-to-sideband power ratio.

CSSB conventional virtual single sideband.

CW continuous wave.

DAC digital-to-analog converter.

DC direct current.

DD decision directed.

DD direct detection.

DFB distributed feedback.

DSB double sideband.

DSB+C double sideband-with carrier.

DSP digital signal processing.

DVSSB digital virtual single sideband.

ECL external cavity laser.

ED envelope detector.

EDFA erbium doped fiber amplifier.

ENOB effective number of bits.

ER extinction ratio.

FEC forward error correction.

FFT fast Fourier transform.

FM frequency modulated.

FOE frequency offset estimation.

FSPL free-space path loss.

GB guard band.

HBT heterojunction bipolar transistor.

HD hard decision.

HEMT high electron-mobility transistor.

HT Hilbert transform.

IF intermediate frequency.

IM intensity modulated.

IQ in-phase quadrature.

ISD information spectral density.

ISI intersymbol interference.

KK Kramers-Kronig.

LAN local access networks.

LMS least mean squares.

LO local oscillator.

LOS line-of-sight.

LPF low pass filter.

MMIC monolithic microwave integrated circuit.

MZM Mach-Zehnder modulator.

N_0 noise spectral density.

NF noise figure.

NIR near-infrared.

OBPF optical band pass filter.

OFCG optical frequency comb generator.

OFDM orthogonal frequency division multiplexing.

ONU optical network unit.

OOK on-off keying.

OPLL optical phase locked loop.

OSNR optical signal-to-noise ratio.

OSSR optical sideband suppression ratio.

OWC optical wireless communication.

PD photodiode.

PE phase estimation.

PM polarization multiplexing.

PON passive optical network.

PS phase shifter.

PSK phase shift keying.

PSPR pilot tone-to-signal power ratio.

QAM quadrature amplitude modulation.

QPSK quadrature phase shift keying.

RAU remote antenna unit.

- RDE** radius directed equalizer.
- RF** radio frequency.
- RoF** radio-over-fibre.
- RRC** Root raised cosine.
- RTD** resonant tunneling diode.
- SBD** Schottky barrier diode.
- SD** soft decision.
- SHM** sub-harmonic mixer.
- SMF** single mode fiber.
- SNDR** signal-to-noise-and-distortion ratio.
- SNR** signal-to-noise ratio.
- SNR_b** signal-to-noise ratio per bit.
- SSB** single sideband.
- SSBI** signal-signal beat interference.
- UTC** uni-travelling carrier.
- VV** Viterbi-Viterbi.
- WDM** wavelength division multiplexing.
- WLAN** wireless local access networks.
- WPAN** wireless personal access networks.
- WSS** wavelength selective switch.